Contract F 61o52 67 C oo46 January 1968

SCIENTIFIC REPORT Interim

No 6

Research on Atmospheric Optical Radiation Transmission

1 Dec 1966 - 3o Nov 1967

K.Bullrich, W.Blättner, T.Conley,
R.Eiden, G.Hänel, K.Heger, W.Nowak

Meteorologisch-Geophysikalisches Institut
der
Johannes Gutenberg-Universität
Mainz, Germany

This research has been sponsored in part by the AIR FORCE CAMBRIDGE RESEARCH LABORATORIES, through the European Office of Aerospace Research, OAR, US Air Force under Contract F 61o52 67 C oo46.

AFCRL-68-0186

Contract F 61o52 67 C oo46 January 1968

SCIENTIFIC REPORT Interim

No 6

Research on Atmospheric Optical Radiation Transmission

1 Dec 1966 - 3o Nov 1967

K.Bullrich, W.Blättner, T.Conley,
R.Eiden, G.Hänel, K.Heger, W.Nowak

Meteorologisch-Geophysikalisches Institut
der
Johannes Gutenberg-Universität
Mainz, Germany

This research has been sponsored in part by the AIR FORCE CAMBRIDGE RESEARCH LABORATORIES, through the European Office of Aerospace Research, OAR, US Air Force under Contract F 61o52 67 C oo46.

Abstract.

A. Measurements of the spectral distribution of the sky radiation and of the radiation reflected by the ground as well as of their degrees of polarization have been done at Alamogordo, N.M., USA.
The purpose of this research study has been to obtain information on the sky radiation, reflected radiation and their degrees of polarization in an air mass which is not polluted by man made activity.

1. The study contains measurement results of the distribution of the sky radiation in the short wave and near infrared range. The measurements have been done in different verticals at different solar elevations; furthermore, in the solar almucantar close to and far from the sun. The influence of the great reflectivity of the White Sands desert could be shown.

2. Measurements of the extinction coefficient as a function of the wave length show a wavelength exponent between 1.3 and 1.8.

3. Measurements of the radiation reflected by the surface of the earth in the short wave and near infrared range show the maximum in the red wavelength. This corresponds to the sky radiation at a distance of about 10° from the sun.

4. The measurement results of the degree of polarization in the sky show very high values. However, the spectral distribution does not follow Rayleigh's law. The portion

of incident radiation which is reflected by the surface of the earth contributes to diminishing the polarization. The influence of the high reflectivity of the White Sands desert was observed. The degree of polarization decreases in the wavelength range $\lambda > 0.6\ \mu$.

5. The measurement results of the degree of polarization of the radiation reflected by the surface of the earth taken from the Two Buttes (115 m above MSL) show the influence of the atmospheric layer between the observer and the surface. With increasing zenith distance of the point under observation, the degree of polarization goes almost to 0%.

6. In order to get an insight in the atmospheric aerosol particle size distribution near the ground the Aitken nuclei have been measured and, furthermore, the particles $0.3 < r < 15\ \mu$ with the help of the Royco device. The number of particles undergoes great variations with time, especially in the range of the large ones. There is no connection with the large particles and the variation of the Aitken nuclei. The decrease of the large particles in the radius interval of 0.4 and 2 μ follows the power law $r^{-1.6}$. The interval from 0.06 through 0.44 μ showed r^{-4}. The radiation measurements for the entire atmosphere have yielded a r^{-4} relationship.

B. Experimental and theoretical investigations into the spectral and angular dependence of reflectivity and the degree of polarization of reflected radiation of various soil types have been performed.

1. The measurements of the reflectivity of light which has been reflected by calcareous soil have been continued. Furthermore, samples of red, grey and white sand from the New Mexico desert have been used to study the different properties in reflectivity of the desert soil.

2. The theoretical explanation for the variation in reflectivity could be given for calcareous soil and grey sand. Each soil sample has a broad particle size distribution. The computation of the reflection based upon scattering processes in different directions. The scattering medium has been assumed as infinitely thick. It could be shown that the measured reflection of the calcareous soil follows a scattering function which is proportional to (1 - cos φ). Furthermore, it was possible to consider the secondary scattering process which requires an additional term. Particularly the angular dependence of the fine grained soil sample could be explained in this way.

C. In the Chapter C the influence of the shape of the aerosol particles on their collection in a jet impactor was studied preliminary. The shape and the density play an important role in the collection process. In addition, there is no agreement in the calibrations of impactors which various authors have made under different atmospheric conditions. It is necessary to improve the theory of the jet impactor, specially for the sampling of aerosol particles and measuring the index of refraction.

D. New measurements of the degree of polarization have been carried out at Mainz to get an insight in the dayly variation of the atmospheric aerosol size distributions and other parameters which influence the spectral distribution of the sky radiation. It could be shown the significance of the behaviour of the two polarization maxima in the sky radiation.

E. A new attempt has been done to construct a portable scattering function meter. The principle is based upon the principle of Duntley's device. But it differs from it in some important ways so that the applicability is enlarged.

F. The influence of second order scattering on the sky radiation and on the radiation emerging from the earth's atmosphere under assumption of a turbid atmosphere has been investigated comprehensively. The great influence in the case of short wavelength and high turbidity is to be seen on the Figures 74 - 77. There, the amount of the secondary scattering near the horizon is 80% of the primary scattering. The computations will be extended for the third order scattering and for the reflectivity of the ground corresponding Chapter B III.

Table of Contents. Page

Figures.

Frequently Used Symbols:

B :	Radiance
H:	Solar Elevation Angle
P:	Degree of Polarization
T:	Turbidity Factor
z:	Zenith Distance of a Point in the Sky
Z:	Zenith Distance of the Sun
T.B.:	Two Buttes
W.S.:	White Sands
a.m.:	forenoon
p.m.:	afternoon
α:	Angle of Azimuth
θ_0:	Angle of Incidence
θ:	Angle of Observation
φ:	Scattering Angle
λ:	Wavelength, where 0: 0.443 μ, 1: 0.548 μ, 2: 0.639 μ, 3: 0.708 μ, 4: 0.053 μ, 5: 0.911 μ.

Fig. 64: Computed Reflectivity of an Infinitely Thick Medium With the Given Scattering Function $30(1 - \cos\varphi)$ for $\lambda = 0.545\ \mu$.
a) and b) for primary scattering (PS);
c) and d) taking secondary scattering into account (SS).

65: Do. 64, Abscissa: Θ, Ordinate: Reflectivity; PS - - -, SS ——,
Measured Values: x fine grained, o coarse grained calcareous sample.

66: Do. 63, $\Theta_0 = 90°$ for Various λ.
The solid curves refer to the function $(1 + \cos^2 \varphi)$.

67: Computed Reflectivity as a Function of the Zenith Distance of the Observer in the Light Source's Vertical.
The plotted values of measurements refer to coarse samples for various Θ_0 at $\lambda = 0.545\ \mu$.
The solid curve represents the computed reflectivity of an infinitely thick medium under the assumption of a phase function according to Schoenberg.
Reflection by a surface element of an individual sphere according to Lambert,
Reflection by a surface element according to Seeliger.

68a: Collection Efficiency η as a Function of the Equivalent Radius r for Various Dynamic Shape Factors $\varkappa$.

A. Measurements of the Spectral Distribution of the Sky Radiation and of the Radiation Reflected by the Ground as Well as of Their Degrees of Polarization at Alamogordo, New Mexico, U.S.A.

Introduction.

The purpose of this research study has been to obtain information on the sky radiation, reflected radiation and their degrees of polarization in an air mass which is not polluted by man made activity in the desert area of New Mexico. Furthermore, it has been planned to carry out these measurements in connection with a balloon flight of the Atmospheric Optics Branch, USAF Cambridge Research Lab., Bedford.

The measurements have been performed from 28 March through 9 April 1967 near Alamogordo, N.M., mainly on top of a steep hill named "Two Buttes" which rises by 115 m above the plain valley: φ = 32°40'N, λ = 106°10'W, altitude 1.460 m above MSL (Fig. 1). Brownish grey sand covers the surroundings of this hill. The land is grown over with sparse grey bushes which have only little green foliage. At a distance of 25 km to the east, there are the wooded Sacramento Mts. and 40 km to the west, the unwooded Andres and Organ Mts.

During the period of observation, cloudless weather has been experienced only from 31 March through 2 April. On the remaining days the sky has cleared only intermittently being overcast most of the time with cirrus, sometimes also with altostratus and stratocumulus. Several times, gale force winds from SW have carried sand from afar over the observation site. During the observation times, the temperature has varied between 17° and 27°C, the relative humidity between 10% and 30%. During the measurements, the visibility has been always more than 100 km.

Due to the steep slope at two sides of the hill it has been possible to measure the radiation reflected by the plain and its degree of polarization under various azimuth and elevation angles.

At the end of the campaign, measurements have been made in the White Sands gypsum desert which is 15 km off Two Buttes, in order to obtain information on the influence of the incrased reflected radiation on the distribution of the sky radiation and its polarization.

The Aitken nuclei have been counted with the Scholz dust counter and the larger particles have been measured simultaneously with the Royco device.

I. Measurements of the Distribution of the Sky Radiation in the Short Wave and Near Infrared Range (Alamogordo, New Mexico)

1. Measurements of the spectral sky radiation in the sun's countervertical at the azimuth angle $\alpha = 180°$ and the zenith distance $z = 10°$.

Denotations: Z is the zenith distance of the sun, z is the zenith distance of the point in the sky under observation, α is the azimuth angle with reference to the sun, B is the radiance in 10^5 cal/cm^{2}min sr.
Observation sites: T.B. is Two Buttes, W.S. is White Sands.
Wavelengths: 0 is $\lambda = 0.443\ \mu$, 1 is $\lambda = 0.548\ \mu$, 2 is

$\lambda = 0.639\ \mu$, 3 is $\lambda = 0.708\ \mu$, 4 is $\lambda = 0.853\ \mu$, and 5 is $\lambda = 0.911\ \mu$.

The Figure 2 shows results of radiance measurements taken at a zenith distance $z = 10°$ and the azimuth angle $\alpha = 180°$. These measurements have been taken simultaneously with the photographic sky light recordings (Chapter V), in order to give the results in absolute physical units. The figures demonstrate the interdependence of the radiance, the wavelength and the zenith distance of the sun. Since mean values have been presented in the figures, maximal deviations of $\pm$ 12% have been found. It can be seen that the decrease in radiance with increasing wavelength almost follows a power law. Furthermore, it can be concluded that with increasing zenith distance of the sun the radiance continuously decreases at all wavelengths.

2. Measurements of the spectral sky radiation in the sun's vertical and other verticals at different solar elevations.

The results of measurements of the spectral radiance of the sky have been plotted in the Figures 2 - 6 for the sun's countervertical and in Fig. 7 for the sun's vertical up to $z = 30°$. The radiance decreases from the circumsolar region towards the zenith and reaches its minimum in the sun's countervertical. This minimum is the more distant from the sun a) the lower the solar elevation, b) the longer the wavelength. At a high solar elevation, this shift of the minimum reaches about 15° between $\lambda = 0.443\ \mu$ and $\lambda = 0.911\ \mu$.

In the Fig. 8, there have been plotted results of measurements taken along the verticals at $\alpha = 270°$ and $\alpha = 90°$ at a zenith distance $Z = 36°$ pm. The vertical at $\alpha = 90°$ is situated over the White Sands, at $\alpha = 270°$ over the Sacramento

Mts. The increased reflectivity of the White Sands desert effects a well marked brightening up to about 60° over the horizon. This effect is illustrated in Fig. 9 where the spectral radiance has been plotted as a function of the wavelength at a constant zenith distance z = 50° under varying azimuth angles α. There is again evidence of a light brightening of the area in the sky over the White Sands (α = 110°) and bordering regions. It must be admitted that the differences are not great and the measuring accuracy is not sufficient for drawing detailed conclusions on the variations of the radiance as a function of the wavelength.

Fig. 6 represents results of measurements taken at an observation site amid the White Sands desert. Fig. 6 shows that along the sun's vertical the radiance greatly varies with the solar elevation, whereas at 10° over the horizon in the sun's countervertical the values tally in each of the spectral ranges. In agreement with Fig. 7, the differences of radiance between the zenith and the horizon increase with increasing wavelength mainly due to the vanishing influence of the Rayleigh scattering.

The comparison of the radiance measurements in the sun's vertical and countervertical taken at the two observation sites Two Buttes and White Sands has revealed an interesting feature: The expectation that the values found over White Sands would be higher than those over Two Buttes has been met only in the short wave range. The values found in the near infrared over the White Sands are lower than those over Two Buttes.

3. Measurements of the Spectral Sky Radiation in the Solar Almucantar.

The Figures 10 - 21 show measurements of the distribution of the absolute spectral radiance in the solar almucantar which have been carried out from 31 March through 2 April 1967 at the station Two Buttes. They cover the spectral range λ = o.45 μ - o.85 μ and refer to the spectral half-width $\Delta\lambda$ = loo Å. The measurements have been made with a photometer, which had primarily been constructed for measuring the radiation close to the sun (Fin. Techn. Rep. 5 Contr. AF 61(o52)-595). However, it was easy to make a conversion into a device for measuring the radiance along the entire solar almucantar. In order to render the presentation of the results more conspicuous, the distribution of the radiance close to the sun up to a scattering angle φ = lo° has been plotted in a separate graph on a larger scale.

a. Measurements close to the sun, Fig. lo - 21 left side.

All the measurements show a relatively steep ascent close to the sun. A rough estimate based upon a comparison of these measurements with theoretical values (Tables [1]) yields for the same gradient of the curves an upper limiting radius of the aerosol particle size distribution of r $\geqq$ lo μ. The spectral dispersion of the individual sets of measurements corresponds to an exponent $\nu^* \approx$ 4 of Junge's power law for the aerosol size distribution.

A more detailed investigation, however, reveals some noticeable deviations of the individual measurements. In particular the measurements which have been taken on 1 April (Figures 12 - 17) show a considerable increase in the gradient of the curves in the course of the day. The curve for λ = o.548 even intersects that for λ = o.443 μ; the amount of radiance for λ = o.548 μ exceeds that for λ = o.443 μ towards the limb of the sun. Simultaneously, the spectral dispersion of the curves decreases. The physical explanation for both these effects is the discrete increase of the giant particles ($r \gtrsim 1\ \mu$). The exponent of the size distribution has been reduced within the range of these particles, whereas in the range $r < 1\ \mu$, the exponent has hardly changed and can still be assumed to be close to $\nu^* \approx 4$. This is also verified from the analysis of the spectral distribution for $\varphi \geq 10°$ which is described in detail in the next section.

There has not been found any influence of the albedo on the radiance close to the sun. The measurements taken in northerly direction towards White Sands do not show systematical differences from those taken in southerly direction.

b. Measurements far from the sun.

The radiance curves for the entire solar almucantar, which have also been presented in the Figures 10 - 24, have a very small gradient which implies an aerosol size distribution with an exponent ν^* 4.0. The distances of the individual spectral curves also allow the conclusion that $\nu^* > 4.0$. In case of a smaller value of ν^*, the curves in the range $\varphi > 10°$ ought to converge much more rapidly, i. e. the gradient of the curves ought to increase with decreasing scattering angle φ in the long wave range.

Besides this general feature, the individual sets of measurements are characterized by deviations which are due to changes in the turbidity. The measurements taken on 1 April 1967 in the afternoon show an intermittent increase of the absolute values in the infrared range simultaneously with the strong increase of the radiance towards the limb of the sun. This can be explained in the same way as the steepening of the curves: It has been effected by advection of dust particles of $r \geq 1\ \mu$ without an essential change of size distribution in the range $r < 1\ \mu$, for any noticeable increase in particles within the size range $1\ \mu \geq r \geq 0.1\ \mu$ ought to be reflected in the diurnal variation of the turbidity factor.

There is no unbiased evidence of an influence of the great albedo values in the area of White Sands; e. g. the Figures 13 and 14 which refer to almost simultaneous measurements in southerly direction and in northerly direction over White Sands, show an increase in radiance over White Sands. Other measurements e. g. those taken on 1 April and represented in the Figures 15 and 16 do not show this effect. It appears therefore a reasonable assumption to conclude that the brightening of the sky over White Sands, which can be observed from Two Buttes, is not so much due to an increased albedo as due to the scattering effect of gypsum particles liftet up by convection.

c. Measurements in the White Sands Desert.

The Figures 22 - 24 represent results of radiance measurements along the solar almucantar which have been obtained with a nonautomatic photometer. The measurements which are represented in the Figures 22 - 24 have been taken in the early morning; they have been added to supplement the results of the measurements which have been discussed under b. The Figures 25 - 27 show the results of measurements which have been carried out inside of the White Sands gypsum desert. On 8 April (Fig. 25) particles which had been lifted up by the strong wind, effected a great increase of the radiance in the area of the sky close to the sun, especially in the infrared range. Whereas on 9 April, there have been almost calm conditions. The results of the measurements which have been plotted as functions of the scattering angle in the Fig. 26 are throughout higher than those taken at Two Buttes on 28 and 31 March which have been plotted in the Figures 22 and 23 together with measurements taken in the early forenoon for comparison. The raise of the values by about half a power of ten is mainly due to the fact that the reflectivity of the gypsum desert is much higher than that of the normal sand desert.

4. Measurements of the Turbidity Factor.

The turbidity condition of the atmosphere is characterized by the spectral turbidity factor $T(\lambda)$ according to Linke. It is defined as

$$T(\lambda) = (a_D(\lambda) + a_R(\lambda))/a_R(\lambda)$$

where $a_R(\lambda)$ is the extinction coefficient of the mere Rayleigh or molecular atmosphere resp., $a_D(\lambda)$ is the extinction coefficient of the mere aerosol atmosphere. The Fig. 28 shows the diurnal variations of $T(\lambda)$ for the virtually cloudless days from 31 March through 2 April. The turbidity is relatively small and rather constant: Except for a slight continuous increase of the turbidity in the course of the day, no systematic variations can be noticed. The slight increase of the turbidity is due to the convective activity which sets in after sunrise and results in the vertical transport of great amounts of dust into the lower troposphere. The oscillations of the curve at $T(0.847\ \mu)$ are only seeming due to the inaccuracy of the measurements which increases with increasing wavelength.

The Fig. 29 shows daily mean values of the aerosol extinction $a_D(\lambda)$ which have been computed from the turbidity factors presented in the Fig. 28. The aerosol extinction $a_D(\lambda)$ has been plotted as a function of λ and shows a normal behavior. In this case, Ångström's wavelength exponent α falls in between $\alpha \approx 1.3$ and $\alpha \approx 1.8$. According to Volz [2] this would result in $\nu^* = \alpha + 2$, thus ν^* between 3.3 and 3.8.

The reduction of the turbidity measurements has been based upon the assumption of o.25 cm ozone over the observation site.

II. Measurements of the Radiation Reflected by the Surface of the Earth in the Short Wave and Near Infrared Range (Alamogordo, New Mexico)

The radiation which is reflected by the surface of the earth makes an essential contribution to the sky radiation. Its values vary considerably according to the properties of the ground. In the visible wavelengths, fresh snow reflects almost the entire incident radiation, however, sandy soil only about 25%. Because of the rather uniform ground conditions in the surroundings of the observation site at an elevation of 115 m above MSL, it has deemed appropriate to investigate the reflectivity in different directions and at various solar elevations. The measurements have been taken at the following zenith distances: z = 92°, 95°, 1oo°, 1o5°, and 11o°, i. e. at 2°, 5°, 1o°, 15°, and 2o° below the horizon. Basically, the measurements taken at small angles are biased by the atmospheric light between the observation site and the sight. However, due to the extraordinary transmissivity of the atmosphere in this area (visibility always > 1oo km) this interference can be neglected. Due to the angle of view of 4° of the photometer, the measurements taken at z = 92° undergo an additional influence by the radiance of the horizon.

The Figure 3o shows the results of measurements taken at high solar elevations. The radiance values are highest for the red wavelengths. The physical explanation is the reddish brown color of the sand with the grey sparse brushwood almost lacking a green foliage. The reflected radiation increases from $\alpha = 36o°$ towards $\alpha = 18o°$.

Different results can be seen in the Figure 31 which represents the measurements taken in 2 April, with Z = 58° pm. The well marked maximum at $\alpha = 18o°$ implies predominating backward reflection of the soil. The maximum is found at $\lambda = o.7o8\ \mu$, the minimum at $o.443\ \mu$.

The measurements taken on 4 April at Z = 66° am which are presented in Fig. 32, are characterized by two well marked maxima, one at z = 0° and the other one at z = 18o°, the latter becomes indistinct already at z = 1oo°. Partly the values considerably differ from those of the Figures 3o and 31, due to the different angles of incidence according to the different positions of the sun at Z = 59° pm and Z = 66° am. E. g. the surface under the angle $\alpha = 0°$ is always underneath the sun, however, it is not always the same surface varying with the position of the sun, i. e. there have always been the same areas of the ground under investigation, however, according to the varying angles of incidence at varying positions of the sun they have been related to different values of α.

Another series of measurements has been taken shortly before noon on 4 April, which is presented in the Figure 33. As for the position of the sun, the situation was similar to that of the measurements taken on 2 April, which are presented in the figures. Indeed, in principle the curves resemble, except for an azimuth shift of about 15° due to the difference in the solar elevations of 12°. However, on 4 April the sky has during noontime been covered with a light cirrus veil which slightly changed the global radiation.

The last series of measurements (Fig. 34) has been taken in the early afternoon of the 4 April with Z = 34° and 10/10 cirrus and stratus. The results are therefore not comparable with the other ones. Furthermore, the observation site has been changed in such a way that the sights could be aligned on the ground beyond the mountain for finding out about eventual differences in the reflectivity. In spite of this change, the results in principle resemble those described previously. The greater the zenith distance, i. e. the steeper downward the bearing, the more shifts the maximum of the reflected radiation towards the long wave range. But the values at $\lambda = 0.9\ \mu$ hardly change any more.

Summing up: The reflected radiation is mainly red, however, at $\lambda = 0.9\ \mu$ mostly of lesser intensity than in the blue wavelength. The maximum values amount to about $100 \cdot 10^{-5}$ cal $cm^{-2}min^{-1}sr^{-1}$ for z > 95° in the red wavelengths. This corresponds to the sky radiation at a distance of about 10° from the sun. The minimum values amount to about 30×10^{-5} cal $cm^{-2}min^{-1}sr^{-1}$ in the red wavelengths. This corresponds to the sky radiation at a distance of about 30° from the sun in the solar almucantar at mean solar elevations.

III. Measurements of the Degree of Polarization of the Sky Radiation in the Short Wave and Near Infrared Range (Alamogordo, New Mexico)

Fig. 1 is again the locator map.

Fig. 35 shows the results of measurements which have been taken on 31 March and 2 April at the observation site Two Buttes. Z again denotes the zenith distance of the sun, z is the zenith distance of the sky light, α is the azimuth angle with reference to the sun, P is the percentage degree of polarization, 0 is the wavelength $\lambda = 0.443\ \mu$, 1 is $\lambda = 0.548\ \mu$, 2 is $\lambda = 0.639\ \mu$, 3 is $\lambda = 0.708\ \mu$, 4 is $\lambda = 0.853\ \mu$, and 5 is $\lambda = 0.911\ \mu$. (Unless otherwise noted, z denotes always the zenith distance in the sun's counter-vertical α 180°.) T.B. denotes the observation site Two Buttes, W.S. means White Sands.

The degree of polarization reaches its highest degree at the lowest solar elevation. The value of 75% which has been found on 2 April at a wavelength 0.443 μ represents a maximum that corresponds best to the condition of the mere molecular atmosphere. The wavelength dependence, especially close to the polarization maximum, is well marked and stronger than e. g. in Greenland or in Hawaii. The portion of incident radiation which is reflected by the surface of the earth contributes to diminishing the degree of polarization. The reflected radiation is in the order of magnitude of the sky radiation due to the reddish sandy desert soil covered with sparse dark and mostly dry brushwood, see Chapter II. The measurements taken on 31 March yield lower values due to the weather: A strong wind had lifted sand particles up to a height above the observation site.

Fig. 36 shows the results of measurements taken in the middle of the White Sands. The area of this bare gypseous desert is limited, however, its very high albedo - see Chapter IV - effects a noticeable lessening of the degree of polarization. This effect is manifested by a series of measurements of the degree of polarization of the sky radiation taken during noontime at Z = 28.5° and z = 50° over the White Sands at a distance of about 2o km with $\alpha = 130°$ and over the Sacramento Mts. with $\alpha = 230°$, listed in Table 1.

Table 1: Percentage Degree of Polarization of Sky Radiation in the Direction of White Sands ($\alpha = 130°$) and Sacramento Peak ($\alpha = 230°$) and in Between ($\alpha = 180°$). Observation Site: Two Buttes; $Z = 28.5^0$, $z = 50°$.

λ	α	13o°	18o°	23o°
o.443 μ		39	51	43
o.639 μ		33	44	34.5
o.7o8 μ		3o	3o.5	32
o.911 μ		19.7	27.3	22.2

The table proves that the degree of polarization in the direction of the White Sands is smaller than that in the direction of the mountains, though the azimuth angle with reference to the sun is the same. Thus it is obvious that this influence goes up to a height of 4o° above the horizon.

Fig. 37 represents the results of measurements of the degree of polarization in the azimuth angle range from 18o° up to 26o°; they prove that the maximum of polarization is located as a broad band in the sky opposite the sun. It is to be expected that two weak secondary maxima occur outside of the sun's countervertical.

Furthermore, the Figures 35 through 37 indicate a marked wavelength dependence of the degree of polarization in the sun's countervertical. It is strongest in the range of maximum polarization and lessens near the horizon. It must be noted that with increasing z the degree of polarization shows a greater decrease in the short wave than in the infrared range.

In the Figures 38 and 39, measurements have been plotted as functions of the wavelength. The results are valid for points in the sky in the sun's countervertical at a distance from the sun of about 8o°, i. e. in the area of maximum polarization. The wavelength dependence varies with Z and z. Generally, it is obviously less marked in the short wave range than at $\lambda > 0.6\ \mu$.

IV. Measurements of the Degree of Polarization of the Radiation Reflected by the Surface of the Earth in the Short Wave and Near Infrared Range (Alamogordo, N.M.)

The Figures 4o and 41 show measured degress of polarization of radiation which has been reflected by the desertlike soil. The zenith distances have been taken as follows: 92°, 95°, 1oo°, 1o5°, and 11o°, i. e. 2°, 5°, 1o°, 15°, and 2o° below the horizon. Furthermore, the measurements have been taken at different azimuth angles and different wavelengths. All the results of these measurements have one feature in common: The degree of polarization is greater in the short wave than in the long wave range. In the near infrared, it almost goes down to 0.

The azimuth dependence of the degree of polarization can be seen from Fig. 4oa at a zenith distance of 95° at a high solar elevation. In the blue light, the degree decreases from 25% at $\alpha = 0°$ (underneath the sun) to 12% at $\alpha = 18o°$. Already in the green light, the degree of polarization of the reflected radiation is considerably less; in the infrared range it reaches but a few percent and the azimuth dependence disappears.

The zenith dependence of the degree of polarization can be seen from Fig. 4ob. This interdependence is noteworthly. The elevation of the observation site is 115 m above MSL; when the zenith distance z is only 2° below the horizon, the reflected radiation stems from a distance of 3.16 km.

z =	9o° corresponds to a distance of	∞ km
	91°	6.52
	92°	3.16
	94°	1.37
	95°	1.15
	1oo°	o.65
	1o5°	o.43
	11o°	o.316
	115°	o.246

The atmospheric layer between the observer and this specific distance effects a degree of polarization of the reflected light which almost equals that of the sky on the horizon, see Fig.38 4. With increasing zenith distance of the point under observation, this influence lessens, and finally, the degree of polarization goes almost down to 0. It is worthwhile mentioning the strong wavelength dependence of the results at the zenith distances between 92° and 11o°. This greatly differs from that of the polarization of the sky light near the horizon where the spectral differences are negligible.

Similar results are presented in Fig. 41a, however, a remarkable feature shows up: At a high solar elevation (4ob) and α = 0° (terrestrial reflection underneath the sun) the degree of polarization has reached its maximum at z = 92°, whereas the reverse is true at a low solar elevation. Furthermore, in the latter case the spectral differences disappear, whereas at a high solar elevation, they have been at a maximum.

Another way of presentation has been chosen for Fig. 41b. The degree of polarization of the reflected radiation has been plotted as a function of the zenith distance z for 4 wavelengths and 3 azimuth angles. The polarization decreases rapidly from the short wave towards the long wave range and is hardly measurable in the infrared. At $\lambda = 0.443\ \mu$, the degree of polarization is highest at $\alpha = 90°$, whereas at longer wavelengths, the values practically do not differ any more. As a matter of fact, it must be mentioned that on the day when this measuring series has been taken, namely 4 April, cirrus clouds have changed the spectral distribution of the solar and sky radiation with respect to clear days.

The degree of polarization of the reflected radiation goes down to 0 when the atmospheric light is eliminated. This has been proved by a polarization measurement of a sandy debris area situated but 8 m underneath the observer ($z = 129°$).

V. The Distribution of the Spectral Radiance of the Entire Sky in New Mexico at Alamogordo (Photographic Measuring Method).

The distribution of the spectral radiance has been measured by means of photographs of a spherical mirror according to the method by Plass [5]. Ca. 4000 grid points of each photograph have been measured by automatic photometry and evaluated with the Siemens 2002 computer.

The Figures 47 ~~and~~ above show relative values at the blue and red wavelength which stem from photographs taken at the observation site Two Buttes on 2 April 1967. The value in the sun's countervertical at the angle of azimuth $\alpha = 180°$

and the zenith distance z = 1o° has been set 1oo. Simultaneous measurements of the radiance in absolute physical units enable one to convert the relative values into absolute ones.

Except for small deformations, the intensity distribution at the blue wavelength is almost symmetrical for both spheres of the sky. At the red wavelength, the symmetry is deranged due to the predominant effect of the radiation reflected by the reddish desert soil. In spite of the very small turbidity a distinct dependence of the measured values on the wavelength can be seen. The decrease in intensity is more marked in the red than in the blue wavelength. This is due to atmospheric aerosol particles which can possibly be concentrated in higher layers of the atmosphere. Details on this connection can be given no sooner than in the next Report.

The Figure 47 below shows results which have been obtained on 9 April 1967 at the observation site in the White Sands desert, during calm condition. The results resemble those obtained at Two Buttes; a physical explanation of the deviations can be given only after a careful consideration based upon the values in absolute units.

The Fig. 48 shows results of the 8 April 1967 obtained in the White Sands desert during a fresh breeze. While taking the photographs, the observer has seen sheets of blowing sand above him. They underwent so rapid changes that no comparison can be made with the following photographs taken at different wavelengths. Firstly, the figure shows a greater gradient of the radiance of the sky than during undisturbed conditions. Secondly, the configuration is not smooth; the isolines have many indentations and protrusions. The evaluated results of the sky photographs which have been presented here, prove the qualification of the photographic method for recording the radiance distribution over the entire sky at a specific moment.

VII. Measurements of the Number and Size of the Atmospheric Aerosol Particles (Alamogordo, N.M.)

In order to get an insight in the aerosol particle size distribution near the ground in New Mexico the Aitken nuclei have been measured with the Scholz dust counter at the observation site Two Buttes. The counter catches the particles within the radius interval from $3 \cdot 10^{-3}$ μ through 0.1 μ. Furthermore, a Royco device of the Meteorological Institute at the Munich University has been used for counting the particles of the following five radius ranges: 0.3 - 0.64 μ, 0.64 - 1.5 μ, 1.5 - 3 μ, 3 - 6 μ, and 6 - 15 μ.

The Fig. 44 shows some results of measurements of the number of Aitken nuclei per cm^3. The number of the particles with a radius < 0.1 μ is subject to variations which a physical explanation cannot be given for but with the help of a long term measuring series. It has been observed that the number of particles is reduced when during the daylight hours the wind freshens up due to convectional activity. More particles have been counted in calm than in windy weather. Moreover, there is no connection between the visibility and the number of these particles with a radius < 0.1 μ. Recently F. Kasten [3] has proved in a quantitative theoretical investigation that these small particles do not influence the transmissivity of the atmosphere. (In spite of that it is not admissible to make the statement that the particles with a radius r < 0.1 μ have no optical effect as it has sometimes been done; for e. g. they strongly influence the spectral distribution of the sky radiation.) With regard to the thinly populated area of New Mexico the number of particles with a radius r < 0.1 μ appears to be rather high; it is by one order of magnitude higher than e. g. in Hawaii.

In order to get an insight in the decrease of Aitken nuclei with height measurements with the Scholz dust counter have been taken during a trip in the Sacramento Mts. At 1.640 m above MSL on the <u>windward</u> side there have been counted $4.3 \cdot 10^4$ particles; at 2.080 m just below the timber line $4.1 \cdot 10^4$ particles; at 2.500 m on a by-way within the timber forest at a distance of some hundreds of meters from the highway $2.1 \cdot 10^4$ particles, at 2.660 m in the forest far from the unfrequented highway still $9 \cdot 10^3$ particles. Even on the Sacramento Peak at 2.720 m there have been found still 7.000 particles. In the <u>lee</u> area of the Sacramento Mts. smaller numbers of Aitken nuclei have been obtained, namely at 2.240 m in the forest 3.000, at 1.830 m in May Hill in the dwarf-pine wood also 3.000. On the way back in the <u>windward</u> region there have been counted 5.000 particles at 2.300 m and 21.000 particles at 1.740 m.

This measuring series allows to draw the conclusion that on the windward side of the high mountains the number of Aitken nuclei remains constant up to rather great heights and decreases towards the leeside.

The Fig. 45 shows some results of the measurements of the number of aerosol particles which have been taken with the Royco counter on 7 April at short time intervals between 0930 and 1700 o'clock. This instrument had a rate of flow of 3 liters of air per minute. Obviously, the number of particles undergoes great variations with time, especially in the ranges 4 and 5, i. e. in the range of the large particles. During the measuring time, gusts from SW have occurred. The circles in the figure represent very high counts which have been valid only for very short periods of time and which do not match the remainder of the measurements.

A series of measurements which has been taken on 8 April between 1130 and 1230 o'clock has been plotted in Fig. 45 . The time scale, which is represented by the ordinate, has been slightly enlarged in comparison with Fig. 45 . Both these series of counts are characterized by great variations in time. Furthermore, the increase and decrease of particles obviously have a parallel trend in all five radius ranges. Of course, there are some exceptions as e. g. the increase of the small particles within the range 1 coincides with a decrease of the large particles and vice versa.

The consecutive groups of measured values have been averaged by logarithmic way and the numbers of particles thus obtained have been plotted in the Figures 42 and 43 as functions of the particle radius. In order to compare them with the counts of the Aitken nuclei per cm^3 they have to be divided by $3 \cdot 10^3$. In contrast to the Figures 45 and 46 , the values of the Figures 42 and 43 are very well organized. The decrease of the large particles follows the power law $r^{-1.6}$ between the radius interval o.4 μ and 2 μ; towards larger radii the increase lessens. The families of curves, which lie one beneath the other, show the same trend as in the Figures 45 and 46 which is characterized by a decrease in time of the particles in all the radius intervals The numbers of particles have been measured with a Royco device. Then, the radius interval from o.o6 μ through o.44 μ at 115 m above ground would be characterized by a power law of r^{-4} *). Radiation measurements have yielded a r^{-4} relationship for the entire atmosphere. The deviation in the radius range o.44 - 1o μ implies that on 7 and 8 April some large desert dust particles have been lifted up into the lower atmosphere by the strong wind.

---

*) The method to incorporate particles r < o.1 μ into the Royco analyse results is given by C. Junge [4].

B. Experimental and Theoretical Investigations into the Spectral and Angular Dependence of Reflectivity and the Degree of Polarization of Reflected Radiation of Various Soil Types.

I. Reflectivity of Ground but not Polished Limestone, Fine and Coarse Grained Soil at Acute Angles of Incidence of the Light Source (Angles of Incidence $\Theta_o = 30°$ and $\Theta_o = 60°$).

The reflectivity at $\Theta_o = 30°$ has been plotted in polar coordinates in the Fig. 60, namely for the fine grained sample (a and b) and the coarse grained sample (c and d). The feature which all the graphs have in common is the distinct predominance of backward scattering over forward scattering. The fine grained sample has a minimum at the angle of observation $\Theta = 45°$ and $\alpha > 140°$ at both wavelengths, namely 30% in the green and 40% in the red wavelength range. The maximum values of the coarse grained sample have almost the same amounts, namely 60% - 80%, as those of the fine grained sample, whereas the minimum values are much less, namely 22.5% in the green and 27.5% in the red wavelength range. The latter are also shifted towards the angle of observation $\Theta = 60°$ and $\alpha > 170°$.

The Fig. 61 has the same contents and arrangement as the Fig. 60, however, referring to $\Theta_o = 60°$. The curve patterns for the fine grained sample (a and b) resemble those in the

Fig.60 , but the maximum values amounting to 90% in the green and to 110% in the red wavelength range are higher than those for $\theta_0 = 30°$. Whereas the minimum values are lesser than those in the Fig.60a,b namely 22.5% in the green and 30% in the red wavelength range. The latter have undergone a displacement towards the angle of observation $\theta = 75°$ and $\alpha > 150°$.

The values of the coarse grained sample (c and d) in the Fig.61 are throughout lower than those of the fine grained sample by about 10%.

The results for the ground but not polished limestone are presented in the Fig. 62a and b for $\theta_0 = 30°$. Uneven parts of the limestone plate cause a more unregular pattern of the isolines than that of the grainy samples. The gradient is lesser, maxima and minima differ by only about 20%. At $\theta = 0°$, the minimum has 45% in the green and 52.5% in the red wavelength range. The maxima are again located near the horizon, however, at angles of azimuth $\alpha > 90°$.

II. Measurements of the Reflectivity of Gypseous Sand as well as Red and Grey Quicksand in the Environs of Alamogordo, New Mexico.

Results of measurements of the reflectivity and the degree of polarization of reflected radiation of calcareous soil of varying texture have been presented in the Scientific Report No 5 and in the first section of this Chapter. The same apparatus has been used to supplement the results presented in the Chapter A of this Report by measurements of the reflectivity of samples of desert sand which have been taken in New Mexico near Alamogordo. The radius of the grains of gypseous sand from White Sands has been $r \ll 1$ mm, whereas the red and grey grains of quicksand had radii of $r \leq 1$ mm.

a) Measurements of the Reflectivity.

The Figures 49a-c show the distribution of the reflectivity of the three samples for the wavelength λ = o.444 μ. The angle of incidence of the light source is Θ_0 = 3o°. As was to be expected the values for white sand (gypsum) are highest. The minimum which amounts to 55% is found at the angle of azimuth α = 0° and the angle of observation Θ = 3o°, i. e. in the range of backward scattering. The minimum for red sand which amounts to 14% is shifted to the angle Θ = 0°, i. e. the zenith. The values for grey sand are similar. The effect of forward scattering is strongest for white sand.

In the Figures 50a-c, the isolines for λ = o.647 μ have been plotted. The pattern resembles that of the blue wavelength, however, the values of the reflectivity are higher by the factor 1.5 to 3.

The Figures 51a-c show the measurements for the wavelength λ = o.78o μ which very much resemble those for λ = o.647 μ; the reflectivity increases by 3% for white sand and by 5% for red and grey sand.

The Fig. 52 shows the reflectivity for the angle of incidence of the light source Θ_0 = 6o° again for each of the three soil samples in the blue wavelength. The results differ only slightly from those at Θ_0 = 3o°, however, there are a few interesting deviations, e. g. the maximum value for gypseous soil is slightly lower and for colored soil by a few percent higher.

The Fig. 53 refers to the same value of θ_o = 6o° but for the wavelength λ = o.78o μ. Again, the changes in the reflectivit. are very small. A striking feature of the grey soil sample is the backward scattering which is caused by the relatively larger grains of sand. The comparison with the measurements taken at λ = o.444 μ reveals a greatly different pattern of distribution and much greater amounts of the values of λ = o,78o μ than of the blue light.

In the Fig. 54, the measurements of the reflectivity have been plotted for the light source's vertical (α = 0° and α = 18o°) as functions of the angle of observation θ for three wavelengths and three soil samples. The angle of incidence of the light source is θ_o = 3o°. In each case the reflectivity is greatest at θ = 9o° amounting to values about 1oo% for gypsum. It can be seen again that the reflectivity is greatest in the near infrared. The position of the minimum can best be recognized in the Fig. 55.

The parameters in the Figures 55a and b are the soil samples, in the Fig. 55a for λ = o.444 μ, in the Fig. 55b for λ = o.647 μ, whereas the Fig. 55c shows the measurements taken at the angle of azimuth α = 9o°. The values of all the three soil samples show a gradual slow increase from the zenith towards large angles of observation. The measurements of the reflectivity at θ_o = 3o° and θ = 0° have been plotted in the Fig. 55d as functions of the wavelength. All the soil samples show a decrease in reflectivity with decreasing wavelength, especially is this true with gypsum. The sample of red sand has a greater reflectivity at the red wavelength than the grey sand.

The Fig. 56 refers to the angle of incidence of the light source θ_o = 6o° and the parameters are the same as in the

Fig. 54 , namely the three wavelengths. The main maximum for gypsum is located at $\Theta = 30°$ and $\alpha = 180°$. A secondary maximum shows at $\Theta = 90°$; at $\lambda = 0.444\ \mu$ the amount of this secondary maximum exceeds that of the primary maximum at $\Theta = 30°$. The sample of red sand shows an increase of the values only in the angle range $\Theta > 40°$ ($\alpha = 180°$) at $\lambda = 0.444\ \mu$; this effect is more pronounced than at $\Theta_0 = 30°$. The maximum of the reflectivity of the sample of grey sand is located at $\Theta = 70°$ and $\alpha = 0°$. At the red wavelength, the reflectivity slowly decreases with decreasing scattering angle; this decrease is very similar for both $\lambda = 0.444\ \mu$ and $\lambda = 0.647\ \mu$. At $\Theta = 90°$ ($\alpha = 180°$) a secondary maximum can be observed.

The parameters in the Figures 57a and b are the same as in the Fig. 55, namely the soil samples. The angle of incidence of the light source is $\Theta_0 = 60°$. Again, a striking feature of the measurements is the great diversity in the dependence of the reflectivity on the angle of observation which is true with all the three soil samples.

b) Measurementsof the Degree of Polarization of the Reflected Radiation.

The Figures 58 ($\Theta_0 = 30°$) and 59 ($\Theta_0 = 60°$) show the measurements of the degree of polarization of reflected radiation as a function of the angle of observation Θ; the parameters are the three wavelengths which the measurements have been taken at. All the results have a feature in common, namely small negative values of polarization at scattering angles about 180°, i. e. in the range of backward scattering. In each case, the highest degree of polarization is found at $\lambda = 0.444\ \mu$. The sample of red sand has the highest values.

The gypsum shows but small differences at the three wavelengths. With the exception of the grey sand, the maximum is found at $\theta_0 = 60°$, $\theta = 90°$ and $\alpha = 180°$.

A physical explanation for the variation in reflectivity could be given so far only for calcareous soil, see Section III of this Chapter. Only the sample of grey sand shows a behavior which resembles that of calcareous soil in variation with the angle of observation.

These laborator measurements will be used for finding a physical explanation for the spectral radiance distribution of the desert soil as it has been measured at the observation site Two Buttes. However, the results can be given no sooner than in the next Report.

III. <u>On the Computation of the Reflectivity</u>.

It has already been mentioned before that all the mineralogical constituents of the soil samples under investigation have a crystalline structure. Thus, their indices of refraction depend on the angle of incidence of the light source. Furthermore, quartz and mica turn the polarization plane of the incident ray. Thus, it is hardly feasible to make any statements on the size distribution of the samples or the absorptivity of the limestone or its sediments in the visible spectrum. Therefore, the computation of the reflectivity raises problems which are too complex for being solved straightway. A first step will be done in this Chapter by restricting the computation to non-compact particles and by neglecting double refraction and absorption. Furthermore, the light source is assumed to supply unpolarized light.

1. General Description of the Problem.

The reflectivity of a soil surface mainly depends on the shape and size of the individual particles. If the particle diameter is small compared to the wavelength of the incident radiation under investigation the scattering of light follows Rayleigh's law. The scattering on particles whose diameter is of the same order of magnitude as the incident radiation is determined by the Mie theory. The scattering on larger particles can be computed with the laws of geometric optics under the condition that these particles have a geometrically simple form.

The above laws can be applied only under the assumption that no extinction takes place inside the particles, i. e. the particles are assumed to be opaque. Now, the larger particles of the soil samples under consideration consist of a great number of small particles which effect a great scattering within their parent particle. Thus, the large particles give the impression as if they were opaque though their constituents are possibly transparent. This opacity implies a strong absorption, however, a simple experiment proves that this assumption is not verified.

The main constituents of the samples under investigation are calcareous spar or crystalline quartz.~~calcareous spar and quartz~~. Since they are nonabsorbent, they appear colorless to the eye in the visible spectrum. If however, the crystals are triturated, the powder turns white and becomes opaque. This can be explained only with scattering. The great variety of forms of the particles renders a great possibility for angles of incidence upon the boundary layer between a particle and the ambient air which surpass the angle of total reflection, under the assumption of an adequate thickness of the crystal powder layer. Yet the coalescence of many individual particles forms a conglomeration which due to shadowiness has optical properties not in conformity with the laws described in the beginning of this paragraph.

Generally, each soil sample has a very broad particle size spectrum so that the computation of the reflection must be based upon the consideration of scattering processes on particles with different diameters in different directions. This requires the knowledge of the size distribution of the samples as well as the consideration of the behavior of the individual parameters. Therefore, the following discussion is restricted to the reflection produced by media with a specific limited range of particle size. The aim is the computation of the reflectivity $R(\theta_o, \theta, \alpha)$ of an infinitely thick medium under the assumption of various scattering processes occurring within this medium; θ_o denotes the angle of incidence of the light source, θ the angle of observation, and α the angle of azimuth. Then, it will be tried to give a physical explanation of the measurements with the help of these computations. It will be proved that it is admissible to employ this special measuring device for the comparison with the reflectivity of an infinitely thick medium.

For being brief, the present Report is restricted to the presentation of the computational results.

2. Definition of the Reflectivity.

The albedo A of a surface element

$$A(\theta_o, \lambda) = d\phi_R(\lambda)/d\phi_o(\lambda) \qquad (1)$$

is defined as the ratio of the radiant flux reflected by the surface:

$$d\varnothing_R(\lambda) \quad [\text{cal sec}^{-1}]$$

to the radiant flux incident upon it: $d\varnothing_o(\lambda)$.

The reflectivity R is expressed as

$$R(\theta_o,\theta,\alpha,\lambda) = \frac{B_R(\theta_o,\theta,\alpha,\lambda)}{I_o'(\lambda)} \quad [\text{sr}^{-1}] \qquad (2)$$

i. e. the ratio of the radiance B_R [cal cm^{-2} sec^{-1} sr^{-1}] reflected by a given surface under a specific angle of reflection to the total irradiance $I_o'(\lambda)$ [cal cm^{-2} sec^{-1}] that is incident upon that surface.

The albedo A and the reflectivity R are related as follows

$$\int_{\Omega} R(\theta_o,\theta,\alpha,\lambda) \cos\theta \, d\omega = A(\theta_o,\lambda) \qquad (3)$$

In case of ideal diffuse reflection (Lambert's surface) a surface has a constant reflectivity R_S. Furthermore, the ideal Lambert's reflector is characterized by the relation

$$\pi R_S = A_S = 1 \qquad (4)$$

The product $\pi R(\theta_o,\theta,\alpha,\lambda)$ which refers to a nondiffusing surface, can therefore be interpreted as the ratio of the radiance reflected by the nondiffusing standard surface to the radiance reflected by the ideal diffusing standard surface. In specific directions, πR can be greater than 1, i. e. in the direction (θ,α) a greater radiance is emitted than in case of the standard surface.

3. Reflection by an Infinitely Thick Medium.

3.1. Basic Equation for Primary Scattering.

The prerequisite is an infinitely thick medium with a plane surface upon which a collimated monochromatic beam of light is incident. The medium is assumed to be homogeneous, i. e. the scattering coefficient $\sigma'(\lambda)$ [cm^{-1}] is constant within the entire medium. The term $f'(\varphi,\lambda)$ [cm^{-1} sr^{-1}] denotes the scattering function of the unit volume (φ is the scattering angle, λ is the wavelength) For primary scattering, the reflectivity is then expressed as

$$\pi R(\theta_o,\theta,\alpha,\lambda) = \pi \frac{f'(\varphi,\lambda)}{\sigma'(\lambda)} \frac{100}{\cos\theta_o + \cos\theta} \, [\%] \quad (5)$$

Thus, the reflectivity depends only on the ratio of the scattering function to the scattering coefficient and a geometric factor, namely $1/(\cos\theta_o + \cos\theta)$.

According to (3) the albedo is expressed as

$$A(\theta_o,\lambda) = \frac{1}{\sigma'(\lambda)} \int_o^{2\pi} \int_o^{\pi/2} f'(\varphi,\lambda) \frac{\cos\theta \cdot \sin\theta}{\cos\theta_o + \cos\theta} \, d\theta \, d\alpha \quad (6)$$

3.2. Reflection According to Lommel/Seeliger's Law.

Seeliger's law describing the radiation I_R [cal cm^{-2}] reflected by a given surface is express

$$I_R(\theta_o,\theta) = \frac{k}{a} I_o \frac{\cos\theta_o \cos\theta}{\cos\theta_o + \cos\theta} \quad (7)$$

where a denotes the extinction coefficient and k a constant.

In this way the reflectivity R of the given surface may be written

$$R(\theta_0,\theta) = \frac{k}{a}\,\frac{100}{\cos\theta_0 + \cos\theta}\,[\%] \qquad (8)$$

The absorption of radiation by individual soil elements can be neglected in the visible part of the spectrum; therefore, the extinction coefficient a can be substituted with the scattering coefficient σ'. Then, the consolidation of the equations (5) and (8) results in $f'(\varphi.\lambda) = k$. This means that the prerequisite of Lommel/Seeliger's law is a constant scattering function of a unit volume, i. e. isotropic scattering processes within the medium.

Futhermore, the theory implies the relation $k/a = 1/4\,\pi$. Thus, R is independent of the wavelength. The dependence on λ is only due to taking absorption into account.

3.3. Reflection in Case of Rayleigh and Mie Scattering.

It is assumed that the light is scattered on the molecules within the model medium defined in para 3.1. Then, with Rayleigh's equations for f' and σ' it is obtained

$$\pi R(\theta_0,\theta,\alpha) = \frac{3}{16}\,\frac{1+\cos^2\varphi}{\cos\theta_0 + \cos\theta}\cdot 100\,[\%] \qquad (9)$$

Besides a numerical factor, the equation (9) consists of cosine functions only. This implies that under the assumption of primary scattering the reflectivity of a molecular medium of infinite thickness is also independent of the refractive index and the density of the molecules.

The equation (9) is not restricted to molecular media only. It holds for all media if the phase function of the unit volumes is proportional to $(1 + \cos^2 \varphi)$.

Now it is assumed that the scattering process within the model medium follows the Mie theory. For such a medium with a specific size distribution, the reflectivity is expressed

$$\pi R(\Theta_o,\Theta,\varphi,\lambda) = \frac{\int_{r_1}^{r_2} i(\varphi,\alpha)\,d\,N(r)}{\frac{1}{2}\int_{r_1}^{r_2}\int_0^{\pi} i(\varphi,\alpha)\sin\varphi\,d\varphi\,dN(r)} \; \frac{100}{\cos\Theta_o + \cos\Theta} \; [\%] \qquad (10)$$

where $i(\varphi,\alpha)$ denotes the Mie function and α the parameter $2\pi r/\lambda$.

3.4. Reflection by a Medium Consisting of Large Particles.

For large spherical particles, the Mie function can be simplified by the laws of geometric optics and diffraction (se. van de Hulst [6]). However, diffraction applies only to forward scattering. And it may be neglected for scattering angles down to about 30°. Since the diffraction furnishes an essential contribution to the entire scattered light, it must be taken into account for the computation of the scattering coefficient σ. There is evidence from computations that the proportion of the entire scattered light due to diffraction is directly proportional to at least the square of the particle radius and inversely proportional to at least the square of the wavelength. The contribution which the terms of the geometric optics furnish to the scattered light is independent of r and α. According to the equation (5) it must be concluded that the reflectivity decreases with increasing particle radius and increases with increasing wavelength. This dependence of the reflected radiation on the wavelength and the particle radius holds also for nonspherical particles if it is assumed that their surfaces are composed of a number of convex projections.

4. Comparison Between Measurements and Computational Results.

4.1. Prerequisites.

The comparison between computed and measured values of reflectivity is limitative due to multiple scattering. Furthermore, the geometric design of the apparatus does not enable one to measure the reflectivity in a specific direction (α,φ). On the contrary, an average reflectivity is obtained in the directions $(\alpha,\varphi \pm \Delta\varphi)$. This error makes itself felt especially in case of large angles of observation. An integration of the values of reflection over the different directions of reflection has not been made due to the laborious mathematical approach. Therefore, at great angles θ, an exact adjustment of the computational model to the measuring conditions cannot be expected even if the contribution of multiple scattering is exactly included in the computation. However, this error is small if the values of the scattering function do not differ much in the individual directions.

The mean range $w = 1/\sigma$ of the radiation within the samples which have been used for this investigation, has been less than o.5 cm for the fine grained sample and less than 1 cm for the coarse grained one. The thickness of the samples has been 5 cm; since this quantity affects all the measurements, it is not necessary to consider the proportion of radiation ΔI which reaches down to the bottom of the measuring receptacle. A scientific estimate implies that ΔI is less than 1% of the total radiation which contributes to the reflection. Hence the discrepancy between the theoretical requirement and the measuring device is so small that the comparison with the reflectivity of an infinitely thick medium is admissible.

4.2. Evaluation of a Scattering Function From the Measurements.

The attempt is made to use the measurements of the reflectivity for finding a scattering law which is valid for the soil samples under investigation. The equation (5) can be solved for f'/σ' as follows

$$\pi f'(\varphi,\lambda)/\sigma'(\lambda) = (\cos\Theta_0 + \cos\Theta)\ \pi R(\Theta_0,\Theta,\alpha) \quad (11)$$

The computations have been made for the coarse soil sample for the wavelength $\lambda = 0.545\ \mu$. The measured values of $\pi R(\Theta_0,\Theta,0.545\ \mu)$ for various angles of incidence in the light source's vertical have been used in the equation (11) in order to compute the values of the reduced scattering function. The latter have been multiplied with the factor $100\cdot\pi$, and these percentages have been plotted in the Fig. 64 as functions of the scattering angle.

The Fig. 64 proves that the scattering function shows a correlation with the scattering angles which is similar for all angles of incidence. An estimate of the effect of multiple scattering tends to prove that the influence of multiple scattering on the reflected radiation decreases with increasing angle of incidence. The empirical evaluation of the reduced scattering function has therefore primarily been based upon values computed for $\Theta_0 = 75°$. It can be seen from the graph that the numerical values for $\pi\cdot 100\ f'/\sigma'$ (marked by crosses) which have been evaluated with the measurements taken at an angle of incidence $\theta_0 = 75°$ deviate only slightly from the function

$$\pi 100\ f'(\varphi, 0.545\mu)/\sigma'(0.545\ \mu) = 30\ (1 - \cos\varphi) \quad (12)$$

The function (12) has also been plotted in the Fig. 64 and it is obvious that also those values which have been computed from other angles of incidence are closely fitted around this curve. Greater deviations (broken curves) occur at any angles of observation near $\theta = 90°$. This is due to a strong increase of the multiple scattering.

4.3. Reflection by a Medium Whose Scattering Function is Proportional to $(1 - \cos\varphi)$.

Vice versa, the reflectivity of an infinitely thick layer can be computed if this medium is characterized by a scattering function which is proportional to the term $(1 - \cos\varphi)$; with the equations (5) and (12), it is obtained

$$\pi R\ (\theta_0, \theta, \varphi, 0.545\ \mu) = 30\ \frac{1 - \cos\varphi}{\cos\theta_0 + \cos\theta}\ [\%] \quad (13)$$

This results in a constand reflectivity for $\theta_0 = 0°$, namely $\pi R(\theta_0 = 0°, 0.545\ \mu) = 30\%$.

The results for $\theta_0 = 30°$ have been plotted in the Fig. 63a, those for $\theta_0 = 60°$ in the Fig. 63b. Both the graphs show the predominance of the rediation related with small angles of reflection. At great angles of observation, the reflectivity increases almost gradually with decreasing azimuth α, ranging between 17.5% and 50% for the specific angle of incidence

Θ_o = 3o° and between 1o% and 11o% for Θ_o = 6o°.

The comparison with the relevant measurements (Figures 60 and 61) shows a relatively good agreement of the isolines of reflectivity except for $\Theta > 75°$. This had to be anticipated because the computations have been restricted to primary scattering.

Therefore, the secondary scattering will also be accounted for in the computations of reflection with the help of a formula which has been derived by Schoenberg [7] for secondary scattering. Without going into details it is stated that the consideration of secondary scattering in case of a reduced scattering function 3o (1 - cos φ) requires to add the term

$$\pi R_S = \left(9/(\cos \Theta_o + \cos \Theta)\right)(Aa - Bb + Cc) \qquad (14)$$

to the equation (13).

Schoenberg has tabulated the quantities a, b, and c as functions of the angles of incidence and observation; the quantities A, B, and C can be evaluated as follows

$$\begin{aligned} A &= 2 + \sin \Theta_o \sin \Theta \cos \alpha \\ B &= -2 (\cos \Theta_o + \cos \Theta) \\ C &= -2 (\cos \Theta_o \cos \Theta - \sin \Theta_o \sin \Theta \cos \alpha) \end{aligned} \qquad (14a)$$

The dependence of the reflectivity on the angles of azimuth and zenith distances of the observer under consideration of secondary scattering can be seen from the Fig. 63c for Θ_o = 3o° and 63d for Θ_o = 6o°. A further approximation between computed and measured results can be seen very clearly, especially the measured minimum of reflectivity about ($\Theta = 50°$, $\alpha > 150°$) for the angle of incidence $\Theta_0 = 30°$ is verified by the computation. The remaining deviations in the configuration of the isolines near the horizon might be eliminated if multiple scattering would be taken into account. The curvature of the measured isolines of reflectivity for $\Theta_0 = 60°$ resembles very much that of the computed isolines of reflectivity for $\Theta_0 = 60°$ even in the range of $\alpha < 90°$, however the amount of the measured reflectivity maximum being 74% is far below that of the computed maximum being 120%.

The fine grained soil sample (Fig. 61) yields a much better agreement betwenn measurement and computation.

Summing up: The formula

$$\pi R = 100\ a \frac{1 - \cos \psi}{\cos \Theta_0 + \cos \Theta}\ [\%] \qquad (13a)$$

fits the measured results of the coarse as well as the fine grained soil sample if the computation is based upon the empirical quantities a which depend on the wavelength and are evaluated from the measurements. These factors a are listed in the following table as functions of the wavelengths which have been used in this investigation. The exact theory yields the substitution of these tabulated values of a by the constand value a = 0.25 which is independent of λ.

Table: Dependence of the Factor a (Equation 13a) on the Wavelength, Evaluated From the Measurements.

$\lambda[\mu]$	0.444	0.545	0.647	0.780
a (coarse grained sample)	0.21	0.30	0.34	0.37
a (fine grained sample)	0.23	0.34	0.41	0.43

Even under consideration of secondary scattering, the equation (13a) results for $\Theta_o = 0°$ in curves which obviously deviate from the measured ones. The Fig. 65 refers to $\Theta_o = 0°$ and shows the curves for primary scattering (PS) and secondary scattering (SS) which have been computed according to the formula (13a) as well as the measured values of the coarse and the fine grained sample (λ = o.545 μ).

In case of incidence normal to the surface, the measured reflectivity is expressed best with the equation

$$\pi R(\Theta_o = 0°, \Theta, \lambda) = 100\ a \frac{1 + \cos^2 \varphi}{\cos \Theta_o + \cos \Theta}\ [\%] \qquad (15)$$

The Fig. 66 shows the values of f'/σ' which have been evaluated from the measurements following the equation (11) for various wavelengths; the solid curves represent the function $a(1 + \cos^2 \varphi)$. The quantities $a(\lambda)$ have been assigned the following numerical values: a(o.444 μ) = o.22, a(o.545 μ) = o.31, a(o.647 μ) = o.38, a(o.78o μ) = o.4o.

According to Schoenberg, the equation (15) which expresses the reflectivity for incidence of radiation normal to the surface, is valid for nearly all natural surfaces.

5. Reflection by a Medium Composed of Opaque Spheres.

5.1. Reflection According to Schoenberg.

Schoenberg has computed the reflection by an opaque sphere under the assumption that the surface of the sphere is homogeneous in all points and has no shadowing irregularities. The reflection by a surface element of the sphere follows Lambert's or Seeliger's law resp. The integration taken over the illuminated part of the sphere results in a phase function which according to Schoenberg is especially valid for the solar radiation which is reflected by the moon towards the earth at various phase angles [7, 8]. The substitution of this phase function in (15) leads to either

$$\pi R_L(\theta_o,\theta,\varphi) = \frac{2}{3\pi} \frac{\sin\varphi - \varphi \cos\varphi}{\cos\theta_o + \cos\theta} 100 \quad [\%] \qquad (16)$$

following Lambert's reflection law, or

$$\pi R_S(\theta_o,\theta,\varphi) = k \frac{1 - \sin\gamma/2 \ \mathrm{tg}\gamma/2 \ \ln \mathrm{ctg}\gamma/4}{\cos\theta_o + \cos\theta} [\%] \quad (17)$$

where $\gamma = \pi - \varphi$ following Seeliger's reflection law.

The results of the computations for the main plane ($\alpha = 0°$, $\alpha = 180°$) are presented in the Fig. 67 for the angles of incidence $\theta_o = 0°$, $30°$, and $60°$. The constant k in the equation (17) has been determined with the relationship $R_L(\theta_o = 0°, \theta = 0°) = R_S(\theta_o = 0°, \theta = 0°)$. The solid lines represent the curves of the formula (16), the broken lines those of the deviating curves of the formula (17).

5.2. Comparison With the Measurements.

The Fig. 67 also shows the measured values of the coarse soil sample. The agreement between the measured and the computed values is better for those reflectivity values which have been evaluated with the function ($1 - \cos\varphi$) than for those evaluated according to the equations (16) and (17). However, a final statement can be made no sooner than after taking into account at least the secondary scattering in the model computation for a medium composed of opaque spheres. The Fig. 64 furthermore shows the great deviation between the scattering functions ($1 - \cos\varphi$) and ($\sin\varphi - \varphi\cos\varphi$); this had to be anticipated because the individual particles of the soil samples partly showed considerable deviations from the spherical form. However, both these functions give a good qualitative description of the backward scattering on an opaque particle.

5.3. Hapke's Reflection Formula.

For completeness, the equations (16) and (17) require a correction according to Hapke [9]. This correction effects another increase of reflectivity for scattering angles greater than 90°.

6. Concluding Remarks on the Physical Explanation of the Measurements.

The aforementioned theoretical considerations enable one to give a physical explanation for the angular dependence of the radiation which is reflected by calcareous soil samples of varying granulation.

Each individual particle of a measuring sample consists of several smaller particles. The reflection by a surface element of this individual particle is therefore based upon the amended form of Seeliger's reflection law for a medium composed of large particles (Section 3.4.). The great increase of reflectivity with the wavelength can be explained with the diffraction term which is independent of the transparency of the individual particles; thus, it might be expected that the reflectivity of other soil samples shows a similar trend according to the wavelength. This assumption has been verified through the measurements made by other authors, e. g. [10, 11, 12, 13].

The scattering of an individual particle follows a phase function which is proportional to the average surface brightness of the illuminated part of the individual particle. Following the statement made in the previous paragraph the average surface brightness depends on the wavelength. Schoenberg interprets the phase function as a shadowing effect. The dependence of the reflectivity on the angles of incidence and observation is then obtained by applying once more Seeliger's law to the reflection of an infinitely thick medium, under the assumption that scattering takes place on opaque particles (equations 16 or 17 resp.). Since the light undergoes diffraction also by the individual spheres, an increase in reflectivity must be expected when the granulation of the sample grows finer, according to Section 3.4.

The shadowing effect can be demonstrated through photographs of the soil samples at various angles of incidence, while the camera is pointing vertically downwards. The 1.photo distinctly shows a great increase in the shadowed part of the coarse soil sample with increasing angle of incidence θ_0, i. e. with decreasing scattering angle. The sections on the lower margin of the individual graphs have a distance of 1 mm. The 2.photo proves that even the fine grained soil sample has a great number of particles large enough for producing a shadowing effect. Here, the distance of the sections is o.5 mm.

For limestone has been calculated a refractive index 1.66.
The density was measured to 2.492 g cm^{-3} ± o.oo4.
Correction: Final Report No 5 read for the wavelengths page 45 .444, .545, .647, .78μ, page 46
$R = 1/o.937\pi\ (I_{max} + I_{min})/B$.

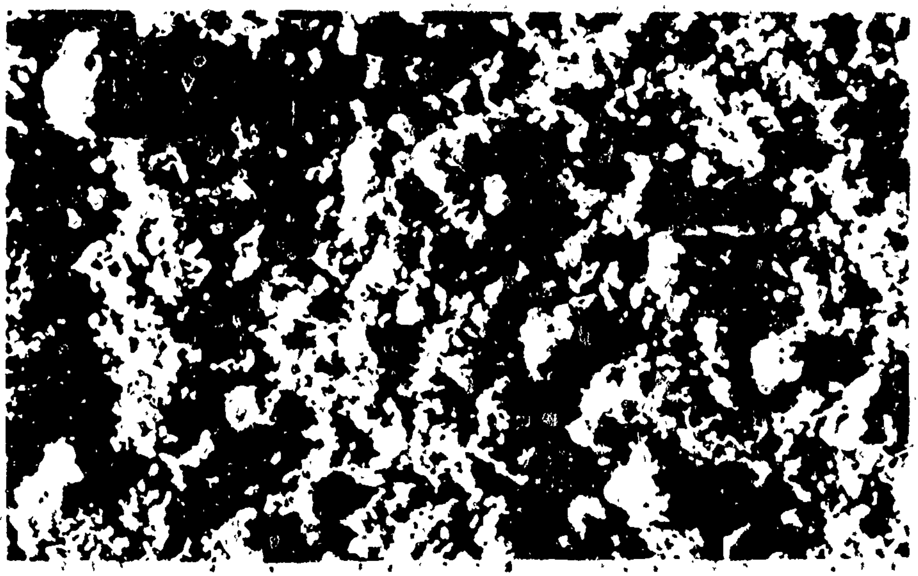

$\theta_0 = 70°$

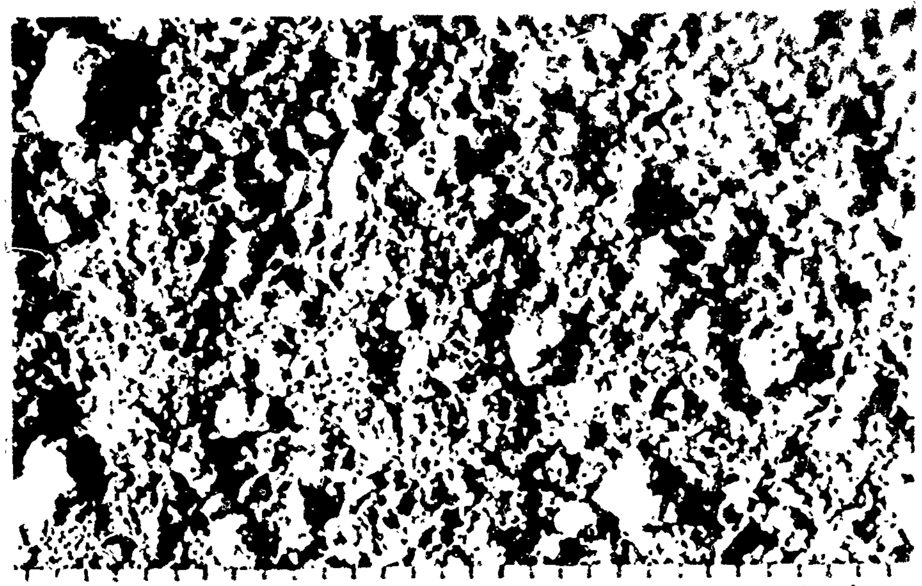

$\theta_0 = 45°$

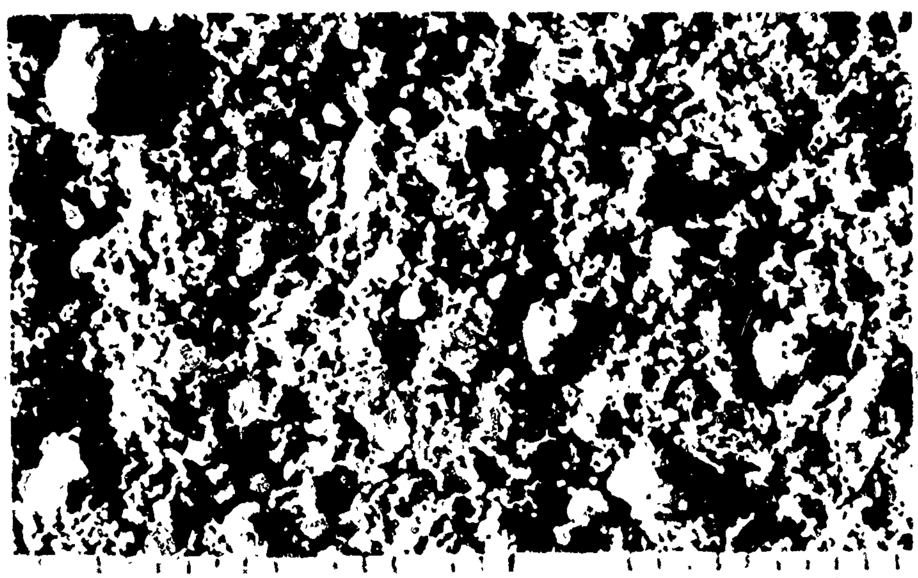

$\theta_0 = 60°$

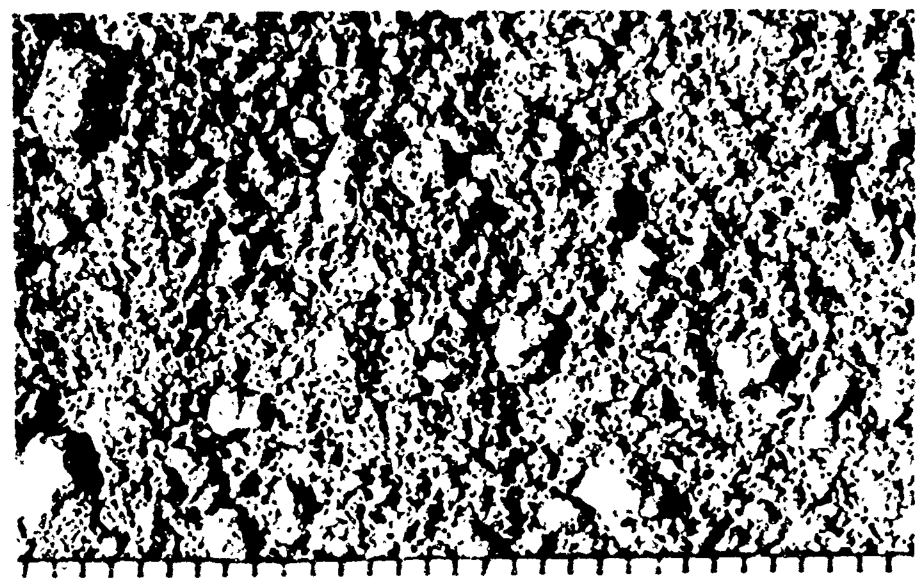

$\theta_0 = 35°$

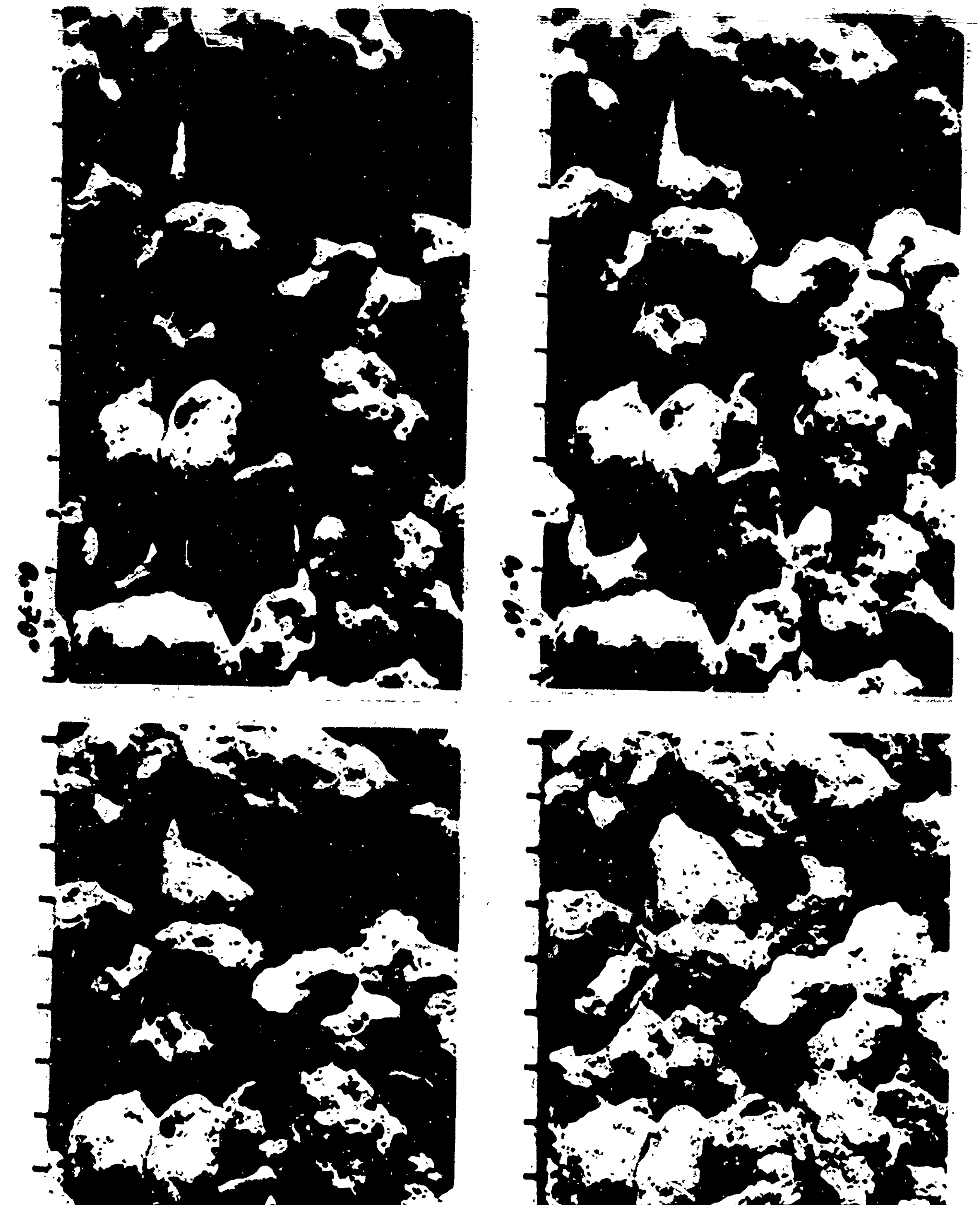

C. The Influence of the Shape of the Aerosol Particles on Their Collection in a Jet Impactor.

The accuracy of the interpretation and the computation of the spectral extinction of the atmospheric radiation and the related phenomena of the sky radiation depends inter alia on whether the full particulars are known about the size distribution and the complex index of refraction of the aerosol particles. Jet impactors are used for both measuring the aerosol size distribution and ~~air~~ sampling for measuring the complex index of refraction of the aerosol particles. So far, the interpretation of the measurements has been based upon the validity of the impactor theory e. g. given by RANZ and WONG [14]. This theory is essentially based upon the validity of Stokes's law which deals with the frictional force arising from the viscosoty of a medium upon spheres and its extension to very small particles by KNUDSEN and WEBER [15]. However, quite a number of authors have shown that there is no unrestricted validity of this law and the inertia parameter

$$\psi_s = \frac{2}{9}\,\frac{u_j r^2 \varrho}{\eta_j D_j}\left(1+\frac{l_j}{r}\left[A+Q\,\exp\left(-B\,\frac{r}{l_j}\right)\right]\right) \qquad (1)$$

which has been derived from it for the movement of spheres in jet impactors; this is true with spheres as well as nonspherical particles. The symbols of the equation (1) are: $A = 1.23$, $Q = 0.41$, $B = 0.88$, ϱ is the density of the aerosol particles, u_j is the speed of the aerosol in the exit plane of the jet, r is the radius of the spheres, η_j is the dynamic viscosity of the air in the exit plane of the jet, D_j is the width of the jet, l_j is the mean free path of the air molecules in the exit plane of the jet.

The first restriction has the consequence that any calibration of jet impactors holds only for the specific operational conditions which it has been based upon. This has been proved by a comparison between the impactor calibrations by STERN et al. at low air pressure and those by RANZ and WONG at an air pressure of about 1 atm., which will not be discussed in this paper. Now a detailed report on the second restriction will be given.

A mathematical approach will be given for the influence of the shape of the aerosol particles on their collection in a jet impactor. At first, a quantity has to be discussed which defines the departure from the spherical shape of the aerosol particles in a suitable way. Such a quantity is the dynamic shape factor $\varkappa$. For specific REYNOLDS numbers characterizing the flow around nonspherical particles $\varkappa$ is the quotient of the mean air resistance to this particle to the air resistance to that sphere which has the same volume as this particle. The radius of this equivalent sphere is called equivalent radius r. The REYNOLDS number characterizing the flow around a particle is defined as

$$Re = \frac{2r\rho_j u_{rel}}{\eta_j} \qquad (2)$$

where r is the equivalent radius of the particle, in case of spheres r is equal to the radius of the sphere, ρ_j is the air density in the exit plane of the jet, u_{rel} is the mean relative speed between the air and aerosol particles in between the exit plane of the jet and the collecting plate in the jet impactor.

The measurements of dynamic shape factors have shown that $\varkappa$ is always greater than 1 as soon as Re becomes greater than o.o5 [16,17,18]. For Re < o.o5 ellipsoids can possibly have dynamic shape factors smaller than 1, however, this is true only with certain directions of flow against the ellipsoids. The dynamic shape factor increases with increasing REYNOLDS number, at the beginning only slightly, but later in the phase of turbulent flow around the particle it increases greatly. The flow around the particle becomes turbulent when $Re > Re_{crit}$, i. e. when the critical REYNOLDS number is exceeded. The latter amounts to 154 for cubes and to 68 for tetrahedrons. The more the shapes of the particles deviate from the spherical shape, the smaller the critical REYNOLDS numbers are.

A more general version of the inertia parameter Ψ_s is obtained if the dynamic shape factor is introduced into the equation (1). This transformation is based upon the definition of the inertia parameter as the quotient of the force which stops the particles on the way $D_j/2$ (this force is assumed to be constant) to the air resistance of the particle. Hence, in case of nonspherical particles the inertia parameter is expressed as

$$\Psi = \frac{2}{9} \frac{\varrho u_j r^2}{\eta_j D_j \varkappa} \left(1 + \frac{l_j}{r}\left[A + Q \exp\left(-B \frac{r}{l_j}\right)\right]\right) \qquad (3)$$

For spheres $\varkappa = 1$, hence $\Psi = \Psi_s$. Thus the equation (1) is a special form of the equation (3).

The calibrations by RANZ and WONG [14] for rectangular jets are used for the computations on the influence of the dynamic shape factor on the collection of nonspherical particles in jet impactors. These calibrations have been conducted in atmospheric pressure which corresponds to that of the lowest troposphere. The speeds in the jets have been $10.5 \text{ m sec}^{-1} \leq u_j \leq 180 \text{ m sec}^{-1}$. The distances between the exit plane of the jet and the collecting plate have been 1 to 3 times as great as the widths of the jets. The latter have been $0.020 \text{ cm} \leq D_j \leq 0.071 \text{ cm}$, and the radii of the test spheres have been $0.17\ \mu \leq r \leq 0.69\ \mu$. RANZ and WONG have evaluated their calibrations for determining the collection efficiency η, i. e. the fraction of all particles initially moving on a collision course with a given impactor which actually do collide with and remain adhered to that impactor, as a function of the inertia parameter Ψ_s. If the operational conditions are given, this function $\eta = \eta(\Psi_s)$ is determinate. It can be applied also to jet impactors with rectangular jets which are geometrically similar to the calibrated impactors and are operated under the same conditions as during the calibrations. The calibrations by RANZ and WONG can be applied also to nonspherical particles because the special inertia parameter Ψ_s for spheres is a special case of the general inertia parameter Ψ for nonspherical particles. Thus, from the theoretical standpoint it does not matter which kind of particles is used for calibrating the impactors, hence $\eta(\Psi_s) = \eta(\Psi)$.

The computations on the influence of the dynamic shape factor have been carried out for the operational conditions given in Table 1.

Table 1. Operational Conditions Inside the Jet Impactor

T_a = 283°K	D_j = 0.03 cm	$\rho_j = 1.27 \cdot 10^{-3}$ g cm^{-3}
p_a = 760 Torr	$u_j = 10^4$ cm sec^{-1}	$\eta_j = 1.74 \cdot 10^{-4}$ g cm^{-1} sec^{-1}
	$l_j = 6.1 \cdot 10^{-6}$ cm	

(T_a = air temperature in front of the jet,
p_a = air pressure in front of the jet).

The mean density of the aerosol particles has been assumed to be $\rho = 2$ g cm^{-3} [19]. The readings from the calibration curve $\eta = \eta\,(\psi)$ have been based upon these operational conditions. Thus, the relationship between the collection efficiency η and the equivalent radius r (for $\varkappa = 1$, r is equal to the radius of the sphere) of the particles has been computed for the dynamic shape factors $\varkappa$ = 1, 1.05, 1.1, 1.2, 1.4, 1.6, 1.8, and 2. These functions $\eta = \eta\,(r,\varkappa)$ have been plotted in the Fig. 68a. This graph shows that the collection efficiency of the little nonspherical particles in the impactor is the lesser the more they deviate from the spherical shape, i. e. the greater their dynamic shape factors.

The functions $\eta = \eta\,(r,\varkappa)$ enable one to compute the number and the volume of the particles collected in the jet impactor, for given aerosol particle size distributions. These computations have been based upon JUNGE's aerosol particle size distribution

$$\frac{dN(r,\nu^*)}{d \log r} = n(r_o)\left(\frac{r}{r_o}\right)^{-\nu^*} \qquad (4)$$

where ν^* is the JUNGE exponent, $N(r,\nu^*)$ is the number of aerosol particles smaller than r, $n(r_o) = (dN/d\log r)_{r=r_o}$, r_o is the reference radius.

The JUNGE exponents have been $\nu^* = 2, 2.5, 3, 3.5, 4, 4.5$. The smallest equivalent radius of the size distribution has been $\underline{r} = 0.05\mu$. The greatest equivalent radius of the size distribution has been $\overline{r} = 1\mu$. The number Z and the volume V of the aerosol particles collected in the jet impactor have been obtained between the limits $\underline{r} = 0.05\mu$ and $\overline{r} = 1\mu$ by numerical integration of the functions

$$dZ(r,\nu^*,\varkappa) = \eta(r,\varkappa)\cdot dN(r,\nu^*) \qquad (5)$$

and

$$dV(r,\nu^*,\varkappa) = \eta(r,\varkappa)\,\frac{4}{3}\,\pi r^3 dN(r,\nu^*) \qquad (6)$$

The integrals of these functions are

$$Z(\underline{r},\overline{r},\nu^*,\varkappa) = \frac{n(r_o)\cdot r_o^{\nu^*}}{\ln 10}\int_{\underline{r}}^{\overline{r}} \eta(r,\varkappa)\, r^{-\nu^*-1}\, dr \qquad (7)$$

and

$$V(\underline{r},\overline{r},\nu^*,\varkappa) = \frac{4\pi n(r_o)\cdot r_o^{\nu^*}}{3\ln 10}\int_{\underline{r}}^{\overline{r}} \eta(r,\varkappa)\, r^{-\nu^*+2}\, dr \qquad (8)$$

The results of the integration are presented in the Figures 68b and 68c in which the relative quantities

$$Z_{rel} = \frac{Z(\underline{r},\overline{r},\nu^*,\varkappa)}{Z(\underline{r},\overline{r},\nu^*,\varkappa=1)} \qquad (9)$$

and

$$V_{rel} = \frac{V(\underline{r},\bar{r},\nu^*,\varkappa)}{V(\underline{r},\bar{r},\nu^*,\varkappa=1)} \tag{10}$$

have been plotted as functions of the dynamic shape factor $\varkappa$, the parameters being the JUNGE exponents $\nu^* = 2$, 2.5, 3, 3.5, 4 and 4.5. Z_{rel} is the quotient of the number of the nonspherical particles collected in the jet impactor to the number of the spherical particles with the same equivalent radii collected under the same operational conditions. V_{rel} is the quotient of the volume of the nonspherical particles collected in the jet impactor to the volume of spherical particles with the same equivalent radii collected under the same operational conditions. The size distributions in equivalent radii are identical for both the nonspherical particles and their equivalent spheres. The graphs show that as well Z_{rel} as V_{rel} are smaller than 1 for all values of ν^* between 2 and 4.5 and for all values of $\varkappa$ between 1 and 2. This means in accordance with Fig.68c, that less nonspherical little particles are collected than spheres of their equivalent radii.

The computational results will be specified by measurements of dynamic shape factors. The values of the dynamic shape factors depend on the mean REYNOLDS numbers for flow around particles in the space between the outlet of the jet and the collecting plate. Thus, it is indispensible to make a scientific guess on these REYNOLDS numbers. Detailed investigations into this problem have shown that for computing Re with the help of the equation (2), the first approximation $u_{rel} = u_j$ is admissible. Then, the mean REYNOLDS numbers for flow around particles are about 3 for those operational conditions which the computations have been based upon. PETTYJOHN and CHRISTIANSEN [16] have found in their measurements that $\varkappa(\mathrm{Re} = 3) \approx 1.09$ for cubes and $\varkappa(\mathrm{Re} = 3) \approx 1.25$ for tetrahedrons. McNOWN and MALAIKA [17] have found in their measurements that $\varkappa(\mathrm{Re} = 3) \approx 1.4$ for rod-shaped rotation ellipsoids, cylinders, prisms, or spindles if the ratio of their axes is 1:4 and that $\varkappa(Re = 3) \approx 1.6$ for disk-shaped rotation ellipsoids, cylinders, prisms, or spindles if the ratio of their axes is 4:1. KUNKEL [18] could show in his measurements that dynamic shape factors $\varkappa(Re = 3) \approx 1.6$ are to be expected in case of agglomerations of 3 spheres of equal volume. If these values of $\varkappa$ amounting to 1.o9, 1.25, 1.4, and 1.6 are used for the computations, the relevant values of Z_{rel} for $v^* = 3$ are o.84, o.65, o.52, and o.42 and the relevant values of V_{rel} for $v^* = 3$ are o.94, o.89, o.84, and o.78. Thus, only slight deviations from the spherical shape complicate the interpretation of measurements if the aerosol particles are collected with a jet impactor. Up to now nothing is known about the dynamic shape factors of the aerosol particles.

A detailed knowledge of the shapes of the atmospheric aerosol particles and the relevant dynamic shape factors as well as the particle densities is the prerequisite for measuring the size distribution of their equivalent radii with jet impactors or other measuring devices based upon the principle of inertia. This will be demonstrated with an example: It is a common practice to compute the so-called STOKES'S radius r_s of the aerosol particles which is related with a specific value of collection efficiency η, e. g. o.5, from the operational conditions of the jet impactor and the well known function $\eta = \eta(\Psi)$. r_s is the radius of a sphere which has a specific density ϱ_0. Mostly, it is set: $\varrho_0 = 1$ g cm^{-3}. The equation (3) for the inertia parameter for irregularly shaped particles can be used for evaluating r_s as follows:

$$r_s^2\left(1+\frac{l_i}{r_s}\left[A+Q\exp\left(-B\frac{r_s}{l_j}\right)\right]\right)= \frac{\varrho}{\varrho_0\varkappa}\, r^2\left(1+\frac{l_i}{r_s}\left[A+Q\exp\left(-B\frac{r_s}{l_j}\right)\right]\right) \quad (11)$$

It can be seen from the equation (11) that the STOKES'S radius depends not only on the equivalent radius r but also on the ratio $\varrho/(\varrho_0 \varkappa)$ which is not known for the atmospheric aerosol particles. Thus, the STOKES'S radius cannot be taken for an exact measure of the aerosol particle size. If the ratio $\varrho/(\varrho_0 \varkappa)$ is not constant for all particles, it is possible that there are gaps in the size distribution of the STOKES'S radii without such gaps in the size distribution of the equivalent radii.

FENN [20] has measured gaps in the size distribution of STOKES'S radii of atmospheric aerosol particles with an aerosol centrifuge by GOETZ. FENN has found these gaps also by meas of optical measurements. The physical explanation might be the fact that well the ratio $\varrho/(\varrho_0 \varkappa)$ as the refractive index of the aerosol particles in the relevant intervals of the equivalent radii have differed from those in the neighboring intervals.

Summing up: The shape and the density of the aerosol particles play a decisive role in the collection process in jet impactors. In addition, there is no agreement in the calibrations of impactors which various authors have made under different atmospheric conditions. Therefore, it is necessary to improve the theory of the jet impactors. A first approach upon which will not reported here is considered being successful since the theory is in agreement with the measurements. Furthermore, this new approach could be used for explaning e. g. the quantitative discrepancies between the impactor calibrations by RANZ and WONG [14] and those by STERN et al. [21]. At present, it is being tried to improve this first approach.

<u>List of Symbols</u>

D_j	Width of Jet
l_j	Mean Free Path of the Air Molecules in the Exit Plane of the Jet
$N(r,v^*)$	Number of the Aerosol Particles Whose Equivalent Radii are Smaller Than r
$n(r_o) = (dN(r,v^*)/d\log r)_{r=r_o}$	
p_a	Air Pressure in Front of the Jet
r	Equivalent Radius
r_o	Reference Radius
r_s	STOKES'S Radius of an Aerosol Particle
Re	REYNOLDS Number for the Flow Around an Aerosol Particle
Re_{crit}	Critical REYNOLDS Number for the Flow Around an Aerosol Particle
T_a	Air Temperature in Front of the Jet
u_j	Speed of the Aerosol in the Exit Plane of the Jet
u_{rel}	Mean Relative Speed Between Aerosol Particles and Air in Between the Exit Plane of the Jet and the Collecting Plate in the Jet Impactor
V	Volume of the Aerosol Particles Collected in the Jet Impactor
Z	Number of the Aerosol Particles Collected in the Jet Impactor
η	Collection Efficiency of Aerosol Particles in a Jet Impactor
η_j	Dynamic Viscosity of the Air in the Exit Plane of the Jet
$\varkappa$	Dynamic Shape Factor of Aerosol Particles
v^*	JUNGE Exponent
ρ	Density of Aerosol Particles

ρ_j	Air Density in the Exit Plane of the Jet
ρ_o	Arbitrary Density Value
ψ	Inertia Parameter for Any Given Shapes of Particles in the Jet Impactor
ψ_S	Inertia Parameter for Spheres in the Jet Impactor

D. Contribution to the Polarization of the Sky Radiation.

1. Diagram for Determining the Variation of the Degree of Polarization as a Function of Various Parameters.

The diagram shows the variation of the maximum degree of polarization of the sky light as a function of each of the following parameters: Turbidity T, wavelength λ, exponent of the aerosol particle size distribution ν*, zenith distance of the sun Z, and albedo A. The conclusions drawn are of qualitative nature.

The ordinate represents relative units. The 24 columns do not comprise all the possible combinations of these five parameters, they represent an arbitrary selection of these combinations. For example: In case of increasing turbidity in the column 1 while ν* has a small value and the albedo A=0, the degree of polarization decreases more slightly at short wavelengths (Column 1) than at longer ones (Column 2). This process is independent of the zenith distance of the sun. Therefore, the relevant squares in the columns 1 and 2 are black. If the same increase in turbidity is combined with a great value of ν*, the wavelength dependence of the maximum degree of polarization makes itself hardly felt any more (Columns 3 and 4).

This diagram enables one to compare the rates of the degree of polarization in those columns which comprise a variation of the same parameter.

The bottom line of the columns 13 through 16 and 17 through 22 does not represent the maximum degree of polarization, but the degree of polarization at scattering angles

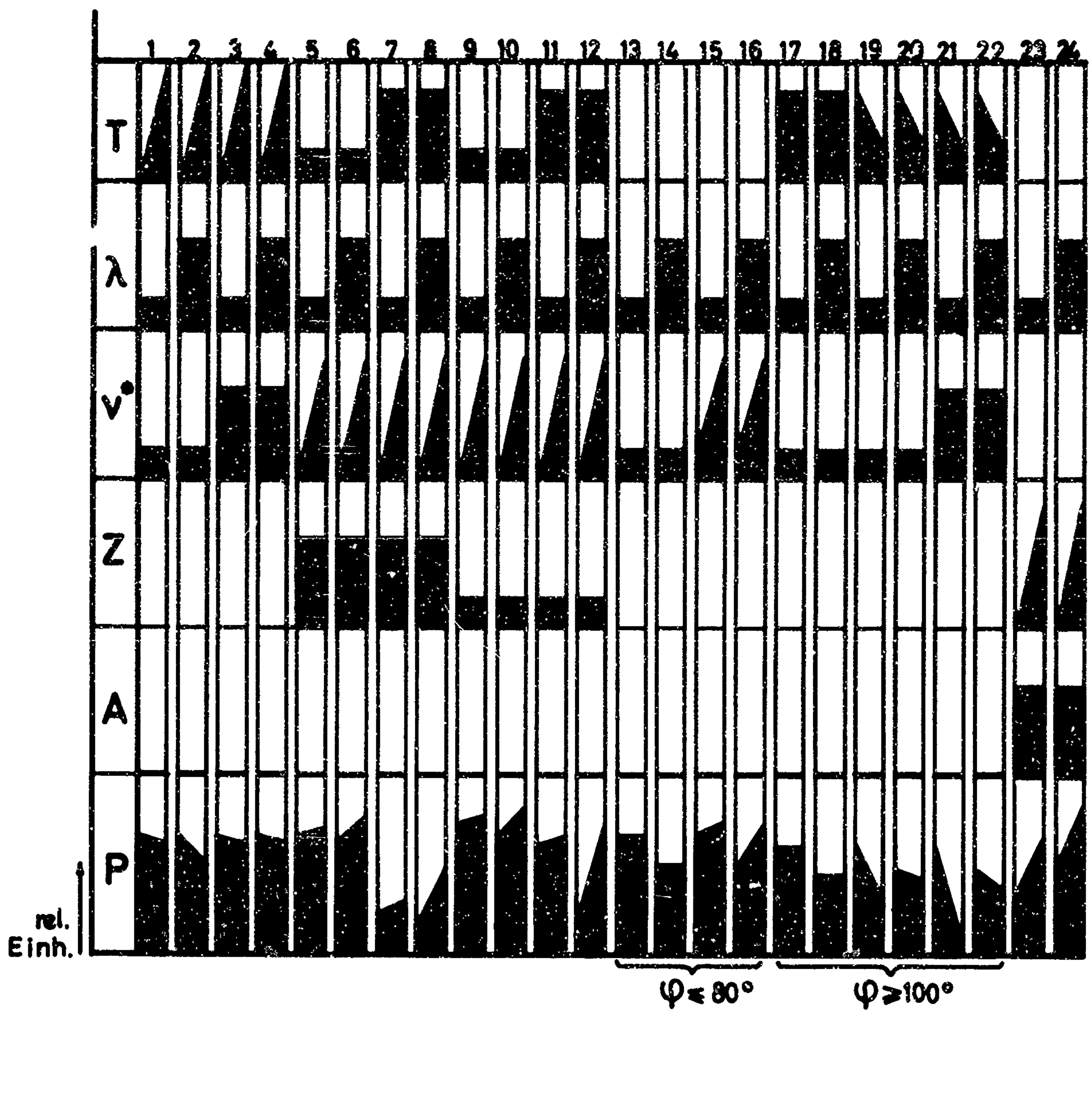
1 2 3 4 5 6 7 8 9 10 11 12 13 14 15 16 17 18 19 20 21 22 23 24
T
λ
v°
Z
A
P
rel. Einh.
φ ≤ 80°
φ ≥ 100°

$\psi = 80°$ and $\varphi = 100°$ resp.

Some cases enable one to make a qualitative statement not only on the variation of the degree of polarization, but also on its amount. The columns 23 and 24 give an example: They show an increase in the degree of polarization with increasing zenith distance of the sun independent of the turbidity at a great albedo; the rate of increase is almost the same at short and long waves, but the degree of polarization is always greater at long waves than at short ones, at the same zenith distance of the sun.

This scheme has been based upon de Bary's computations in order to interpret polarization measurements of the type which is represented in the following graphs and to relate them with the aerosol particle size distribution.

2. <u>Measurements of the Spectral Distribution of the Polarization of the Sky Radiation on 22 September 1966 at Mainz, Germany.</u>*)

The figures 69-71 show the spectral distribution of the percentage degree of polarization of the sky radiation for the wavelengths $\lambda_1 = 0.449\mu$, $\lambda_2 = 0.624\mu$ and $\lambda_3 = 0.844\mu$ as a function of the zenith distance of the point under observation in the sky for 5 verticals from the zenith to the horizon. The azimuth angle of the observation point from the sun's vertical is used as parameter. The first vertical is identical with the sun's vertical, the fifth with the sun's countervertical; the angular distance between two neighbored verticals is 45°. The measurements have been plotted for 6 solar elevations.

*) The fully automatic measuring device has been described in the Final Tech Rep Contract DA-91-591-EUC-3458, Apr 1966.

This method of presentation is more conspicuous than isopleths because it is more responsive to changes in the slope of the curves as e. g. due to erratic or multiple maxima. It can be assumed that the circle of maximum polarization in the sky almost coincides with the circle of $\varphi = 90°$. This prerequisite implies a theoretical curve pattern as follows:

The maximum of the 90°-curve is always found at the zenith distance $z = 90°$, i. e. at the intersection with the horizon, independent of the zenith distance Z. From the 90°-curve towards the countervertical, the maximum polarization shifts to gradually decreasing values of z; in the countervertical, i. e. in the 180°-curve, the maximum polarization reaches its greatest height at the zenith distance $z = 90° - H_o$ (H_o denotes the elevation angle of the sun). In between the 90°-curve and the sun's vertical, i. e. the 0°-curve, this maximum point is located underneath the horizin or beyond the zenith resp. This implies that both the 45°-curve and the 0°-curve show an increase at both their ends and a minimum at $z = Z$. The minimum value of the 45°-curve amounts to half of the maximum value, whereas the minimum value of the 0°-curve is zero.

The knowledge of the height of the polarization maximum along a vertical does not enable one to draw any conclusions on the actual value of the polarization maximum. In the case of the two separate maxima as for instance due to haze layers in the turbid atmosphere, this maximum can amount to greater values in the 135°-vertical than in the sun's countervertical.

Theoretically, all the 5 lines should intersect the ordinate in the same point at $z = 0$. This cannot be fully realized due to the time lag between two zenith measurements and due to a small polarization effect of the multiplier. A measuring set for each of the verticals comprised 5 observation points (including the zenith) at 3 wavelengths, so that the time interval between two zenith measurements was about two minutes. This time lag has an effect on the zenith measurements only at a low sun. The rotation of the multiplier around its optical axis as it is the routine between two zenith measurements, can cause a polarization effect of the multiplier window of 3%. This effect can be eliminated only if besides the degree of polarization also the position of the polarization plane in the sky is determined.

The examples of the measurements presented in the graphs can be evaluated as follows: At the beginning of the measurements at the solar elevation H_0 = 16°30' a.m., the maximum polarization found in the infrared is distinctly lower than in red and in blue light. During the course of the day the maxima of the different wavelengths gradually become almost equal in amount; from H_0 = 26° a.m. on, the maxima at λ = 0.449μ and at λ = 0.624μ are nearly the same and in the afternoon, a wavelength dependence of the maximum polarization can hardly be seen any more. Furthermore, all the maxima of the afternoon are higher in amount than in the morning.

Moreover, two separate maxima occur. This can be seen from the greater values in the 135°-curves and the 90°-curves compared with the 180°-curves, i. e. the counterverticals, which according to the theory, should have the only maximum. Furthermore, the ratio of the maximum values of the 135°-curves to those of the 180°-curves varies: This variation manifests a displacement of the maxima; with increasing solar elevation the maxima are shifted towards the countervertical, in the afternoon, however, back towards the horizon.

A striking fact is the great bulge of the 90°-curve at the wavelength $\lambda = 0.844\ \mu$ at the solar elevation $H_0 = 35°$ a.m. This implies a shifting of the maximum towards the horizon in the infrared, whereas in the red and blue light this shifting is not observed. The physical explanation is a distinct momentary atmospheric pollution due to smoke plumes which contain mainly large particles and thus have an effect only in the long wave portion of the spectrum.

The curves have been plotted only down to a zenith distance $z = 72°$ because this has been the lowest point under observation.

These figures are only a few selected examples of quite a number of measurements in order to prove the feasibility of obtaining information on the amount of the maximum polarization, the wavelength dependence, the location of the maxima and the influence of specific types of aerosol particles on the degree of polarization of the sky light.

E.

A Portable Scattering Function Meter

I. The Device and Operation.

A number of devices, called nepholometers, intended to measure the angular variation of scattered flux from a volume of air or other scattering medium have been developed in the past twentyfive years, all more or less based on the design of Waldram [22]. The mathematical expression for this property, called the scattering function, is found in the equation in polar coordinates:

$$\tau_s(\alpha,m) = \frac{I}{E_o V_s} = 2\pi \int_0^{\pi} f\,(\alpha,m,\varphi)\,\sin\varphi d\varphi \qquad (1)$$

where $\tau_s(\alpha,m)$ is the volume scattering coefficient, physically the flux I scattered out of a unit volume V_s per unit irradiance E_o of the volume; $f\,(\alpha,m,\varphi)$ is the scattered function, φ is the angle between the forward direction of the incident beam and the scattered light, called the scattering angle, and α and m are the scattering parameter $\frac{2\pi r}{\lambda}$ and the index of refraction, respectively.

The instrument which will be described Fig. 72 was based loosely on Duntley's [23] device, but differs from it in several important and essential ways. First, portability and consequently the potential for a wider employment were achieved in the new instrument by allowing the photometer and light trap combination to rotate about the scattering volume, rather than move in a circular path while mounted rigidly on an aircraft. Secondly, a chopper has been added to increase the signal to noise ratio and to eliminate the effect of the sky-light background. The open space found in Duntley's device is now enclosed by a rotation tube having two rectangular apertures of equal size oppositely located along the sides. Light from the sun or a collimated source, entering each of the apertures in turn as they pass by the sourcelit side of the instrument, irradiates the scattering volume at twice the chopper frequency. Finally, the blackened inner wall of the instrument, half cut away where the chopper is located, provides a means of masking the scattered volume from light sources below the scattering plane. This mask eliminates the need for an albedo grid such as Duntley used and, at the same time, complements the function of the chopper as shown below. The resulting irradiation of the scattering volume during one period of rotation of the chopper about its centerline is as shown in the following table:

Source of Irradiation	Portion of the Period			
	T_1	T_2	T_3	T_4
a. through aperture 1:	Sky	Sky + Sun	Mask	Mask
b. through aperture 2:	Mask	Mask	Sky	Sky + Sun
c. total irradiation through both apertures:	Sky + Mask	Sky, Sun + Mask	Sky + Mask	Sky, Sun + Mask

It is only necessary, then, to use an amplifier tuned to double the chopper frequency of rotation in order to isolate the photometer signal which is proportional to the effect of the irradiation of the scattering volume by source light alone. As the entire instrument rotates about the axis normal to the scattering plane, the angular variation of this signal is measured, from which one may obtain the scattering function directly.

The following calculations were made to determine if an adequate signal to noise ratio could theoretically be developed by the instrument using interference filters. If the equation (1) is written in terms of solid angles and differentiated, one obtain:

$$f(\alpha,m,\varphi) = \frac{d\tau s(\alpha,m)}{d\omega} = \frac{I(\alpha,m,\varphi)}{E_o V_s} \qquad (2)$$

The flux received at the lens having area A at a distance from the scattering volume is given by:

$$P = \frac{IA}{r^2} = \frac{E_o\ A\ f(\alpha,m,\varphi)\ V_s}{r^2} \qquad (3)$$

The flux density irradiating the scattering volume, E_o, was calculated from extraatmospheric irradiation per micron for .555 μ as given by Johnson [24] and corrected for attenuation through an atmosphere having a turbidity factor of 6 along a slant path of 3o° elevation. The resulting irradiation of the scattering volume was estimated at 1.76×10^{-2} watts/cm^2/μ. The lens used in the instrument has an area of 37 cm^2, approximately. An expression for $(dk/d\omega)_R$, the Rayleigh scattering function, derived from Johnson [25], was used as a starting point. The expression obtained was:

$$\frac{dk}{d\omega_R} = f(\alpha,m,\varphi) = \frac{2\pi^2\ (m-1)^2{}_{gas}\ (1 + \cos^2\varphi)}{\lambda^4 n} \qquad (4)$$

where m is the index of refraction of air, $(m-1)_{gas}$ refers to a cubic centimeter of gas, given as 293×10^{-6} by Johnson and n is the molecular number density at sea level. The scattering volume was taken as 5oo cc. This gave the flux scattered at 9o° falling on the lens as roughly 2.3×10^{-9} watts/μ or 2.3×10^{-11} watts for a 1o mμ interference filter bandwidth. Assuming that Mie scattering exceeded this value by a factor of 1o, that the lumped transmissions of the filters and the lens amounted to 3o% and all energy reached the photocathode, and further calculating an noise effective power of 8×10^{-3} watts for the photomultiplier with a 1 cycle noise bandwidth using the resonant amplifier, asignal to noise ratio of 8 was arrived at, showing that the critical elements of the design were adequate for obtaining useful information for the arbitrary conditions chosen.

III. Mechanical and Optical Design Features.

The instrument may be regarded as a narrow field photometer with a chopper and light trap located coaxially in front of the optics as a kind of foreoptical element. The photometer optic consists of a 7.5 cm diameter lens with a focal length of 15 cm located toward the rear of the instrument. A polarizing filter, manufactured by Käsemann, is set behind the lens in a rotation mount, so that the scattered intensity normal and parallel to the scattering plane can be measured. At present, Schott absorption filters are being used to obtain the spectral dependence of the scattering function, and, during measurements, these are inserted sequentially behind the lens. A Maurer SMV photo-multiplier with a side looking photocathode having a 7 mm x 7 mm surface is located 1 cm behind the focal point of the lens. A field stop having a 7 mm diameter placed at the focal point restricts the field of view of the lens so that no direct rays through the apertures nor rays reflected from walls or stops in the instrument tube fall on the photo-cathode. Forward of the lens, a series of movable stops sprayed with 3M Black Velvet Optical Lacquer have been placed within the tube, each one masking the side of the tube in front of it from the lens, while those on either side of the chopper apertures screen the lens and light trap from direct rays of the sun and at the same time limit the maximum forward and back scattering angles for which the scattering volume remains constant. On the outer wall of the tube on either side of the chopper apertures, additional stops have been placed to screen the lens and light trap from sky radiation.

The instrument tube is made of brass and consists of three sections, the photometer, the chopper and the light trap, easily separated for transport and repair or adjustment. The chopper is driven by a 3ooo r.p.m. synchronous motor through a ring gear operating at 8:1 reduction, mounted on its outer edge. The motor is mounted partially within the instrument tube rather than flush so as to reduce the diameter of the ring gear mounted on the chopper. This is necessary to prevent the ring gear from forming an outside stop for source rays before the maximum planned backscattering angle is reached. Care must be taken that the angle formed by the ring gear and the rear edge of an aperture is smaller than that formed by the edge and any other stop intended to limit sky or source light. The same is true for a reinforcing ring located on the other end of the chopper.

The instrument is mounted on a tapered steel shaft seated in brass and driven through a worm gear arrangement by a synchronous motor at o.2 r.p.m. A spirally wound resistor geared to the shaft, in combination with a 1.5 volt cell and voltage divider, is used to obtain a voltage which is proportional to the amount of rotation. A three-pole, double-throw switch attached to the shaft seat reverses the direction of rotation of the drive motor automatically at the end of each 18o° traverse or less, if desired. This mount, in turn, can be pivoted about horizontal and vertical axes to change the scattering plane to correspond with the elevation and azimuth of the sun, respectively. The entire system is mounted on a wooden tripod and weighs approximately 2o kg.

To allow use of the higher operating voltages, a cooling housing for the photomultiplier has been developed. Crushed dry ice is poured into a plastic cylinder enclosing the tube, which is in contact with the cylinder wall where a hole the size of the photomultiplier window, surrounded by a sponge rubber gasket, allows the scattered light to pass, but no gases or vapors. Dry nitrogen is introduced at low pressure to the space between the photomultiplier window and the filter, purging it of water vapor and preventing ice from forming on the window. The gasket mentioned reduces the loss of nitrogen and prevents it from heating the dry ice. Nitrogen is also introduced at low pressure to the tube voltage source connector to avoid condensation which might cause a short circuit.

Although normalized scattering functions are useful, it is desireable to obtain absolute data. This requires that the instrument be calibrated. A simple method would be to place a specular or diffuse reflector in the chopper cavity whose reflectance is known for each wavelength studied. A standard source having a known spectral dependence can be used to first calibrate for E_0 and then, by use of a set of neutral density filters placed between the reflector and the lens, to calibrate for the much weaker range of scattering signals encountered.

F. The Influence of Second Order Scattering on the Sky Radiation and on the Radiation Emerging From the Earth's Atmosphere Under the Assumption of a Turbid Atmosphere.

1. Introduction.

This paper deals with the computation of the radiation which after having been scattered once { } or twice on the molecules and aerosol particles of the air, reaches the ground or the upper boundary of a model atmosphere which is assumed to be homogeneous and plane parallel. This computation is based upon Bouguer-Lambert's law in a slightly changed from

$$(1) \quad dJ(\lambda) = -\left\{ \sigma_R'(\lambda) + \sigma_D'(\lambda) \frac{H_D}{H_R} \right\} \cdot J(\lambda) \cdot ds \tag{1}$$

where $\sigma_R'(\lambda)$ is the scattering coefficient for the molecular and $\sigma_D'(\lambda)$ for the turbid constituents of the air near the ground under normal conditions. By means of the quotient H_D/H_R it has been taken into account that the homogeneous turbid atmosphere, which is characterized by $\sigma_D'(\lambda)$, does not reach the vertical extension of the homogeneous Rayleigh atmosphere.

If the irradiance $I(\lambda)$[cal sec^{-1} cm^{-2}] is incident upon a volume element dV, the radiance $dJ(\varphi,\lambda)$ [cal sec^{-1} cm^{-2}] is scattered on it under the angle φ:

$$dJ(\varphi,\lambda) = \left\{ f_R'(\varphi,\lambda) + f_D'(\varphi,\lambda) \frac{H_D}{H_R} \right\} \cdot J(\lambda) \cdot dV \tag{2}$$

where $f'_R(\varphi.\lambda)$ is the scattering function for a volume of molecular air and $f'_D(\varphi.\lambda)$ for a volume of turbid air. Both the equations (1) and (2) are based upon the assumption that the aerosol particle size distribution remains the same in the vertical distribution, namely following C Junge's [26] measurements in the air near the ground. The term H_D/H_R in the equation (2) indicates that in case of uniform mixing the concentration in the homogeneous Rayleigh atmosphere is less than in the homogeneous turbid atmosphere.

2. Radiation Received at the Bottom of the Atmosphere.

The direct solar radiation and the global radiation are incident upon the reference plane, which is the earth's surface. However, only the latter radiation is of interest here with emphasis on the primary and secondary scattering.

2.1. Radiation Due to Primary Scattering [27, 28] [1]

According to the ~~Sketch 1~~ Fig. 73, this portion at first penetrates along the path s_1 to the volume element dV_1 and is then scattered on it under the angle φ_1'', towards the point B. The radiation suffers attenuation as well along the path s_1 as s_2''. The expression for this attenuation is

$$d^2 J_H(\varphi_1'',\lambda) = \frac{J_0(\lambda)}{a(\lambda)} \cdot \frac{\sec z_1}{\sec z_0 - \sec z_1} \cdot \bar{f}(\varphi_1'',\lambda) \times \left\{ e^{-a(\lambda)\cdot \sec z_1} - e^{-a(\lambda)\cdot \sec z_0} \right\} d\omega_1 \tag{3}$$

According to the ~~Sketch 1~~ Fig. 73, z is the zenith distance of the beam s_2''. The solid angle $d\omega_1$ is defined through

$$d\omega_1 = \frac{dF_1}{s_2''} \tag{4}$$

where dF_1 is the surface of the volume element dV_1 which points towards B. The scattering function for the entire atmosphere $\bar{f}(\varphi,\lambda)$ is determined through $\bar{f}(\varphi,\lambda) = f_D'(\varphi,\lambda)\ H_D + f_R'(\varphi,\lambda)\ H_R$ and the extinction coefficient $a(\lambda)$ is determined through $a(\lambda) = \sigma_D'(\lambda)\ H_D + \sigma_R'(\lambda)\ H_R$.

2.2. Radiation Due to Secondary Scattering.

Two possibilities are given: The radiation can be scattered upon dV_1 either into the lower or into the upper hemisphere. The following mathematical approach is based upon the slightly modified equation (3) which is now not valid for $b = b_o$ but for $b = b_2$:

$$d^2 J_H^I(\varphi_1,\lambda,b_2) = \frac{J_o(\lambda)}{a(\lambda)} \cdot \frac{\sec z_2}{\sec z_o - \sec z_2} \cdot \bar{f}(\varphi_1,\lambda) \times \left\{ e^{-a(\lambda)\cdot \sec z_2 \cdot \frac{b_2}{b_o}} - e^{-a(\lambda)\sec z_o \cdot \frac{b_2}{b_o}} \right\} d\omega_2 \tag{3a}$$

where the symbol I denotes primary and II secondary scattering. A portion of this radiation is scattered on the volume element dV_2 under the angle φ_2 towards the surface element df. With the help of the equation (2) it is obtained

$$d^5 J_H^I(\varphi_2, \varphi_1, \lambda, b_2) = \frac{J_o(\lambda)}{a(\lambda)} \cdot \frac{\sec z_2}{\sec z_o - \sec z_2} \cdot \bar{f}(\varphi_1, \lambda) \left\{ f_R'(\varphi_2, \lambda) + f_g'(\varphi_2, \lambda) \cdot \frac{H_D}{H_R} \right\}$$

$$\times \left\{ e^{-a(\lambda) \cdot \sec z_2 \cdot \frac{b_2}{b_o}} - e^{-a(\lambda) \cdot \sec z_o \cdot \frac{b_2}{b_o}} \right\} d\omega_2 \, dV_2 \qquad (5)$$

Furthermore, dV_2 can be substituted with

$$dV_2 = \frac{H_R}{b_o} \cdot \sec z_3 \cdot s_3^2 \cdot db_2 \cdot d\omega_3 \qquad (6)$$

and moreover, this scattered radiation is being attenuated along its path s_3 so that it can be written

$$d^5 J_H^I(\varphi_1, \varphi_2, \lambda, b_2) = \frac{J_o(\lambda)}{b_o \cdot a(\lambda)} \cdot \bar{f}(\varphi_1, \lambda) \cdot \bar{f}(\varphi_2, \lambda) \cdot \frac{\sec z_2 \cdot \sec z_3}{\sec z_o - \sec z_2}$$

$$\times \left\{ e^{-\frac{a(\lambda)}{b_o} \left[\sec z_2 \cdot b_2 + \sec z_3 (b_o - b_2) \right]} - e^{-\frac{a(\lambda)}{b_o} \left[\sec z_o \cdot b_2 + \sec z_3 (b_o - b_2) \right]} \right\} d\omega_2 \, d\omega_3 \, db_2 \qquad (7)$$

Now, in order to find the total of all the volume elements dV_2 within the infinitesimal solid angle $d\omega_3$, the equation (7) is integrated over b_2 within the limits $b_2 = 0$ and $b_2 = b_0$:

$$d^4 J_H^I(\varphi_1, \varphi_2, \lambda) = \frac{J_0(\lambda)}{a^2(\lambda)} \cdot \bar{f}(\varphi_1, \lambda) \cdot \bar{f}(\varphi_2, \lambda) \cdot \frac{\sec z_2 \cdot \sec z_3}{\sec z_0 - \sec z_2}$$

$$\times \left\{ \frac{1}{\sec z_0 - \sec z_3} \left[e^{-a(\lambda)\cdot \sec z_0} - e^{-a(\lambda)\cdot \sec z_3} \right] \right. \qquad (8)$$

$$\left. - \frac{1}{\sec z_2 - \sec z_3} \left[e^{-a(\lambda)\cdot \sec z_2} - e^{-a(\lambda)\cdot \sec z_3} \right] \right\} d\omega_2 \, d\omega_3$$

Another final integration over the solid angle $d\omega_2$ is necessary because the volume element dV_2 receives radiation from the entire upper hemisphere which has been scattered once.

Hence, the following radiation which has been scattered twice is received from the solid angle $d\omega_3$ by the surface df:

$$d^2 J_H^I(\lambda) = \frac{J_0(\lambda)}{a^2(\lambda)} \cdot \sec z_3 \left\{ \int_{\alpha_2=0}^{2\pi} \int_{z_2=0}^{\frac{\pi}{2}} \bar{f}(\varphi_1, \lambda) \cdot \bar{f}(\varphi_2, \lambda) \cdot \frac{\sec z_2 \cdot \sin z_2}{\sec z_0 - \sec z_2} \right.$$

$$(9)$$

$$\times \left\{ \frac{1}{\sec z_0 - \sec z_3} \left[e^{-a(\lambda)\cdot \sec z_0} - e^{-a(\lambda)\cdot \sec z_3} \right] \right.$$

$$\left. \left. - \frac{1}{\sec z_2 - \sec z_3} \left[e^{-a(\lambda)\cdot \sec z_2} - e^{-a(\lambda)\cdot \sec z_3} \right] \right\} dz_2 \, d\alpha_2 \right\} d\omega_3$$

The radiation which has first gone upwards and has been scattered on dV_2' is expressed with a similar equation:

$$d^2 J_H^{II}(\lambda) = \frac{J_0(\lambda)}{a^2(\lambda)} \cdot \sec z_3' \left\{ \int_{\alpha_2'=0}^{2\pi} \int_{z_2'=0}^{\frac{\pi}{2}} \bar{f}(\varphi_1',\lambda) \cdot \bar{f}(\varphi_2',\lambda) \cdot \frac{\sec z_2' \cdot \sin z_2'}{\sec z_0 + \sec z_2'} \right.$$

$$\times \left(\frac{1}{\sec z_3' - \sec z_0} \left[e^{-a(\lambda)\cdot \sec z_0} - e^{-a(\lambda) \sec z_3'} \right] \right. \qquad (10)$$

$$\left. - \frac{1}{\sec z_2' + \sec z_3'} \left[e^{-a(\lambda)\cdot \sec z_0} - e^{-a(\lambda)\left[\sec z_0 + \sec z_2' + \sec z_3'\right]} \right] \right)$$

$$\left. dz_2' \, d\alpha_2' \right\} d\omega_3'$$

3. Scattered Radiation Emerging From the Top of the Earth's Atmosphere Without Accounting for the Reflectivity on the Earth's Surface.

This paper does not deal with the reflection by the ground but is restricted to the consideration of the radiation which after having been scattered once or twice resp., is turned back into space.

3.1. Radiation Due to Primary Scattering.

The Scientific Report No 3 AF 61(052)-595 AFCRL, OAR, Jan. 1965[27] contains a detailed derivation of radiation which goes back to space after having been scattered once. Thus, for not being repetitious, only the final equation is presented:

$$d^2 J_B(\varphi_3'', \lambda) = \frac{J_0(\lambda)}{a(\lambda)} \cdot \bar{f}(\varphi_3'') \cdot \frac{\sec z_4''}{\sec z_0 + \sec z_4''} \times \left\{ 1 - e^{-a(\lambda)\cdot\left[\sec z_0 + \sec z_4''\right]} \right\} d\omega_4' \tag{11}$$

where the indices have been slightly changed as against the aforementioned Report, according to the Sketch 2.

3.2. Radiation Due to Secondary Scattering.

Again, two different possibilities must be taken into account: The radiation can first due to primary scattering be turned into the lower hemisphere and then due to secondary scattering back to space. Or the radiation is scattered twice into the upper hemisphere.

The first way via dV_2 is being considered in detail now. The mathematical approach is based upon the equation (3a). According to the equation (2), this radiation is scattered under the angle φ_3 as it is indicated in the ~~Sketch 2~~ Fig. 73. Then, it can be written:

$$d^5 J_B^I(\varphi_3,\lambda) = \frac{J_0(\lambda)}{a(\lambda)\cdot s_4^2} \cdot \bar{f}(\varphi_1,\lambda)\cdot\left\{f_R'(\varphi_3,\lambda) + f_D'(\varphi_3,\lambda)\cdot\frac{H_D}{H_R}\right\}$$

$$\times \frac{\sec z_2}{\sec z_0 - \sec z_2}\left\{ e^{-a(\lambda)\cdot\sec z_2\cdot\frac{b_2}{b_0}} - e^{-a(\lambda)\cdot\sec z_0\cdot\frac{b_2}{b_0}}\right\} d\omega_2\, dV_2 \tag{12}$$

The volume element can be substituted with

$$dV_2 = -\frac{H_R}{b_0}\cdot\sec z_4\cdot s_4^2\, d\omega_4\, db_2 \tag{13}$$

where the infinitesimal solid angle $d\omega_4$ is determined by dV_2 and s_4.

The attenuation along the path s_4 is taken into account by integrating the equation (1) from $b = b_2$ to $b = 0$ and substituting the path element by the pressure

$$ds = -\frac{H_R}{b_0}\cdot\sec z_4\, db \tag{14}$$

Hence

$$d^5 J_8^I(\varphi_1, \varphi_3, \lambda, b_2) = -\frac{J_0(\lambda)}{a(\lambda)\cdot b_0}\cdot \bar{f}(\varphi_1,\lambda)\cdot \bar{f}(\varphi_3,\lambda)\cdot \frac{\sec z_2 \cdot \sec z_4}{\sec z_0 - \sec z_2}$$

$$\times \left\{ e^{-a(\lambda)\cdot[\sec z_2 + \sec z_4]\frac{b_2}{b_0}} - e^{-a(\lambda)\cdot[\sec z_0 + \sec z_2]\frac{b_2}{b_0}} \right\} d\omega_2\, d\omega_4\, db_2 \tag{15}$$

Then, in order to find the total of all the volume elements dV_2 within the infinitesimal solid angle $d\omega_4$, the integration over b_2 must be made from $b_2 = 0$ to $b_2 = b_0$:

$$d^4 J_8^I(\varphi_1, \varphi_3, \lambda) = \frac{J_0(\lambda)}{a^2(\lambda)}\cdot \bar{f}(\varphi_1,\lambda)\cdot \bar{f}(\varphi_3,\lambda)\cdot \frac{\sec z_2 \cdot \sec z_4}{\sec z_0 - \sec z_2}$$

$$\times \left\{ \frac{1}{\sec z_2 + \sec z_4}\left[1 - e^{-a(\lambda)[\sec z_2 + \sec z_4]}\right] - \frac{1}{\sec z_0 + \sec z_4}\left[1 - e^{-a(\lambda)[\sec z_0 + \sec z_4]}\right] \right\} d\omega_2\, d\omega_4 \tag{16}$$

Finally, the integration over the solid angle ω_2 furnishes the total radiation due to secondary scattering which is incident upon the surface dF, from the cone $d\omega_4$:

$$d^2 J_g^{I}(\varphi_1,\varphi_3,\lambda) = \frac{J_0(\lambda)}{a^2(\lambda)} \cdot \sec z_4 \left\{ \int\limits_{\alpha_2=0}^{2\pi} \int\limits_{z_2=0}^{\frac{\pi}{2}} \bar{f}(\varphi_1,\lambda)\cdot \bar{f}(\varphi_3,\lambda) \times \frac{\sec z_2 \cdot \sin z_2}{\sec z_0 - \sec z_2} \left\{ \frac{1}{\sec z_2 + \sec z_4}\left[1 - e^{-a(\lambda)\cdot[\sec z_2 + \sec z_4]}\right] - \frac{1}{\sec z_0 + \sec z_4}\left[1 - e^{-a(\lambda)[\sec z_0 + \sec z_4]}\right] dz_2\, d\alpha_2 \right\} d\omega_4 \qquad (17)$$

The relevant equation for the way via dV_2' reads:

$$d^2 J_g^{II}(\varphi_1',\varphi_3',\lambda) = \frac{J_0(\lambda)}{a^2(\lambda)} \cdot \sec z_4 \left\{ \int\limits_{\alpha_2'=0}^{2\pi} \int\limits_{z_2'=0}^{\frac{\pi}{2}} \bar{f}(\varphi_1',\lambda)\cdot \bar{f}(\varphi_3',\lambda) \times \frac{\sec z_2' \cdot \sin z_2'}{\sec z_0 + \sec z_2'} \cdot \left\{ \frac{1}{\sec z_0 + \sec z_4'}\left[1 - e^{-a(\lambda)[\sec z_0 + \sec z_4']}\right] - \frac{1}{\sec z_4' - \sec z_2'}\left[e^{-a(\lambda)[\sec z_0 + \sec z_2']} - e^{-a(\lambda)[\sec z_0 + \sec z_4']}\right] \right\} dz_2'\, d\alpha_2' \right\} d\omega_4' \qquad (18)$$

The very complicated equations (9), (1o), (17), and (18) enable one to compute the radiant flux due to secondary scattering in the atmosphere. Unfortunately, the evaluation of these equations is a rather difficult task, so that it appears necessary to give a brief discussion of the numerical methods.

4. Numerical Evaluation.

The first difficulty results from the fact that the numerical values of the scattering function for turbid air $\overline{f}_D(\varphi,\lambda)$ are available only for discrete angles φ_i. Now, the scatter angles φ depend on the zenith distances of the sun z_o, the zenith distances of the scattered beams z and the angles of azimuth α. An example is given for the angle φ_2 in the equation (17):

$$\cos\varphi_2 = \sin z_2 \cdot \sin z_3 \cdot \cos\alpha_2 \cdot \cos\alpha_3 + \sin z_2 \cdot \sin z_3 \cdot \sin\alpha_2 \cdot \sin\alpha_3 + \cos z_2 \cdot \cos z_3 \tag{19}$$

Obviously, φ_2 depends on the arbitrary selection of the discrete prop values (z_2, α_2) for the numerical integration and on the direction of the incident scattered radiation (z_3, α_3); it is mere chance if the numerical value of φ_2 coincides with one of the discrete angles φ_i. That could be helped by fitting an interpolation parabolic curve in between three consecutive values φ_{i-1}, φ_i and φ_{i+1} each.

Hence, the numerical integration has been done in the following way: With a set of three functional values f_i, f_{i+1}, f_{i+2} at the points t_i, t_{i+1}, t_{i+2} a Newton's interpolation polynomial has been established

$$F_i(t) = \gamma_1^{(i)} + \gamma_2^{(i)}(t - t_i) + \gamma_3^{(i)}(t - t_i)(t - t_{i+1}) \tag{2o}$$

where the coefficients $\gamma_1^{(i)}$, $\gamma_2^{(i)}$ and $\gamma_3^{(i)}$ are determinable. Then, this function $F_i(t)$ has been integrated over the interval $[t_i, t_{i+1}]$.

5. Discussion of the Results.

5.1. Selection of the Parameters.

The equations (3), (9), (1o) or (11) resp., (17) and (18) which have been described in the previous sections, have been used for computing the intensities received after primary and secondary scattering at various zenith distances of the sun z_0, and at various wavelengths λ and turbidity factors T.

The latter is included as well in the scattering function according to

$$\bar{f}_D(\varphi, \lambda, T) = (T-1) \cdot \bar{f}_D(\varphi, \lambda, T=2) \tag{21}$$

as in the extinction coefficient according to

$$a_D(\lambda, T) = (T-1) \cdot a_D(\lambda, T=2) \tag{22}$$

The following numerical values of the parameters have been selected: Wavelengths λ = 0.45 μ, 0.65 μ, 0.85 μ; two zenith distances of the sun z_o = 37°, 78°; the turbidity factors T = 2, 4, 6. Finally, it has to be mentioned that the monochromatic solar radiation has been set $I_o(\lambda) = \pi.10^3$ [cal cm^{-2} sec^{-1}] and the solid angles have been set $d\omega_i$ = 1 str (i = 1, 2, 4) so that the results which will be discussed are relative values. According to the mathematical approach, the irradiances I(λ) refer to a surface which is normal to the incident beam.

5.2. The Scattered Radiation Received at the Bottom of the Earth's Atmosphere.

The results of the computation will be interpreted with the help of a few typical examples. The way of presentation is the following: The diamter of the semicircle represents the sun's vertical. This diamter is subdivided in equidistant values of the zenith distance z which run from the center M in two different directions up to the intersection with the arc of the semicircle. The angles of azimuth α run along the periphery from α = 0° up to α = 180°; in the Fig. 74 the angles ψ = 30°, 60°, 90°, 120° and 150° are also marked. Thus, each point (z, α) in the graph is related with a direction from which an observer in the point M receives scattered radiation.

The effect of scattering is strongest in a turbid atmosphere with a great turbidity factor T and at a small wavelength λ as it is already indicated by the extinction coefficient. An instructive example is given with the parameters T = 6, λ = 0.45 μ and the zenith distance of the sun z_o = 37°.

The graphs with the index a show the radiation due to primary scattering which is received as sky radiation from different directions at the earth's surface or at the top of the earth's atmosphere resp. The graphs with the index b present the radiation due to primary and secondary scattering. The graphs with the index c show only the radiation due to secondary scattering. Finally, the graphs with the index d give the ratio of the radiation due to secondary scattering to that due to primary scattering if the latter is set 100%.

The comparison of the Figures 74a and 74b proves that close to the sun it does not make much difference whether the effect of secondary scattering is accounted for or not; the Figure 74d shows no more than 5% increase in radiance in this area. However, the greater the angular distance from the sun, the greater the rate of increase of radiation due to secondary scattering, which near the horizon is almost doubled in amount. The isolines of percentage increase are almost circles around the minimum which marks the respective position of the sun. The numerous equidistant curves prove the strong continuous increase of the effect of secondary scattering. It can be seen from the Figure 74c that the absolute increase of the effect of secondary scattering is a gradual one. The minimum for both primary and secondary scattering is located in the sun's vertical opposite to the sun ($\alpha = 180°$). Towards the horizon ($z \approx 75° - 80°$) a slight increase in intensity can be seen and a relative maximum shows as a band of high intensity. Both the maxima are located at the side of the sun: The first coincides with the position of the sun, the second falls within the aforementioned band. Thus, the great portion of forward scattering due to the turbid atmosphere which is so characteristic for primary scattering, also shows with secondary scattering.

In case of a small extinction coefficient a(λ), namely for T = 2 and the wavelength λ = o.85 μ, quite a change is observed. The percentage increase in the Fig. 75d reaches a maximum value of only a little more than 15% and goes down in the minimum to about 1%. The Fig. 75c shows that most of the raditation which has been scattered twice comes from near the horizon and the isolines of intensity are circles around the minimum located at $z \approx 22°$ and $\alpha = 18o°$.

5.3. The Scattered Radiation Received at the Top of the Earth's Atmosphere.

The Figures 76 and 77 refer to the same parameters z_0, λ, and T as in the Figures 74 and 75 ; however, the Figures 76 and 77 show the scattered radiation which is received at the top of the earth's atmosphere. The comparison between the graphs 76c and 77c as well as 76d and 77d proves that the radiance due to secondary scattering is greatest at great extinction coefficients; this is true with the relative as well as with the absolute values.

The isolines of scattered radiance ($z_0 = 37°$, λ = o.45 μ, T = 6) are similar in both shape and position for primary as well as secondary scattering since they surround the minimum nearly as circles in the graphs 76a and 76c . This minimum, however, has shifted from a position at $z \approx 25°$ for primary scattering to in between $z = 5°$ and $z = 1o°$ for secondary scattering.

According to the graph 76d, a band of greatest relative increase runs between both the minima, i. e. that at $z \approx 3o°$,

α = 18o° and that at the horizon. The proportion of the radiation due to secondary scattering partly amounts to more than 5o‰ of the radiation due to primary scattering.

In case of a small extinction coefficient related with λ = o.85 μ and T = 2 (Fig. 77), there cannot be seen any basic change. In accordance with the sky radiation, the radiation due to secondary scattering shows only a little increase, both in the relative and absolute values. It is a striking feature of the graph 77d that this increase is distributed very uniformly into all directions. The percentages vary only between 6‰ and 16‰ and the maximum has been displaced towards the horizon compared with its location at λ = o.45 μ and T = 6.

5.4. Scattered Radiation in the Sun's Vertical.

The influence of secondary scattering is most conspicuous if the intensities in the sun's vertical are plotted on semi-logarithmic paper.

The Fig. 78 shows the distribution of the sky radiation if at a high constant turbidity (T = 6) the zenith distance of the sun and the wavelength vary. The position of the sun is marked with an arrow where the curves break off, because the intensities have not been computed for $z = z_o$.

The comparison between the curves a and b proves the decreasing influence of secondary scattering when z approaches z_o, i. e. comes close to the sun; for both the curves gradually move together. This is true with both solar positions and both wavelengths. At a great distance from the sun, however, the relevant pairs of curves for primary scattering $I(\lambda)_I$ as well as primary and secondary scattering $I(\lambda)_{I+II}$ branch off the more the smaller the wavelength grows. Thus, the influence of secondary scattering increases with decreasing wavelength.

The Fig. 79 refers to the same parameters as in Fig. 78 ; however, the Fig. 79 shows the scattered radiation which is received at the top of the earth's atmosphere. Again, the predominance of secondary scattering at small wavelengths is striking though it does not reach as great a value as with the sky radiation. The arrows in the graph mark the directions of the point in opposition to the sun $\bar{z}_0$. When the intensities due to primary scattering become very great due to strong forwardscattering (α = 0 and z is great), the influence of secondary scattering diminishes at a low sun.

6. Concluding Remarks.

So far, only those intensities have been computed which due to primary and secondary scattering in the turbid atmosphere can be received at the earth's surface or at the top of the earth's atmosphere resp. Future computations must account for the reflectivity of the earth's surface, too. It is intended to take into account not only the diffuse reflection according to Lambert's cosine law but also the partly specular reflection. The measurements taken by Blättner which are presented in this Report will be very suitable for this purpose.

Acknowledgements.

We gratefully acknowledge the support of this study by Contract with the Air Force Cambridge Research Laboratories, through the European Office of Aerospace Research, Brussels.

We like to thank Dr. R. Fenn and Mr. R. B. Toolin for their help, Dr. Mark W. Jones and Dr. L. Elterman who gave the permission to perform measurements at the Two Buttes and to use the facilities there. Furthermore, we are indebted to Mr. Donald Dayton, superintendent of the White Sands National Park, who gave the permission to carry out measurements in the Park. We also thank Lt. Col. R. C. Clemenson and Mr. M. Brown at Holoman Air Force Base. They gave us any assistance we needed.

References.

1. E. de Bary, B. Braun, K. Bullrich (1965): Tables related to light scattering in a turbid atmosphere. AFCRL-65-71o (I-III), Special Reports, No. 33. Optics Physics Lab. Hanscom Field, Bedford, Mass., USA.
2. F. Volz (1956): Handb. der Geophysik, 8, 822.
3. F. Kasten: Beitr. z. Physik der Atm., to be published in 1968.
4. C. Junge (1966): Studies of the Chemistry of Unpolluted Atmospheres, p. 17. Standford Res. Inst. Menlo Park, Cal., USA. Contr. No. Cwb-11151. Dept. of Commerce.
5. D. Plass (1967): Eine photographische Methode zur Messung der Intensitätsverteilung der Himmelsstrahlung, Optik 25, 162.
6. H. C. van de Hulst (1957): Light Scattering by Small Particles.
7. E. Schoenberg (1929): Theoretische Photometrie, Handbuch der Astrophysik 11, 1.
8. E. Schoenberg (1926): Untersuchungen zur Theorie der Beleuchtung des Mondes auf Grund photometrischer Messungen, Acta Societatis Scient. Fennicae 50.
9. B. Hapke (1963): A Theoretical Photometric Function for the Lunar Surface, J. o. Geoph. Res. 68 (15), 4571.
10. K. L. Coulson, G. M. Bouricius (1965): Optical Reflection Properties of Natural Surfaces, J. o. Geoph. Res. 7o, 46o'.
11. K. L. Coulson (1966): Effects of Reflection Properties of Natural Surfaces in Aerial Reconnaissance, Appl.Opt.5, 9o5.

12. K. L. Coulson, G. M. Bouricius, E. L. Gray (1965): A Study of the Reflection and Polarization Characteristics of Selected Natural and Artificial Surfaces, R 65 SD 4.

13. E. Ashburn, R. Weldon (1956): Spectral Diffuse Reflectance of Desert Surfaces, J. o. Opt. Soc. o. Amer. 46 (8).

14. W. E. Ranz, J. B. Wong (1952): Impaction of Dust and Smoke Particles on Surface and Body Collectors, Industrial and Engineering Chemistry 51, 1o39.

15. M. Knudsen, S. Weber (1911): Air Resistance Against the Slow Movement of Small Spheres, Annalen der Physik, 36, 981.

16. E. S. Pettyjohn, E. B. Christiansen (1948): Effect of Particle Shape on Free Settling Rates of Isometric Particles, Chemical Engineering Progress, 44, 157.

17. J. S. McNown, J. Malaika (195o): Effect of Particle Shape on Settling Velocity at Low Reynolds Numbers, Transactions American Geophysical Union, 31, 74.

18. W. B. Kunkel (1948): Magnitude and Character of Errors Produced by Shape Factors in Stokes' Law Estimates of Particle Radius, J. o. Appl. Phys., 19, 1o56.

19. K. Bullrich, E. de Bary, W. Blättner, R. Eiden, G. Hänel, W. Nowak (1967): Research on Atmospheric Optical Radiation Transmission, Sci. Rpt. No 5 USAF 61(o52)-595, Cambridge Research Lab., Bedford, Mass., USA.

2o. R. Fenn (1964): Aerosol Distribution and Scattered Atmospheric Light, Beitr. Phys. d. Atm., 37, 69.

21. S. C. Stern, H. W. Zeller, A. I. Schekman (1962): Collection Efficiency of Jet Impactors at Reduced Pressures, I + EC Fundamentals, 1, 273.

22. J. M. Waldram (1945): Transactions of the Illuminating Society, London, 8, 147.

23. S. Q. Duntley, A. R. Boileau, R. W. Preissendorfer (1957): JOSA, 47, 499.

24. J. C. Johnson (1954): J. of Meteorology, 11, 431.

25. J. C. Johnson (1954): Physical Meteorology, MIT Press, 44.

26. C. Junge (1952): Ber. d. Dtsch. WD. in d. US-Zone Nr. 35.

27. K. Bullrich, E. de Bary, K. Danzer, R. Eiden, K. Heger (1965): Scientific Report No 3, Contr. AF 61(o52)-595.

28. K. Heger (1965): Die von der trüben Atmosphäre nach aussen gestreute Strahlung, Beitr. Phys. d. Atm., 38,

1

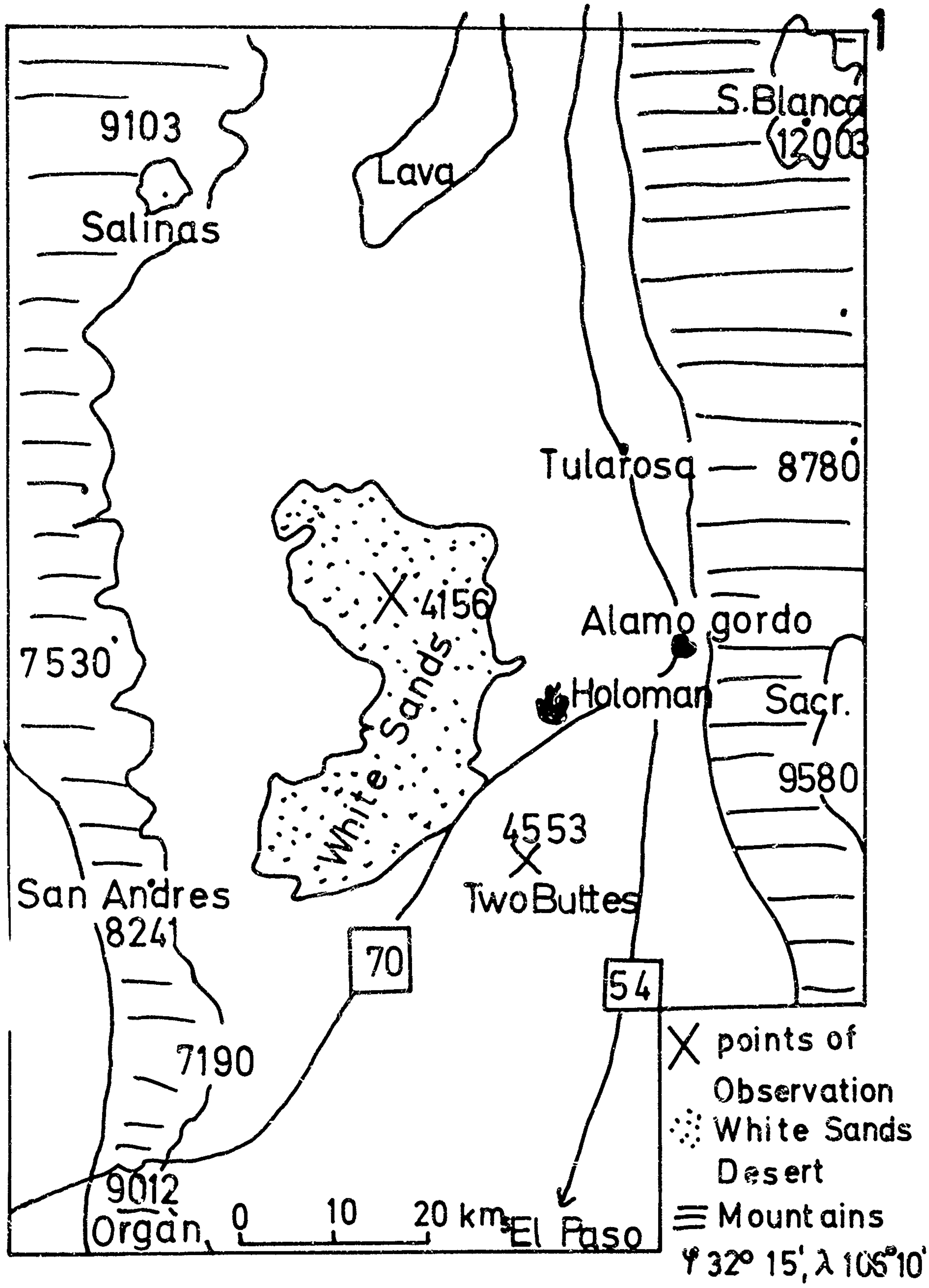
9103
Salinas
Lava
S.Blanca
12003
Tularosa
8780
4156
White Sands
Alamo gordo
Holoman
Sacr.
9580
7530
4553
Two Buttes
San Andres
8241
70
54
7190
9012
Organ
0
10
20 km
El Paso
points of Observation
White Sands Desert
Mountains
φ 32° 15', λ 106°10'

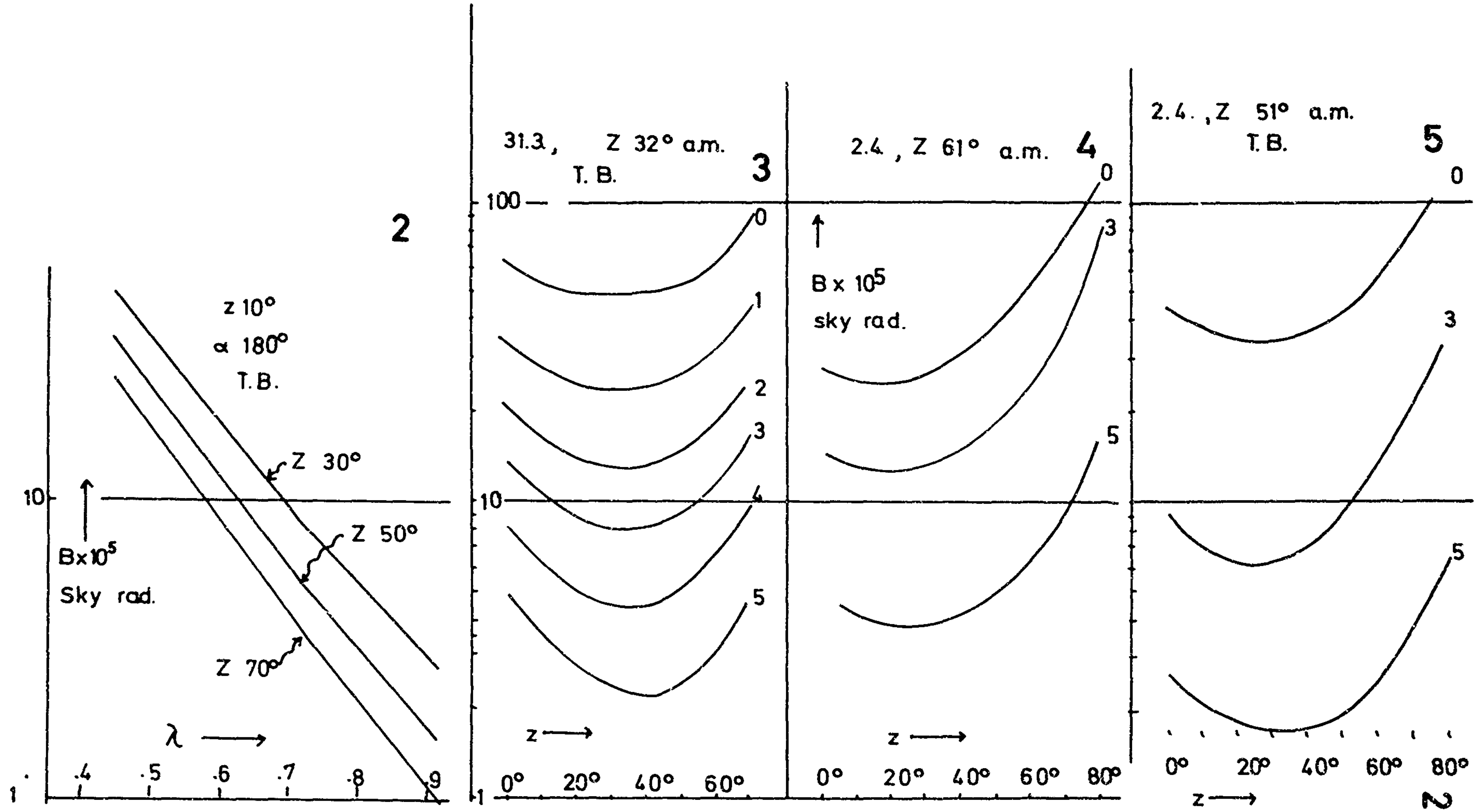
2
z 10°
α 180°
T.B.
Z 30°
Z 50°
Z 70°
B x 10^5
Sky rad.
λ
.4 .5 .6 .7 .8 .9
1
10
100
3
31.3, Z 32° a.m.
T. B.
0
1
2
3
4
5
z
0° 20° 40° 60°
4
2.4 , Z 61° a.m.
B x 10^5
sky rad.
0
3
5
z
0° 20° 40° 60° 80°
5
2.4. , Z 51° a.m.
T.B.
0
3
5
0° 20° 40° 60° 80°
z
2-5

6-9

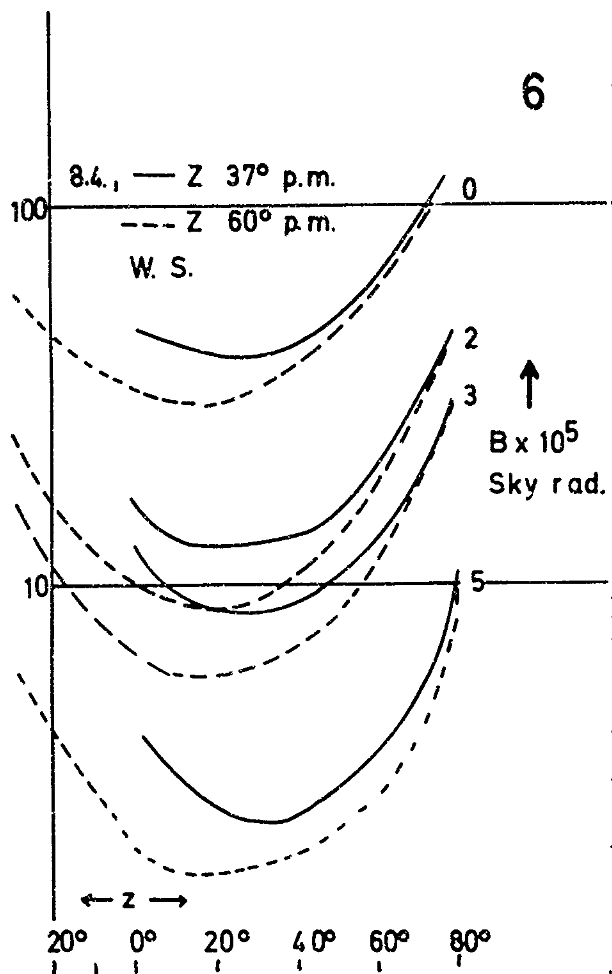
6
8.4., — Z 37° p.m.
--- Z 60° p.m.
W. S.
100
10
0
2
3
5
B x 10^5
Sky rad.
← z →
20° 0° 20° 40° 60° 80°

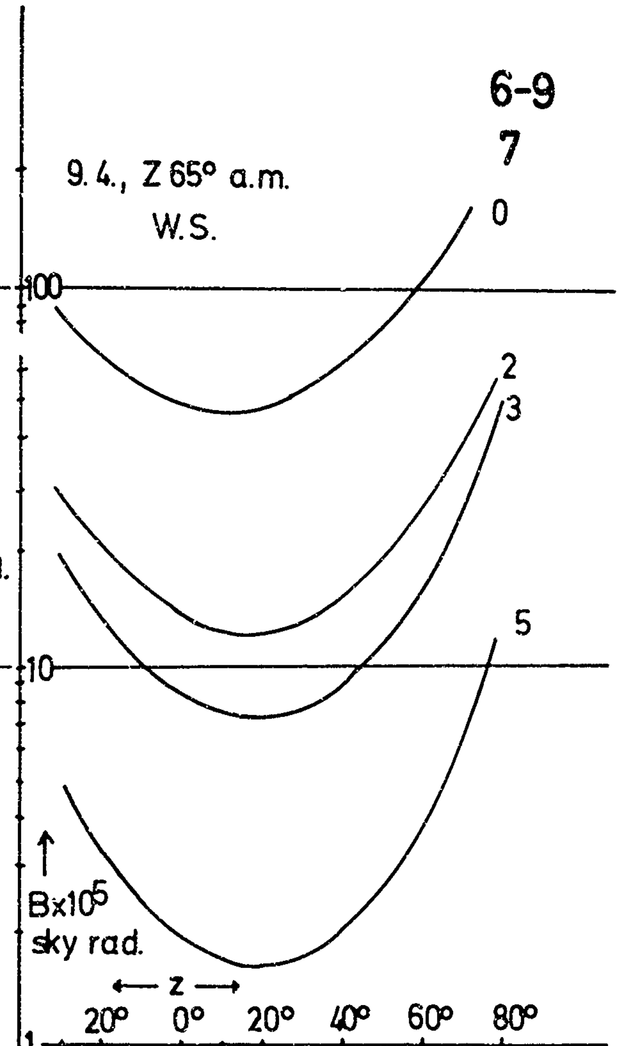
7
9. 4., Z 65° a.m.
W.S.
100
10
1
0
2
3
5
Bx10^5
sky rad.
← z →
20° 0° 20° 40° 60° 80°

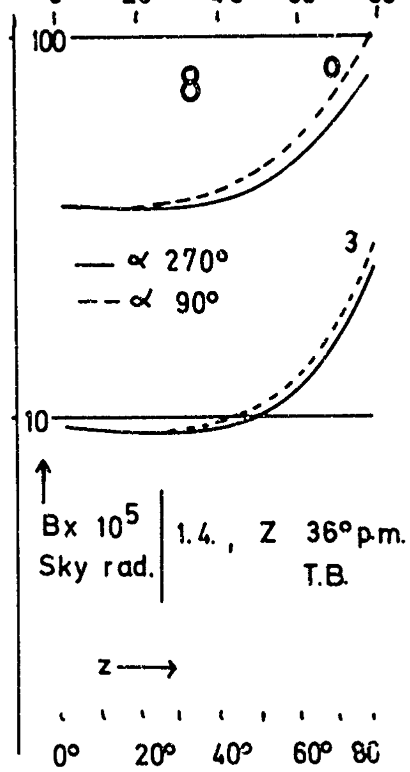
8
100
10
0
3
— ∝ 270°
--- ∝ 90°
Bx 10^5
Sky rad.
1.4., Z 36° p.m.
T.B.
z ⟶
0° 20° 40° 60° 80

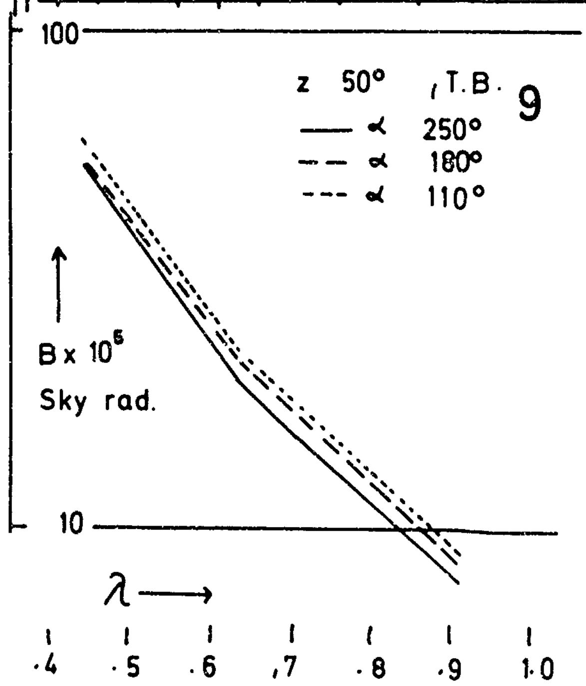
9
z 50° , T.B.
— ∝ 250°
-- ∝ 180°
--- ∝ 110°
100
10
B x 10^5
Sky rad.
λ ⟶
·4 ·5 ·6 ,7 ·8 ·9 1·0

10-12

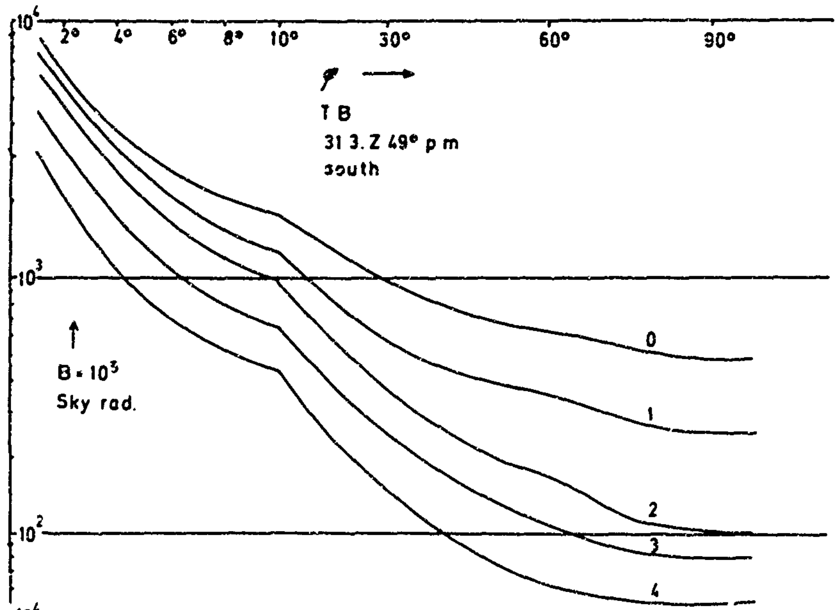
10^4
2° 4° 6° 8° 10° 30° 60° 90°
$\varphi \rightarrow$
T B
31 3. Z 49° p m
south
10^3
B = 10^3
Sky rad.
0
1
2
3
4
10^2

10

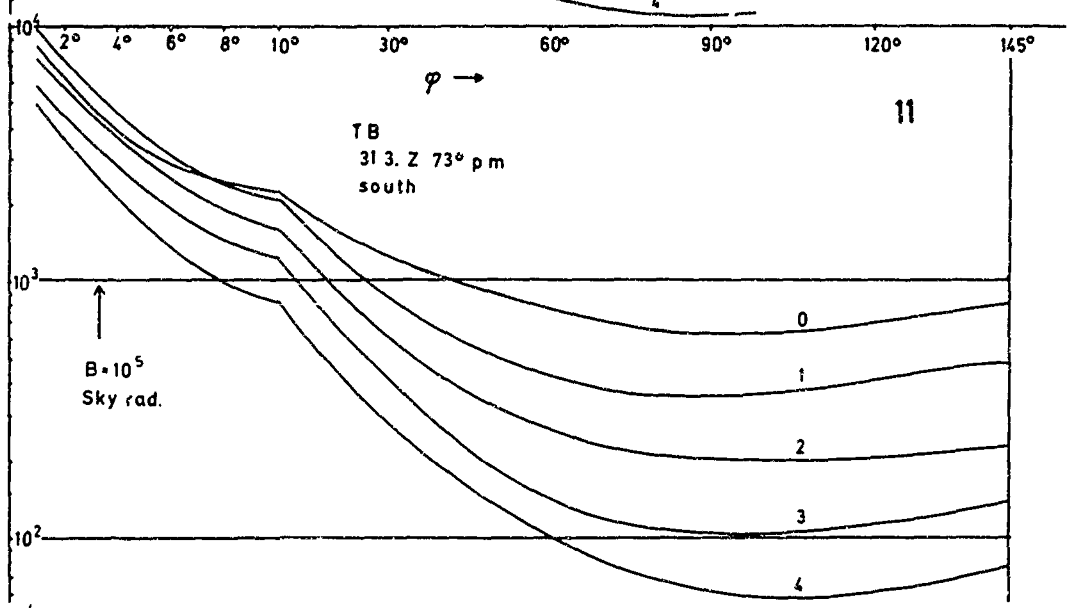
10^4
2° 4° 6° 8° 10° 30° 60° 90° 120° 145°
$\varphi \rightarrow$
T B
31 3. Z 73° p m
south
10^3
B = 10^5
Sky rad.
0
1
2
3
4
10^2

11

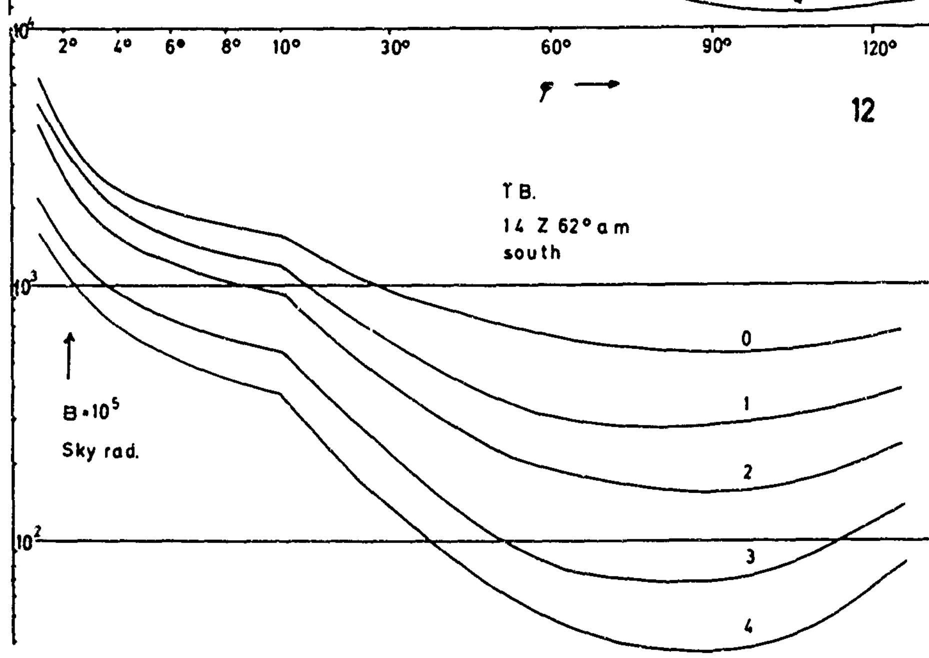
10^4
2° 4° 6° 8° 10° 30° 60° 90° 120°
$\varphi \rightarrow$
T B.
14 Z 62° a m
south
10^3
B = 10^5
Sky rad.
0
1
2
3
4
10^2

12

13-15

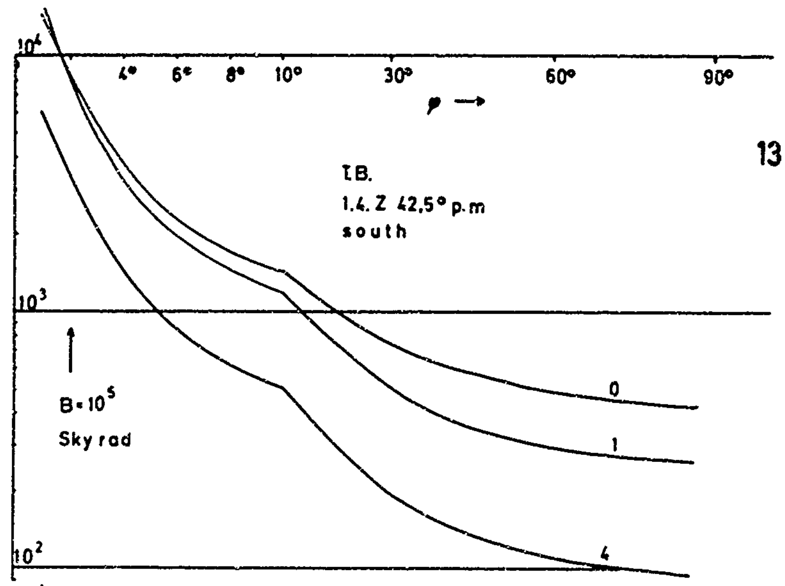

10⁴
4° 6° 8° 10° 30° 60° 90°
φ →
13
T.B.
1.4. Z 42,5° p.m
south
10³
B·10⁵
Sky rad
0
1
4
10²

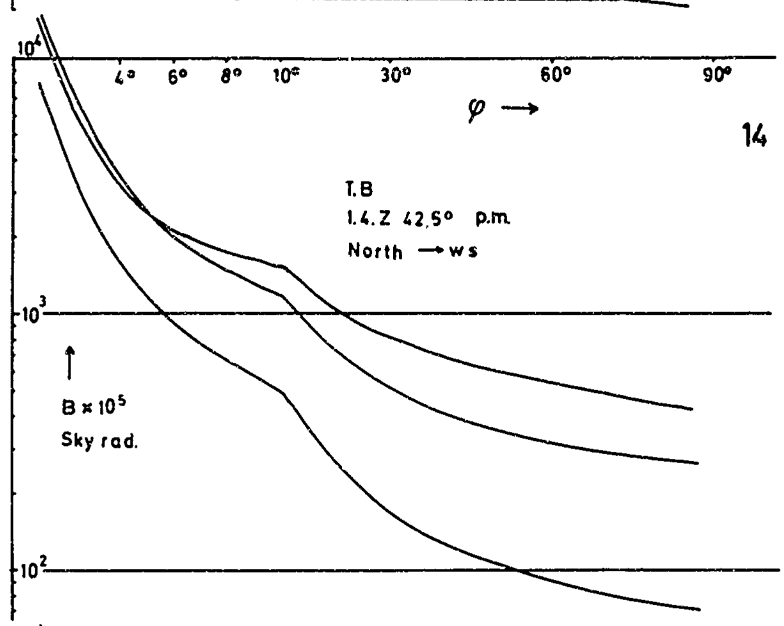

10⁴
4° 6° 8° 10° 30° 60° 90°
φ →
14
T.B
1.4. Z 42,5° p.m.
North → ws
10³
B × 10⁵
Sky rad.
10²

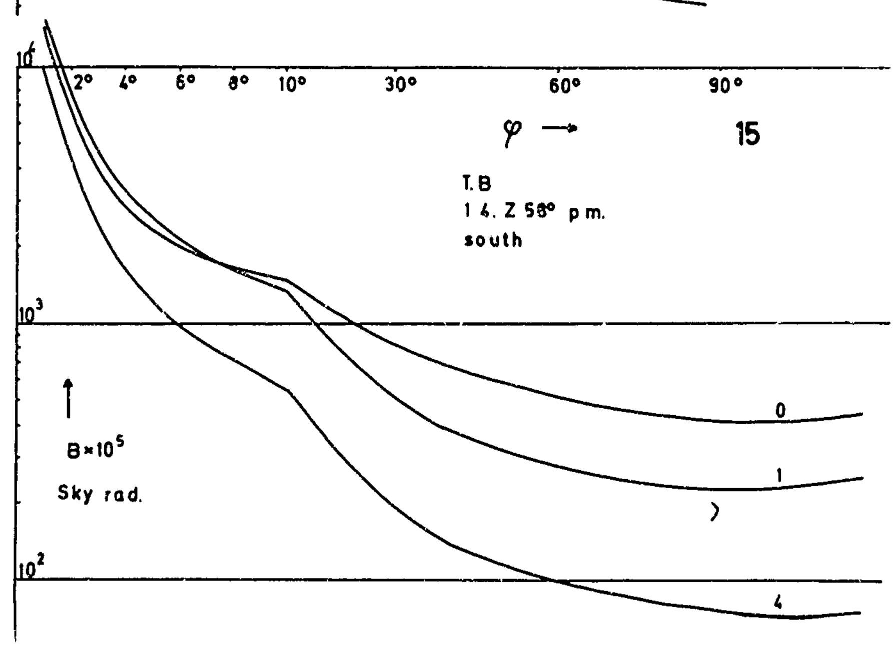

10⁴
2° 4° 6° 8° 10° 30° 60° 90°
φ →
15
T.B
1.4. Z 58° p.m.
south
10³
B×10⁵
Sky rad.
0
1
4
10²

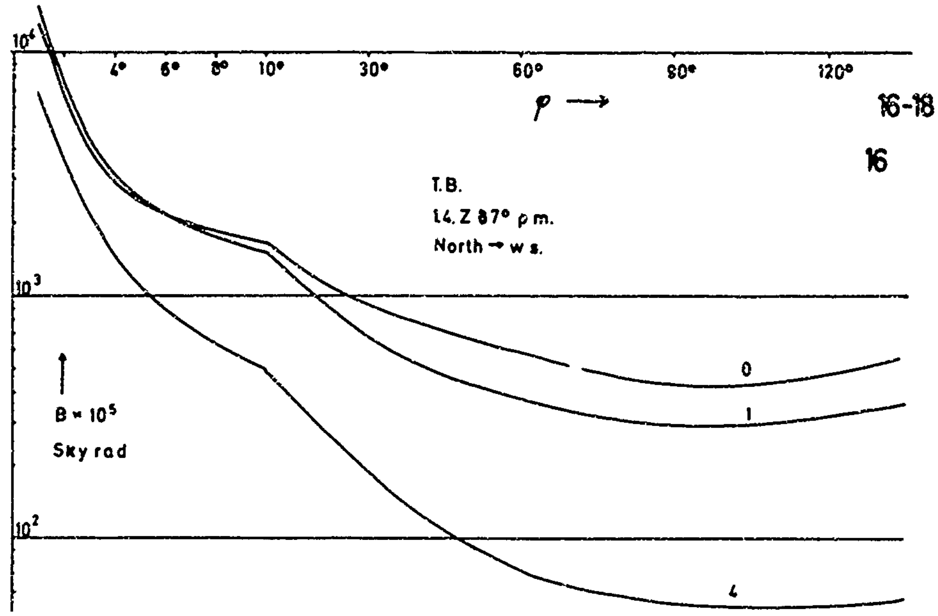

16-18
16
10^4
4° 6° 8° 10° 30° 60° 80° 120°
$\varphi \longrightarrow$
T.B.
14. Z 87° p.m.
North → w s.
10^3
10^2
↑
B × 10^5
Sky rad
0
1
4

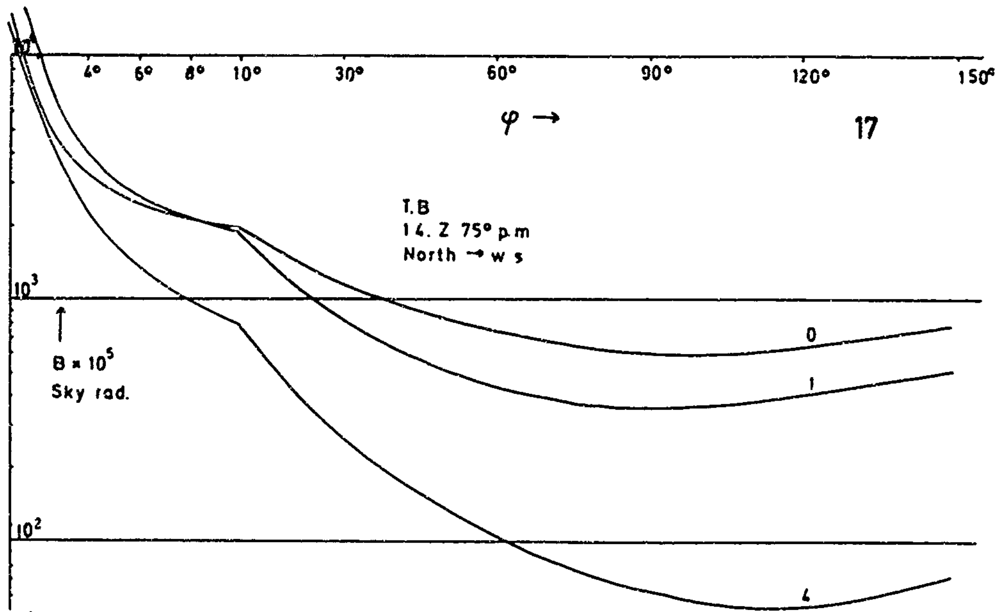

17
4° 6° 8° 10° 30° 60° 90° 120° 150°
$\varphi \rightarrow$
T.B
14. Z 75° p.m
North → w s
10^3
10^2
↑
B × 10^5
Sky rad.
0
1
4

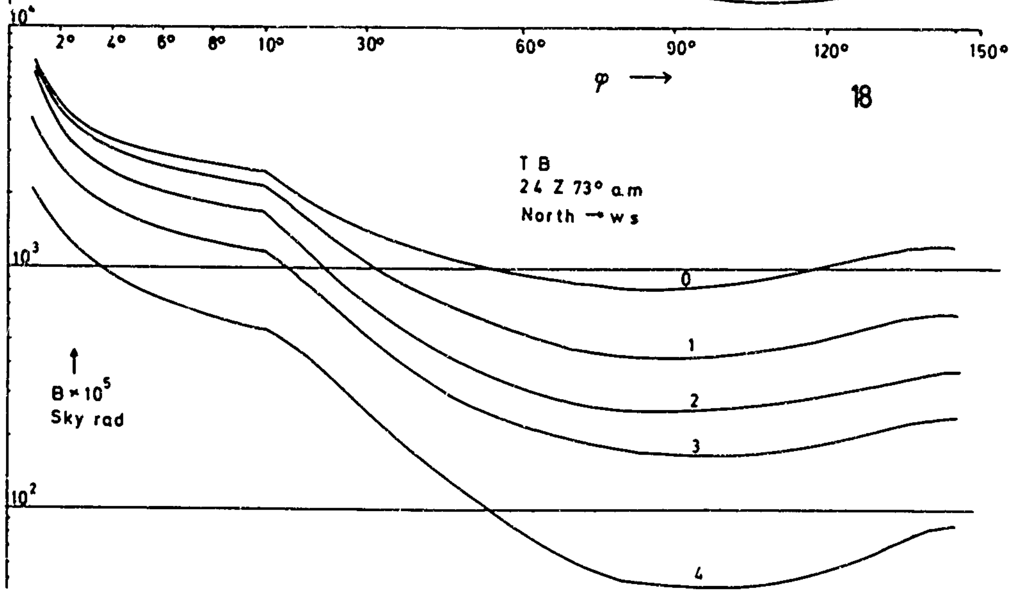

18
10^4
2° 4° 6° 8° 10° 30° 60° 90° 120° 150°
$\varphi \longrightarrow$
T.B
24 Z 73° a.m
North → w s
10^3
10^2
↑
B × 10^5
Sky rad
0
1
2
3
4

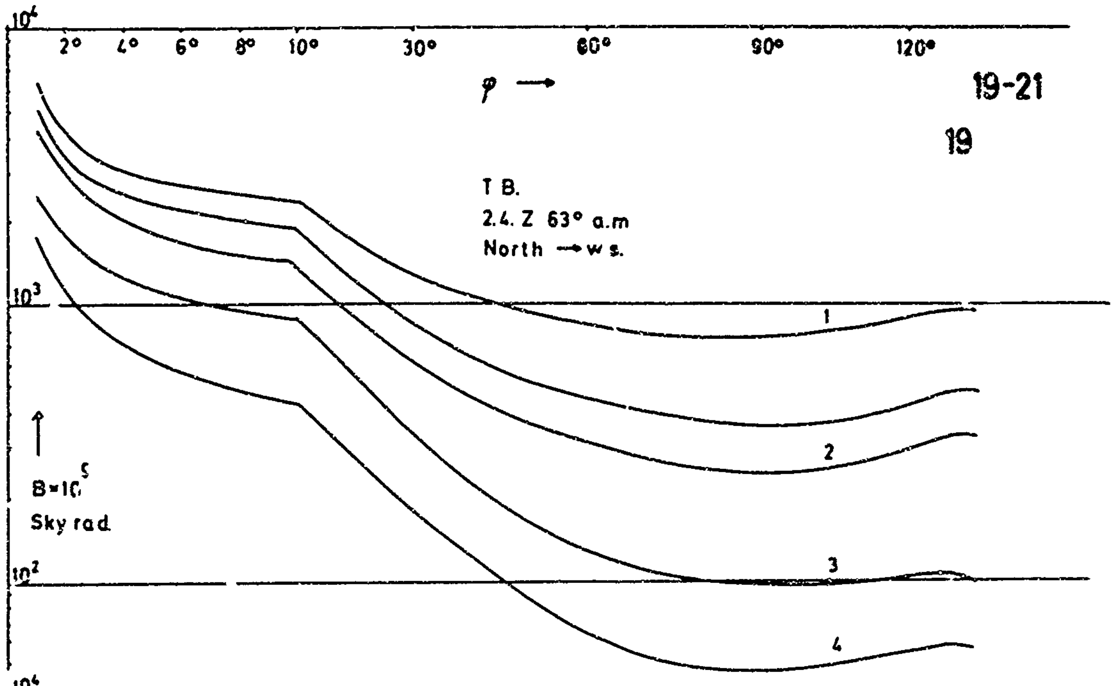
19-21
19
T B.
2.4. Z 63° a.m
North → w s.
B×10^5
Sky rad.

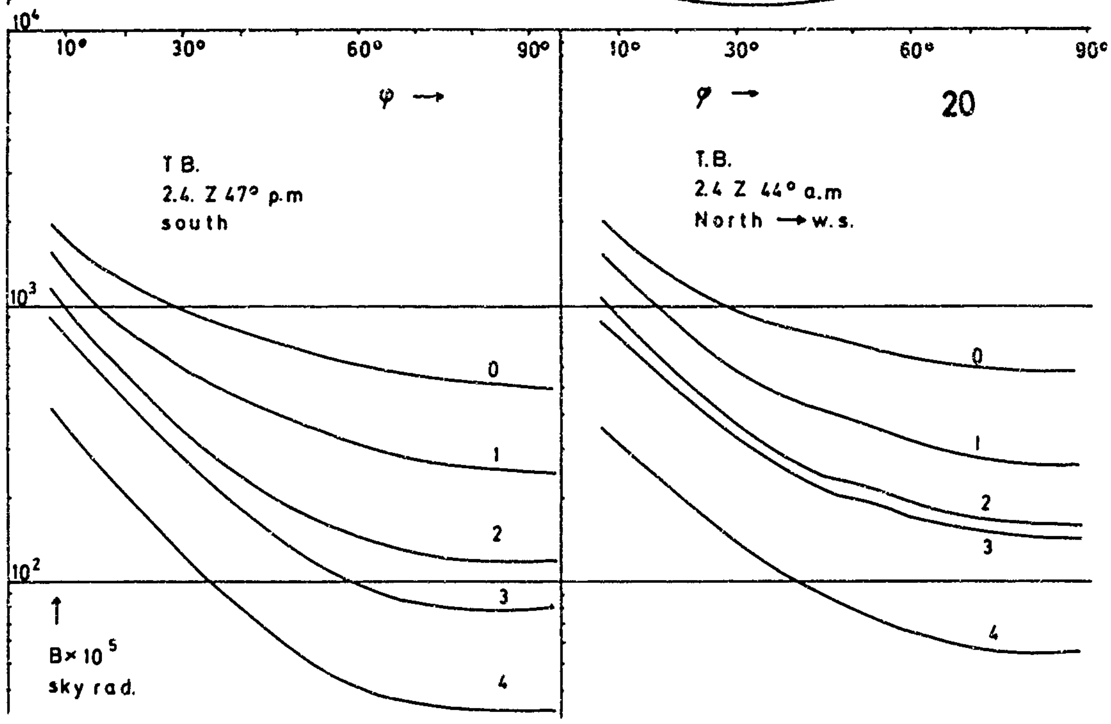
20
T B.
2.4. Z 47° p.m
south
T.B.
2.4 Z 44° a.m
North → w.s.
B×10^5
sky rad.

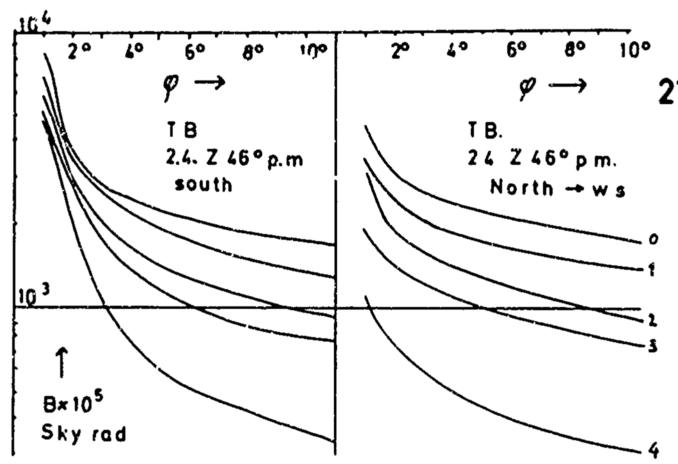
21
T B
2.4. Z 46° p.m
south
T B.
2 4 Z 46° p m.
North → w s
B×10^5
Sky rad

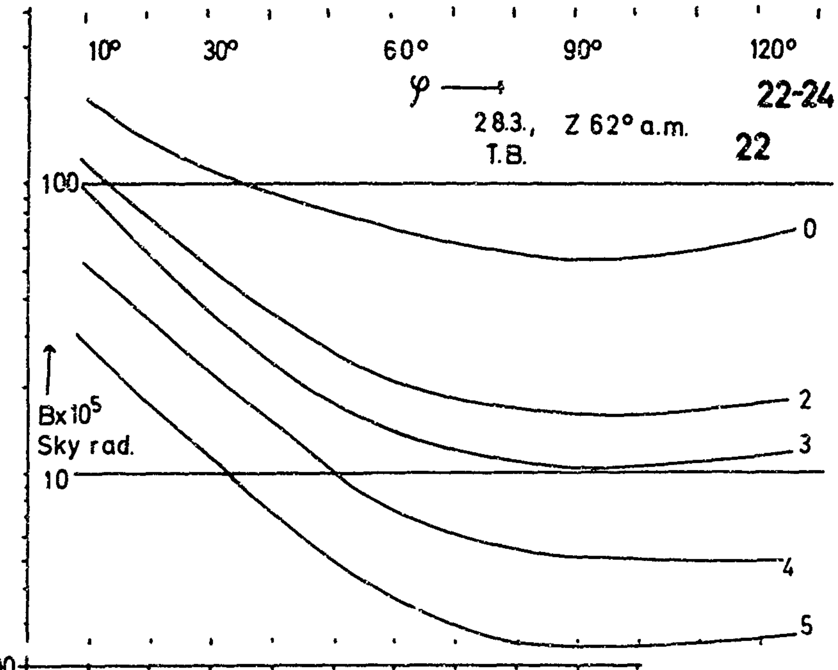
10° 30° 60° 90° 120°
φ ⟶
22-24
28.3., Z 62° a.m.
T.B.
22
100
10
Bx10⁵
Sky rad.
0
2
3
4
5

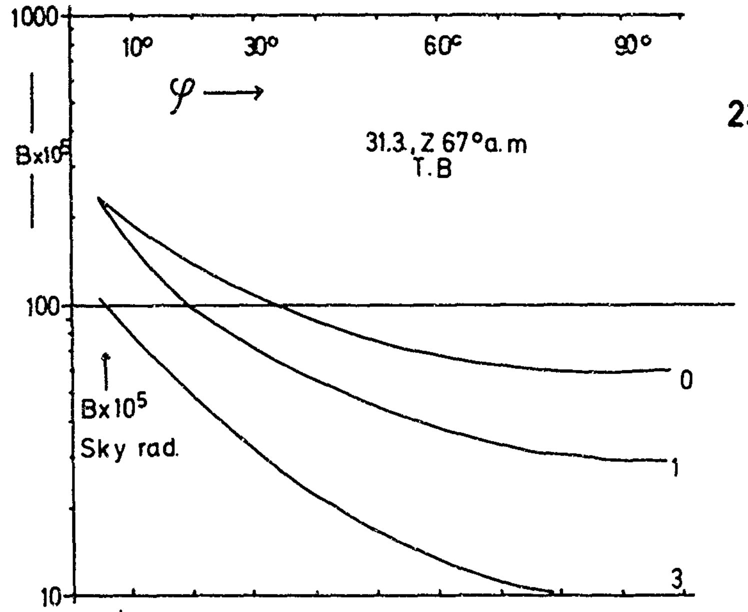
1000
10° 30° 60° 90°
φ ⟶
23
31.3., Z 67° a.m
T.B
Bx10⁵
100
Bx10⁵
Sky rad.
10
0
1
3

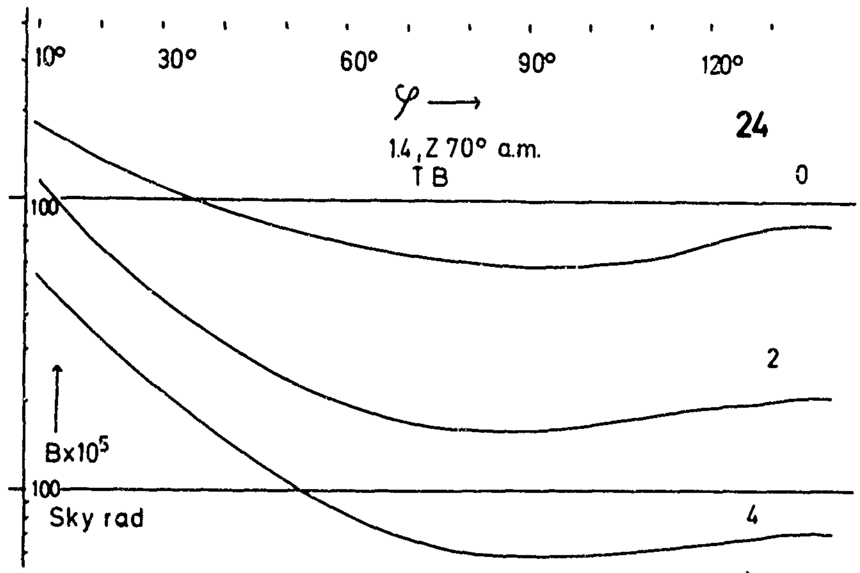
10° 30° 60° 90° 120°
φ ⟶
24
1.4, Z 70° a.m.
T B
100
Bx10⁵
100
Sky rad
0
2
4

25-27

25

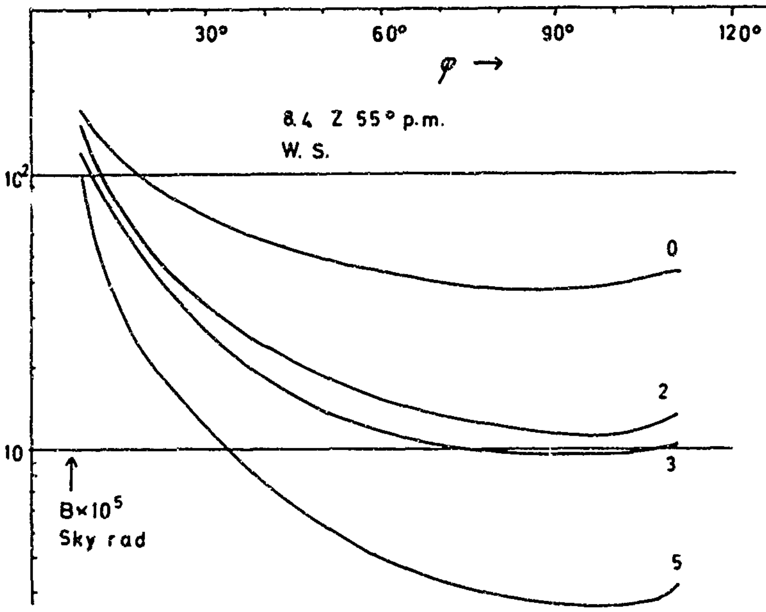
30°
60°
90°
120°
φ →
8.4 Z 55° p.m.
W. S.
10²
10
0
2
3
5
B×10⁵
Sky rad

26

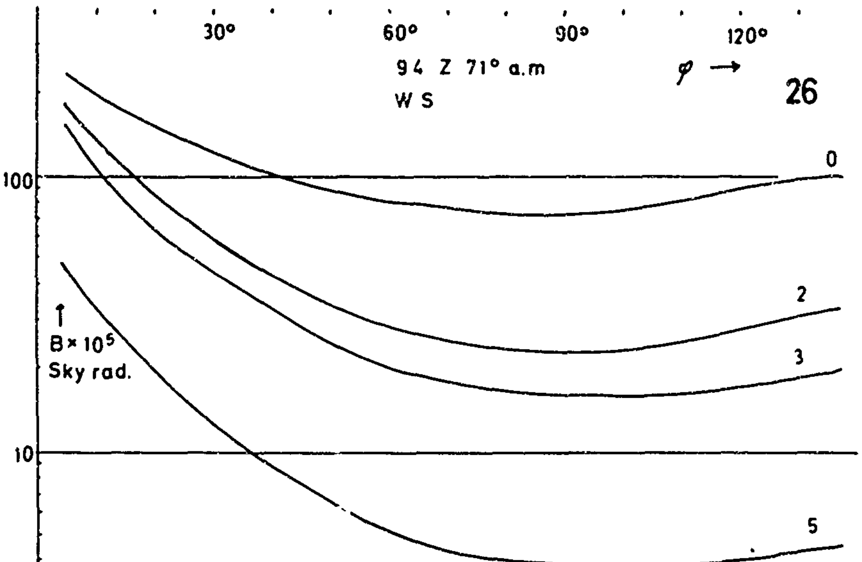
30°
60°
90°
120°
9 4 Z 71° a.m
W S
φ →
100
10
0
2
3
5
B×10⁵
Sky rad.

27

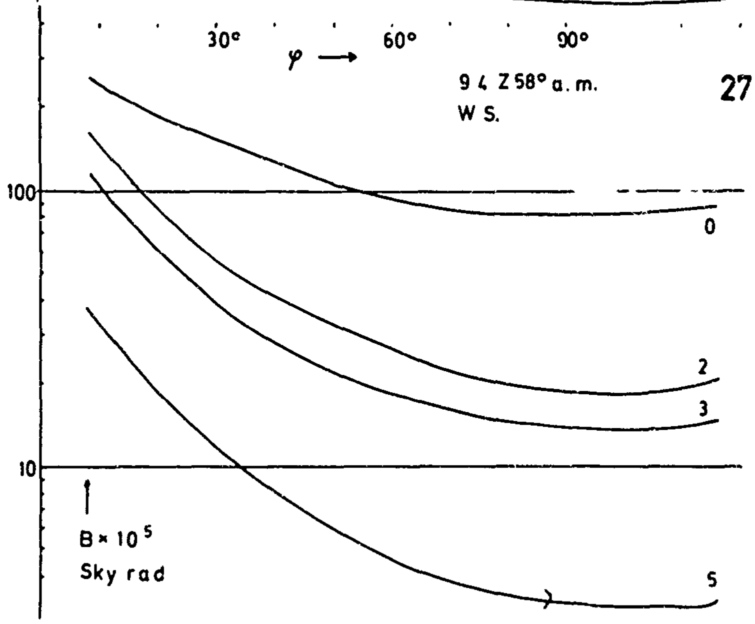
30°
φ →
60°
90°
9 4 Z 58° a. m.
W S.
100
10
0
2
3
5
B×10⁵
Sky rad

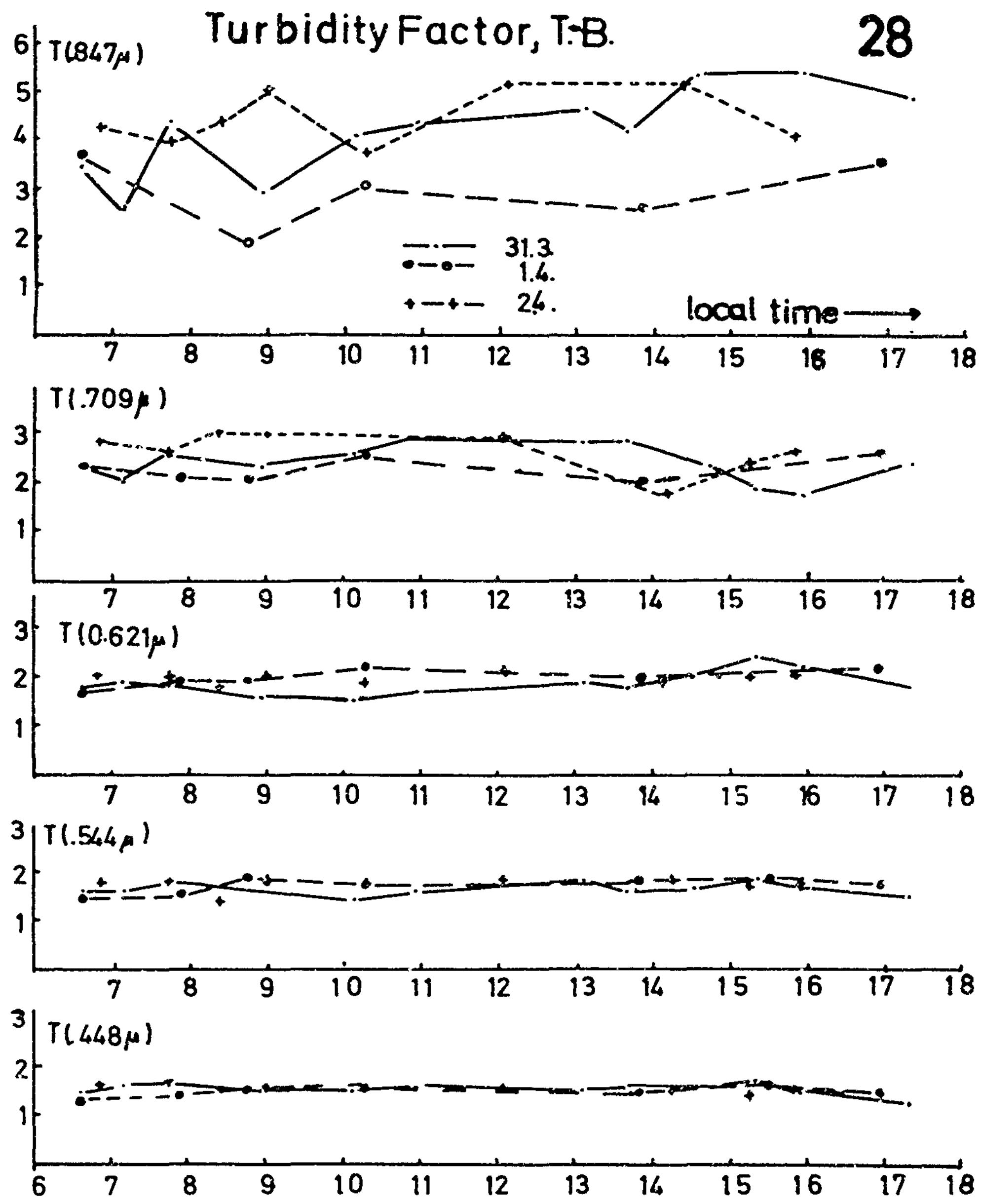

Turbidity Factor, T-B.
28
T(.847μ)
T(.709μ)
T(0.621μ)
T(.544μ)
T(.448μ)
31.3.
1.4.
2.4.
local time

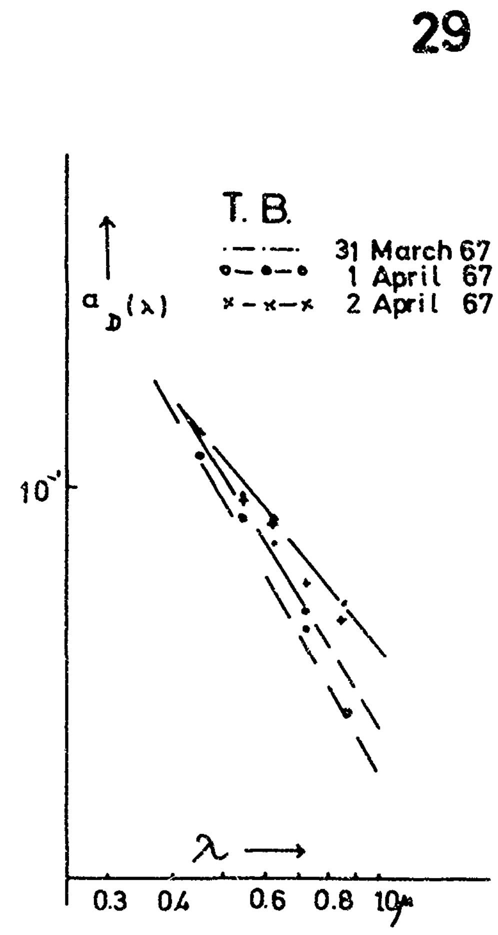

29
T. B.
31 March 67
1 April 67
2 April 67
$a_D(\lambda)$
10^{-1}
λ
0.3 0.4 0.6 0.8 1.0μ

28-29

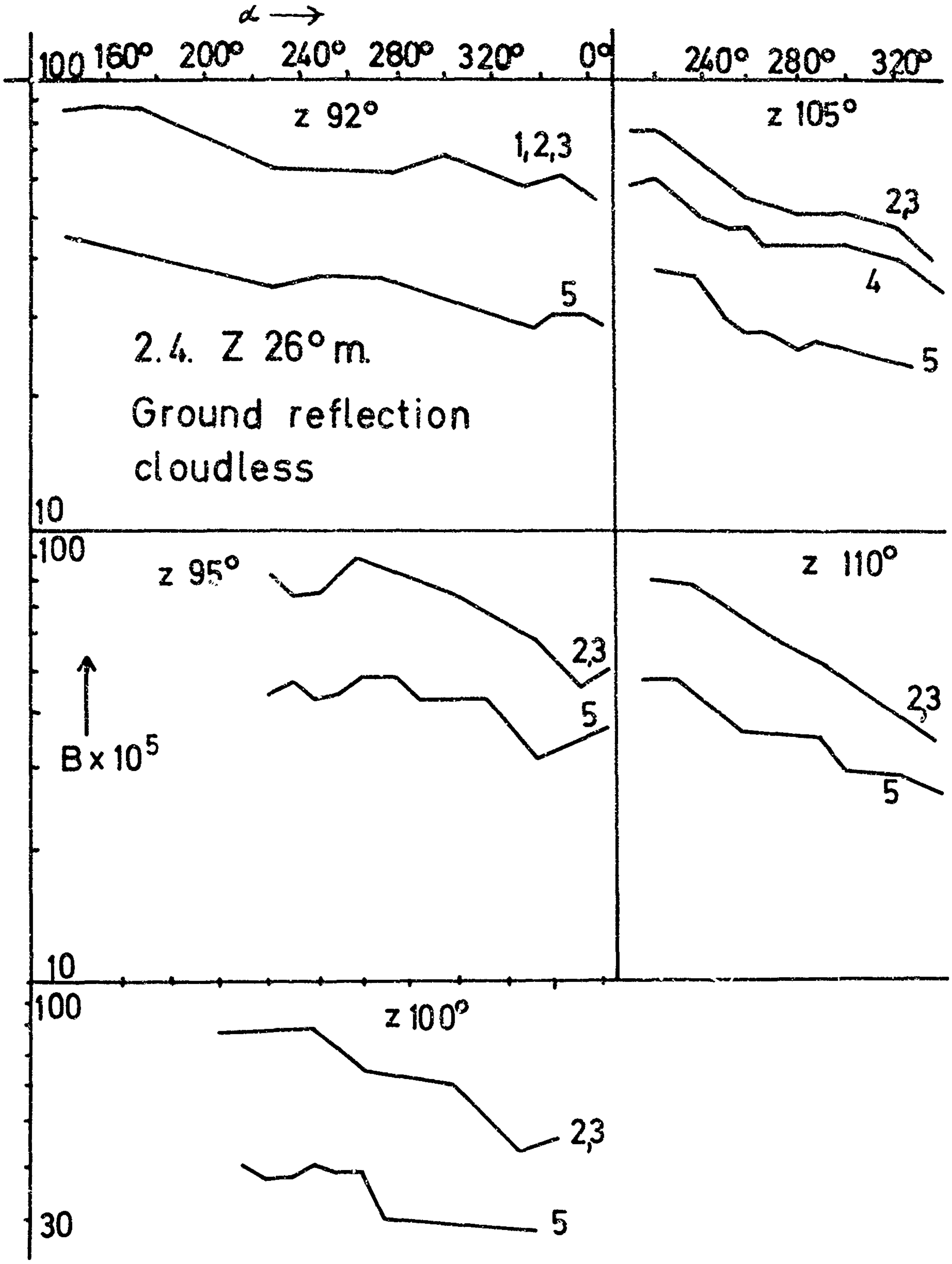

α →
100 160° 200° 240° 280° 320° 0°
240° 280° 320°
z 92°
1,2,3
5
2.4. Z 26° m.
Ground reflection
cloudless
10
z 105°
2,3
4
5
100
z 95°
2,3
5
B x 10⁵
10
z 110°
2,3
5
100
z 100°
2,3
5
30

2.4. Z 58°p.m. cloudless

Ground reflection

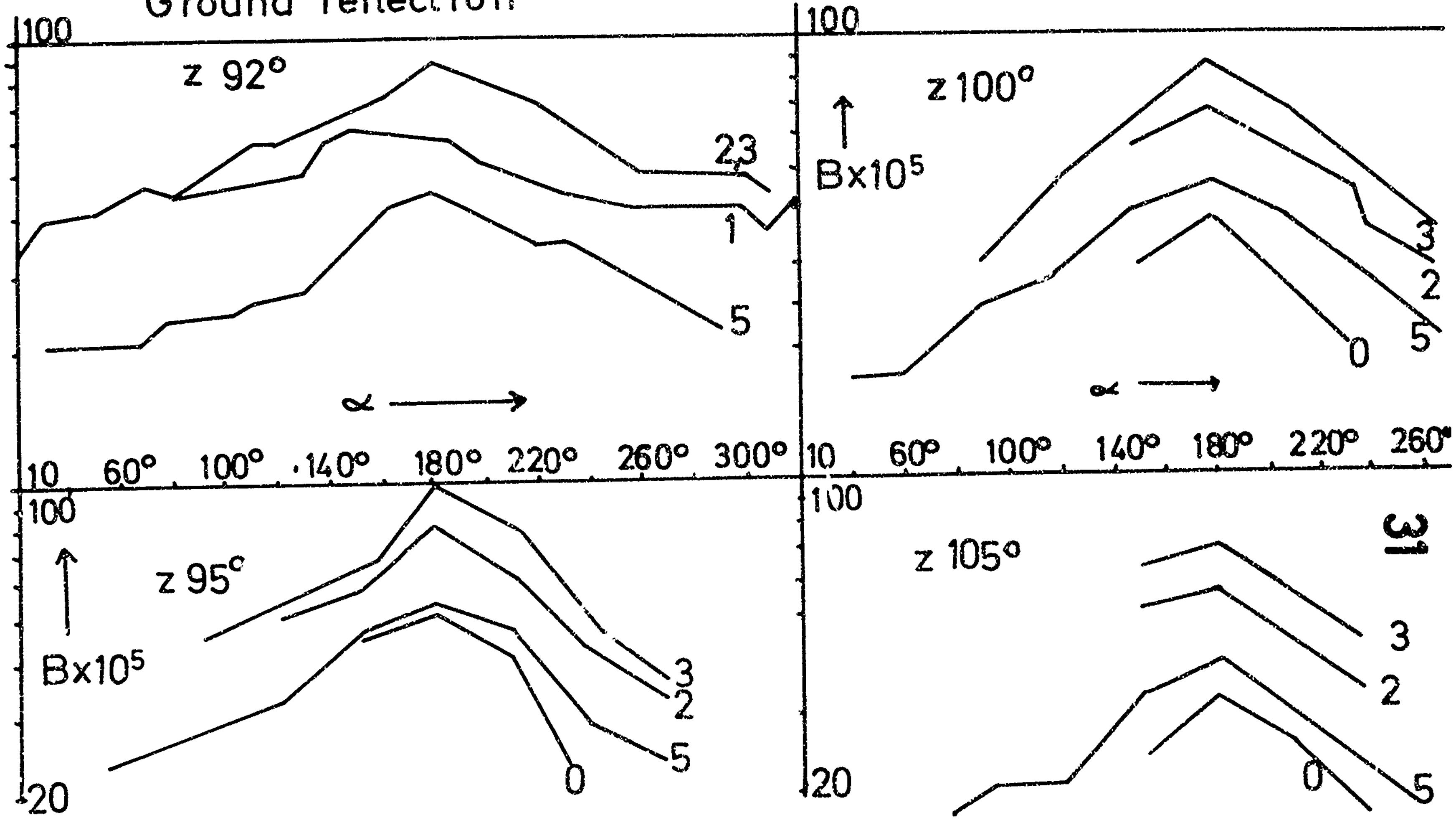

4.4. Z 66° a.m.

Ground reflection, cloudless

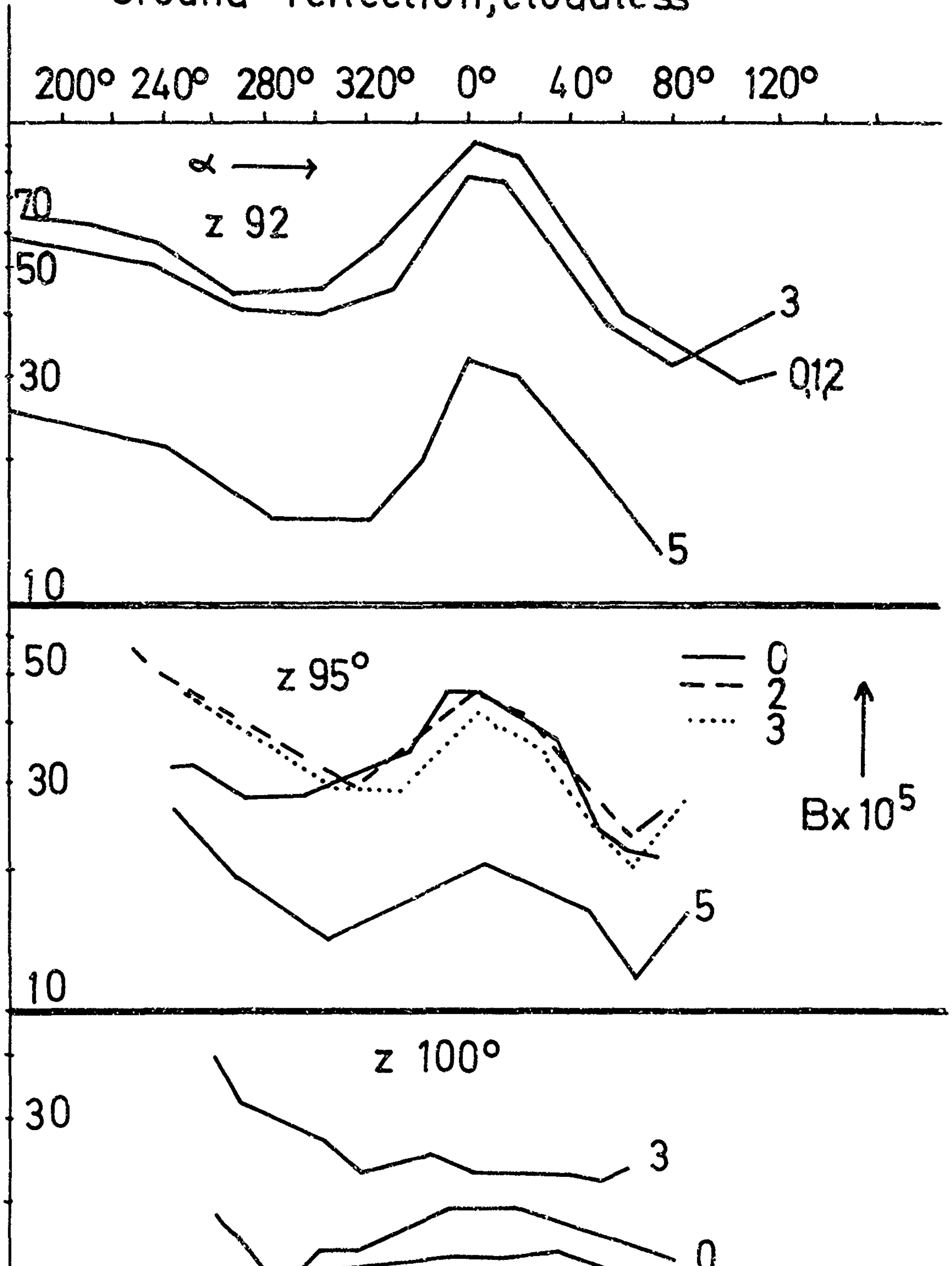

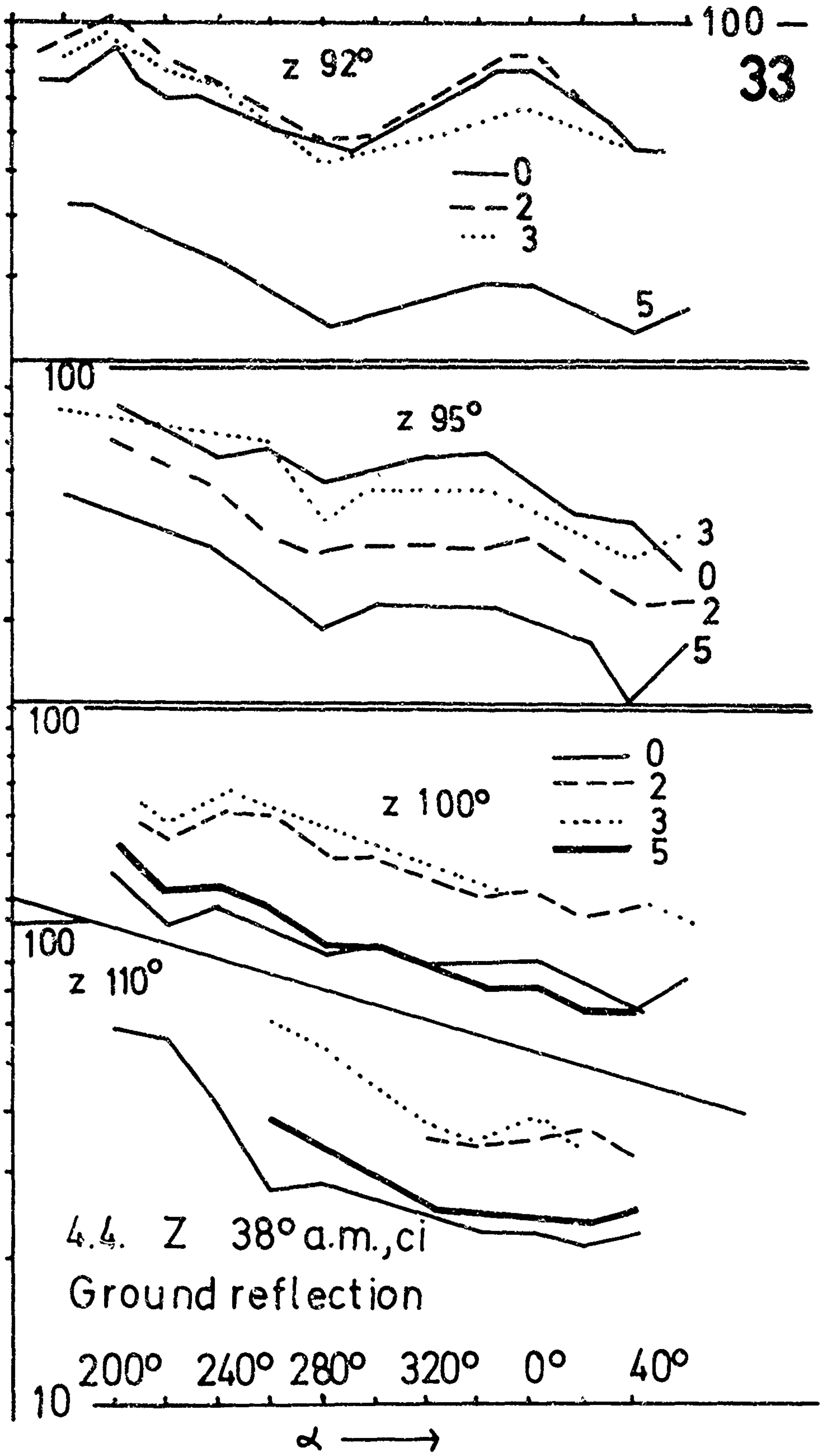

4.4. Z 38° a.m., ci
Ground reflection

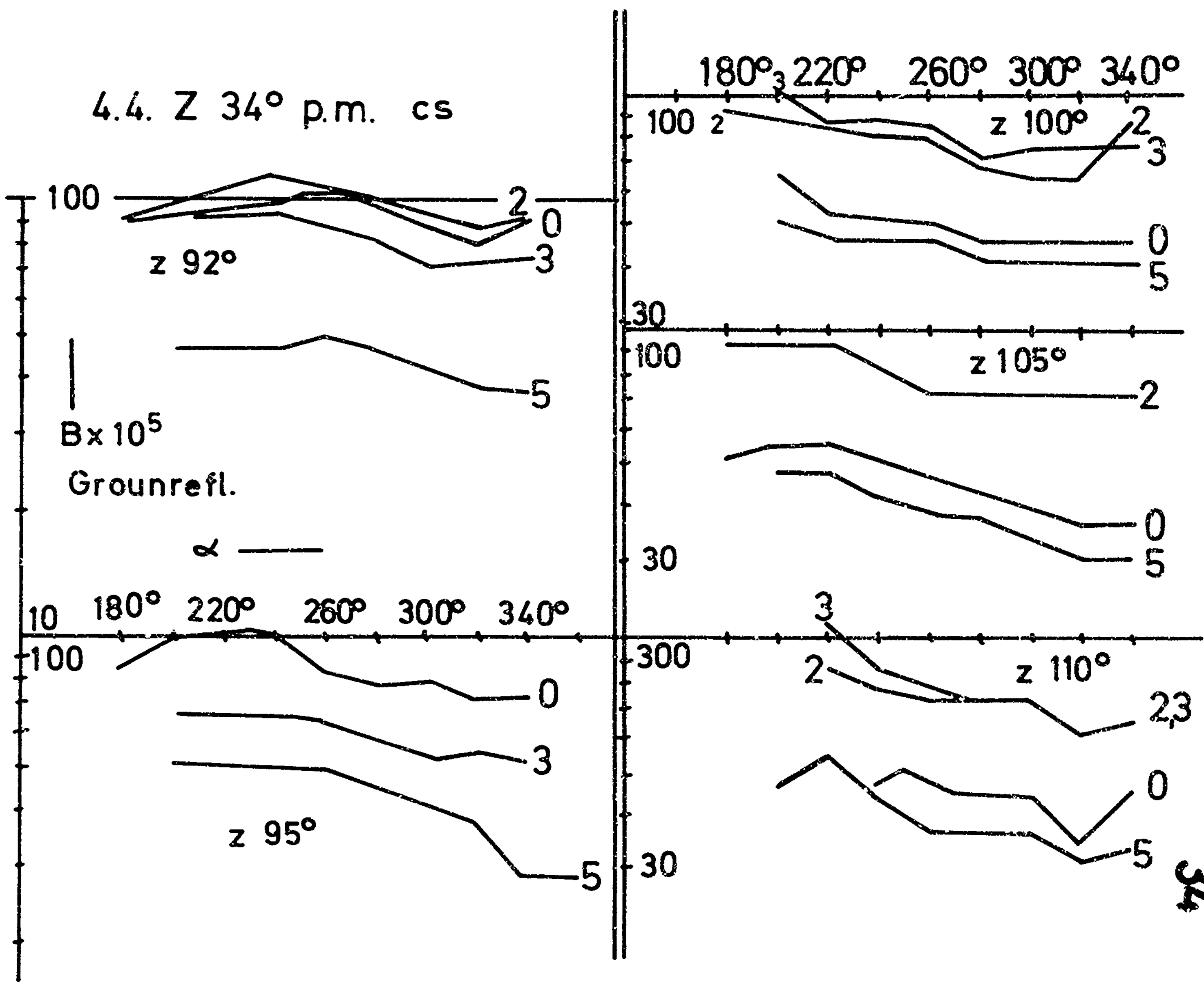
4.4. Z 34° p.m. cs
100
z 92°
2
0
3
5
B x 10^5
Grounrefl.
α
10
100
180°
220°
260°
300°
340°
z 95°
180°
220°
260°
300°
340°
100
z 100°
30
100
z 105°
30
300
z 110°
2,3
30

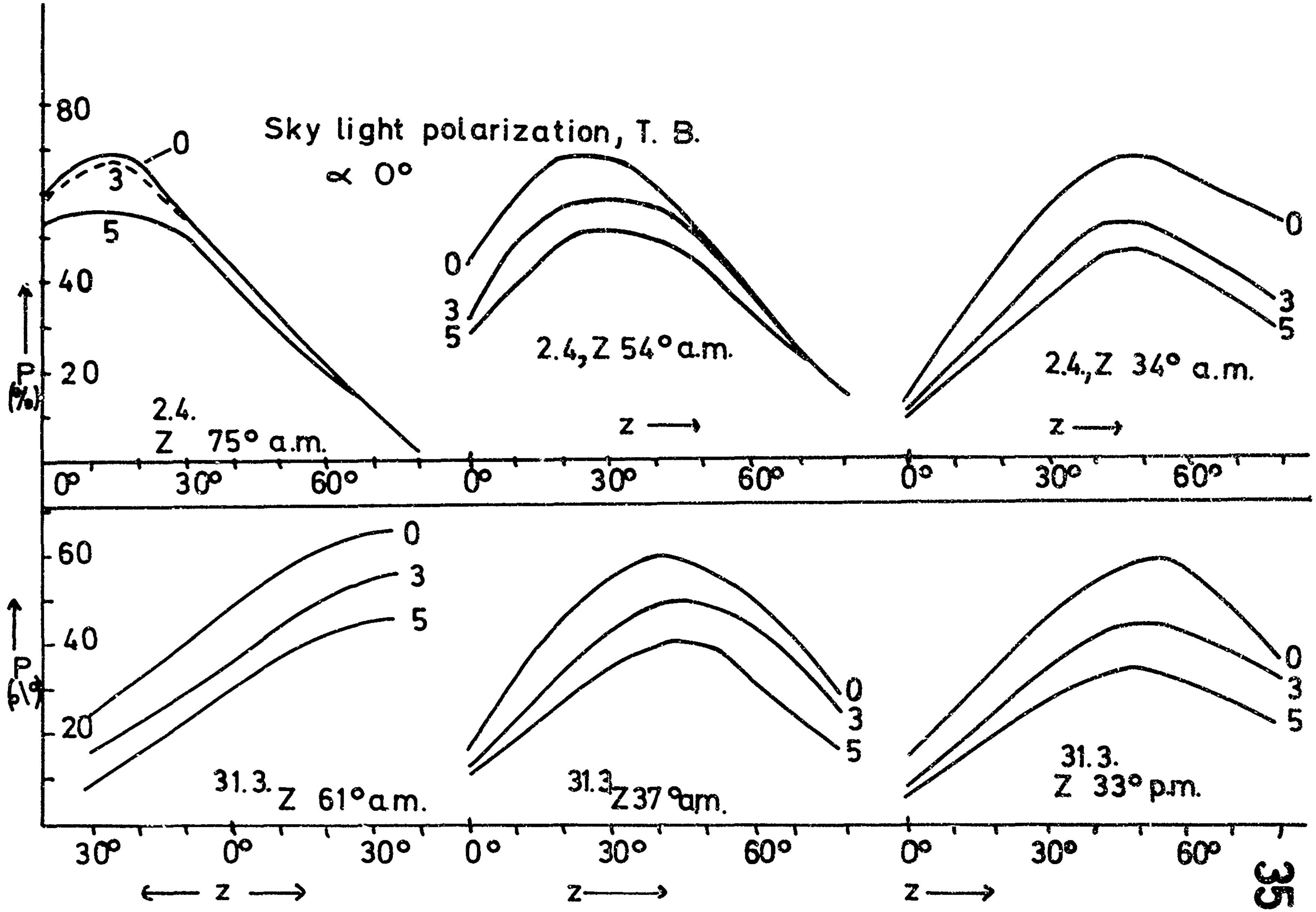
Sky light polarization, T. B.
α 0°
P (%)
80
40
20
60
2.4. Z 75° a.m.
2.4, Z 54° a.m.
2.4, Z 34° a.m.
31.3. Z 61° a.m.
31.3. Z 37° a.m.
31.3. Z 33° p.m.
0
3
5
0°
30°
60°
z →
← z →

35

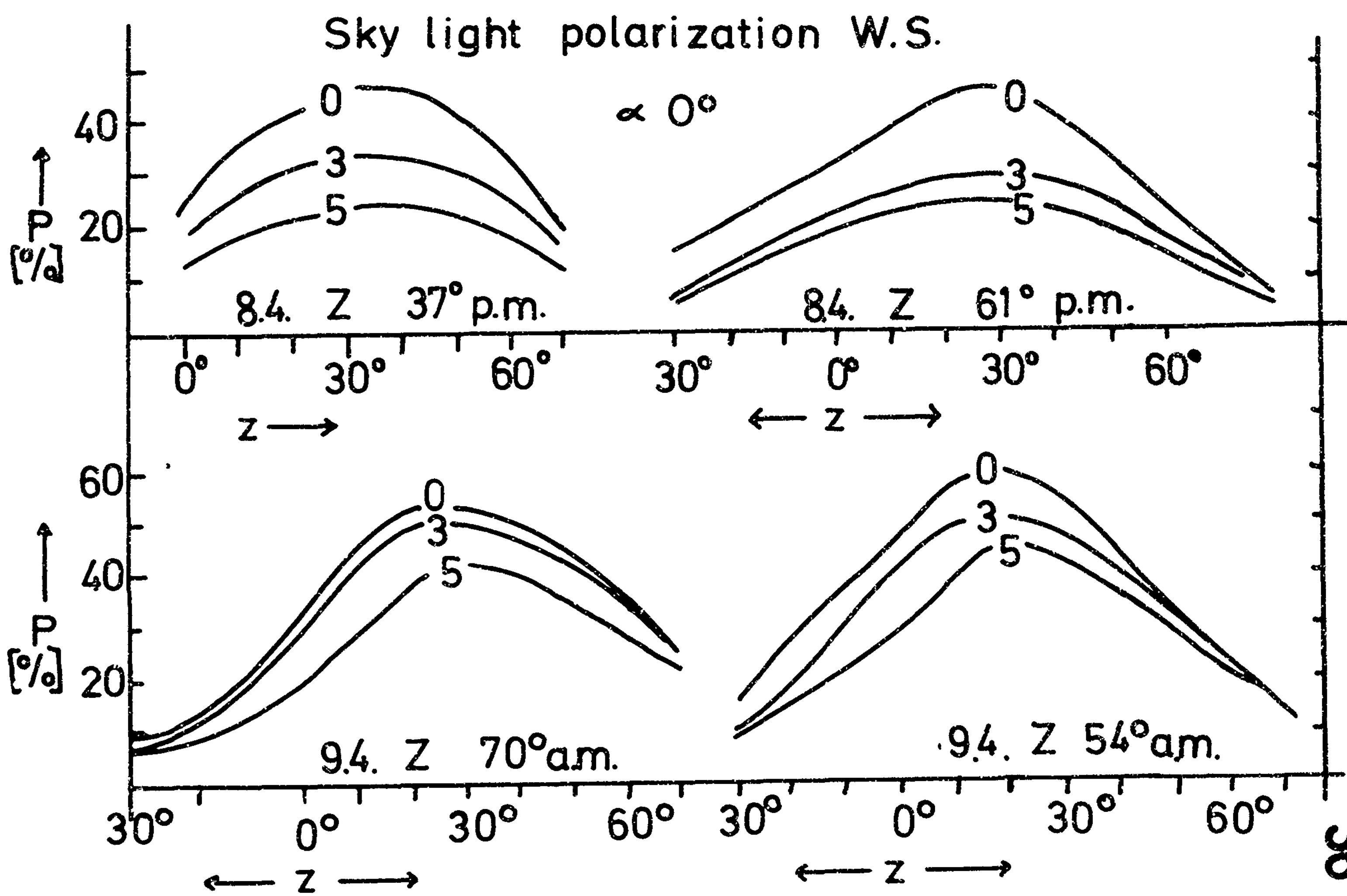
Sky light polarization W.S.
α 0°
P [%]
40
20
60
0
3
5
8.4. Z 37° p.m.
8.4. Z 61° p.m.
9.4. Z 70° a.m.
9.4. Z 54° a.m.
0°
30°
60°
z

36

37

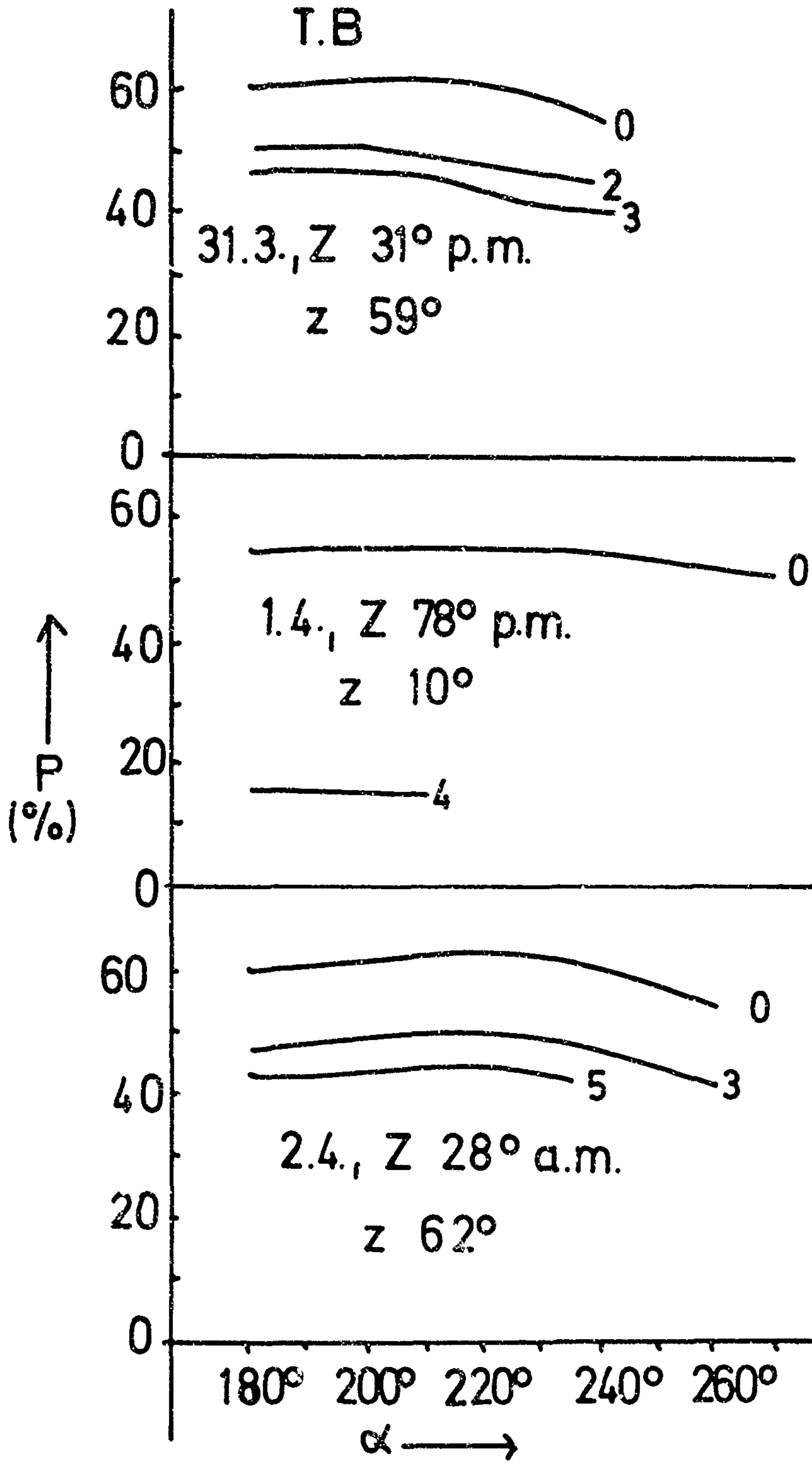

Sky light polarization, T.B.

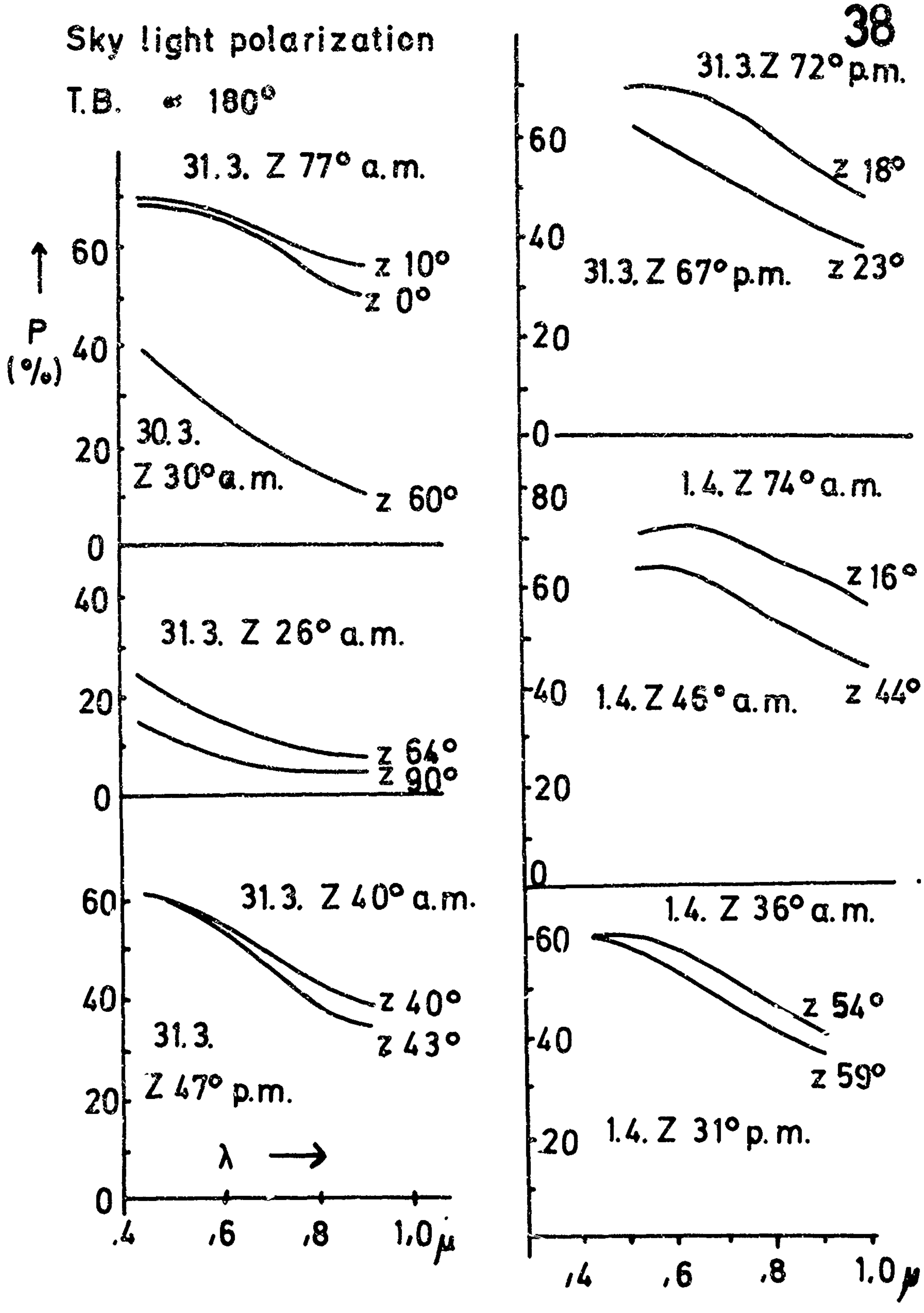
Sky light polarization
T.B. α 180°
31.3. Z 77° a.m.
P (%)
z 10°
z 0°
30.3.
Z 30° a.m.
z 60°
31.3. Z 26° a.m.
z 64°
z 90°
31.3. Z 40° a.m.
z 40°
z 43°
31.3.
Z 47° p.m.
λ
,4
,6
,8
1,0 μ
31.3. Z 72° p.m.
z 18°
31.3. Z 67° p.m.
z 23°
1.4. Z 74° a.m.
z 16°
1.4. Z 45° a.m.
z 44°
1.4. Z 36° a.m.
z 54°
z 59°
1.4. Z 31° p.m.

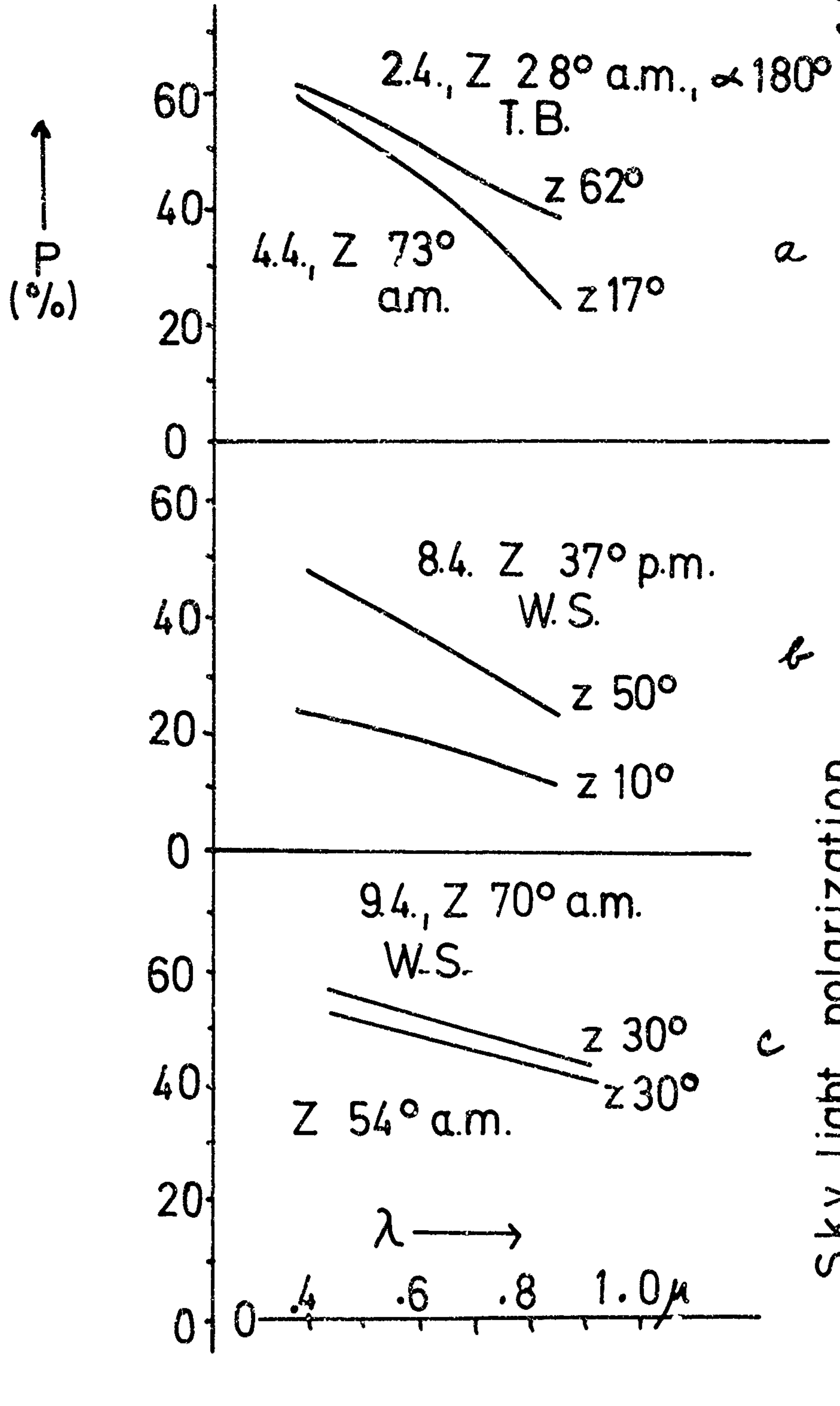

Sky light polarization.

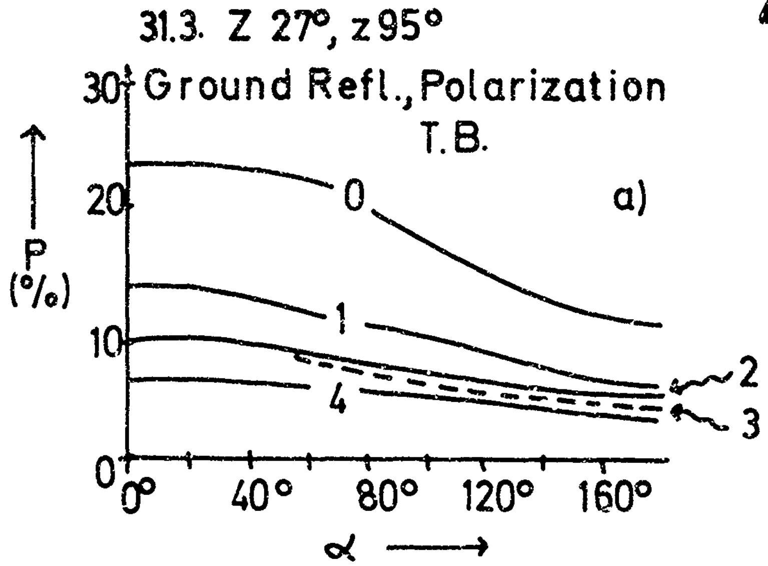
31.3. Z 27°, z 95°
Ground Refl., Polarization
T.B.
a)
P (%)
30
20
10
0
0
1
2
3
4
0°
40°
80°
120°
160°
α

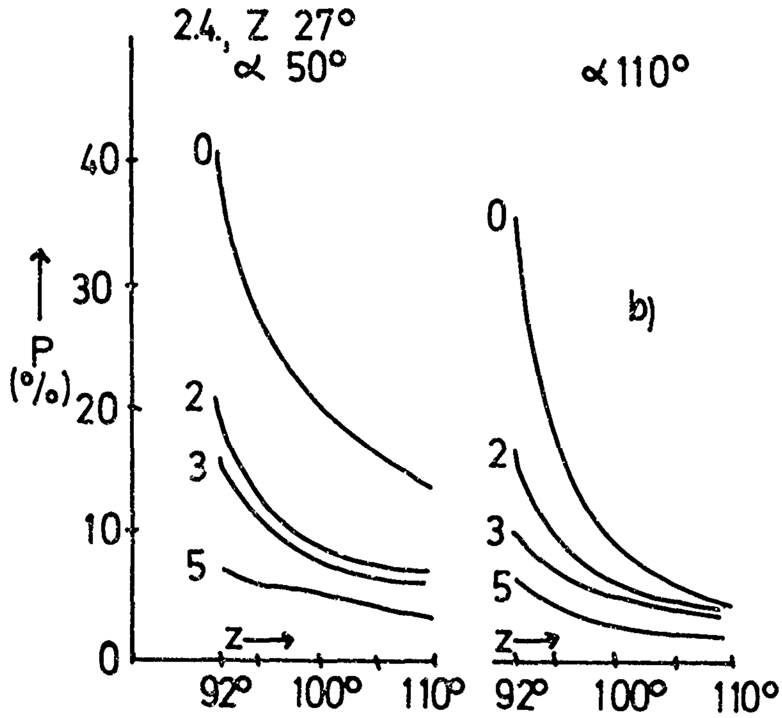
2.4., Z 27°
α 50°
α 110°
b)
P (%)
40
30
20
10
0
0
2
3
5
z
92°
100°
110°

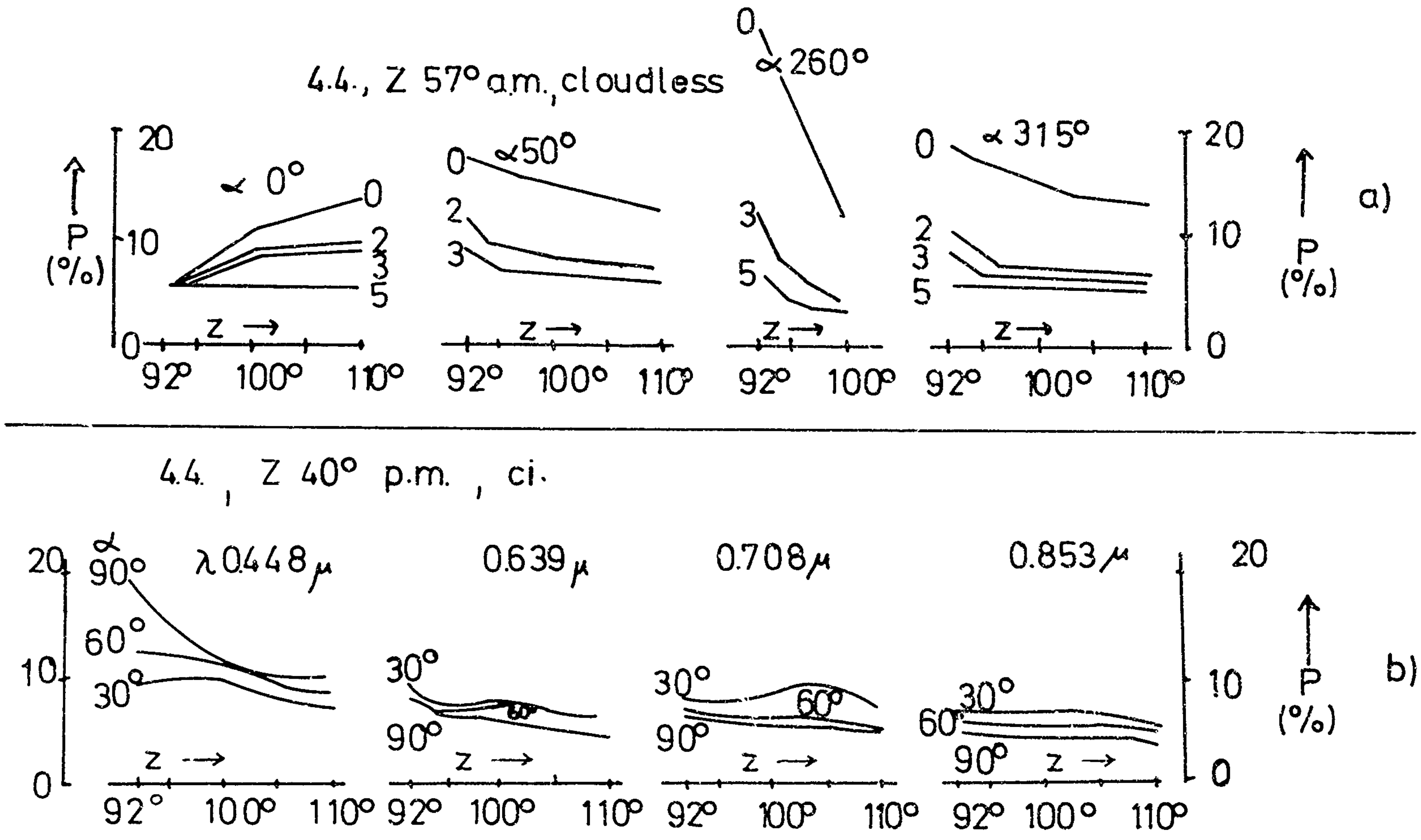

Ground reflection, polarization. T. B.

42

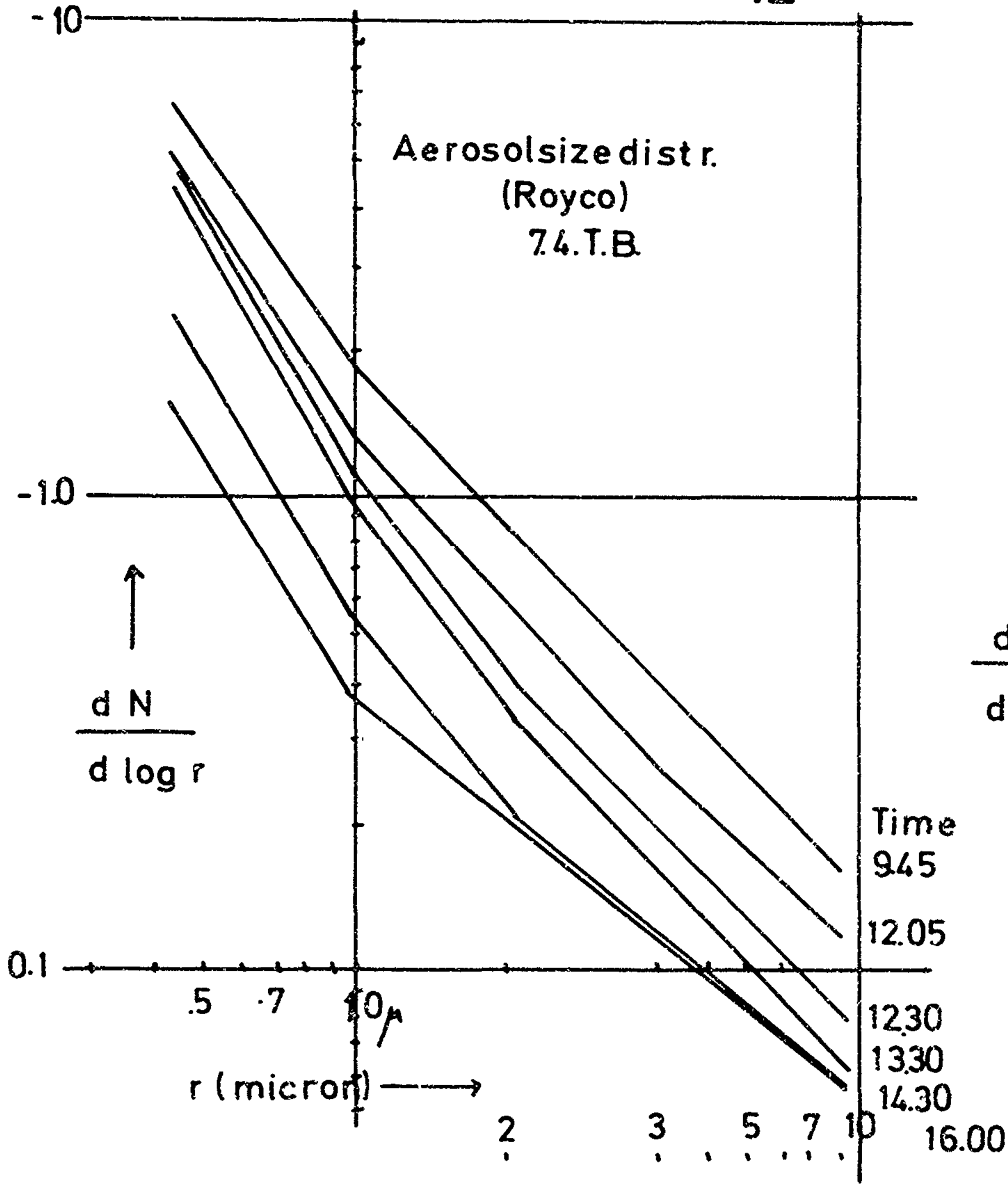

Aerosolsizedistr.
(Royco)
7.4.T.B.
-10
-1.0
0.1
d N / d log r
.5
·7
10μ
2
3
5
7
10
r (micron)
Time
9.45
12.05
12.30
13.30
14.30
16.00

43

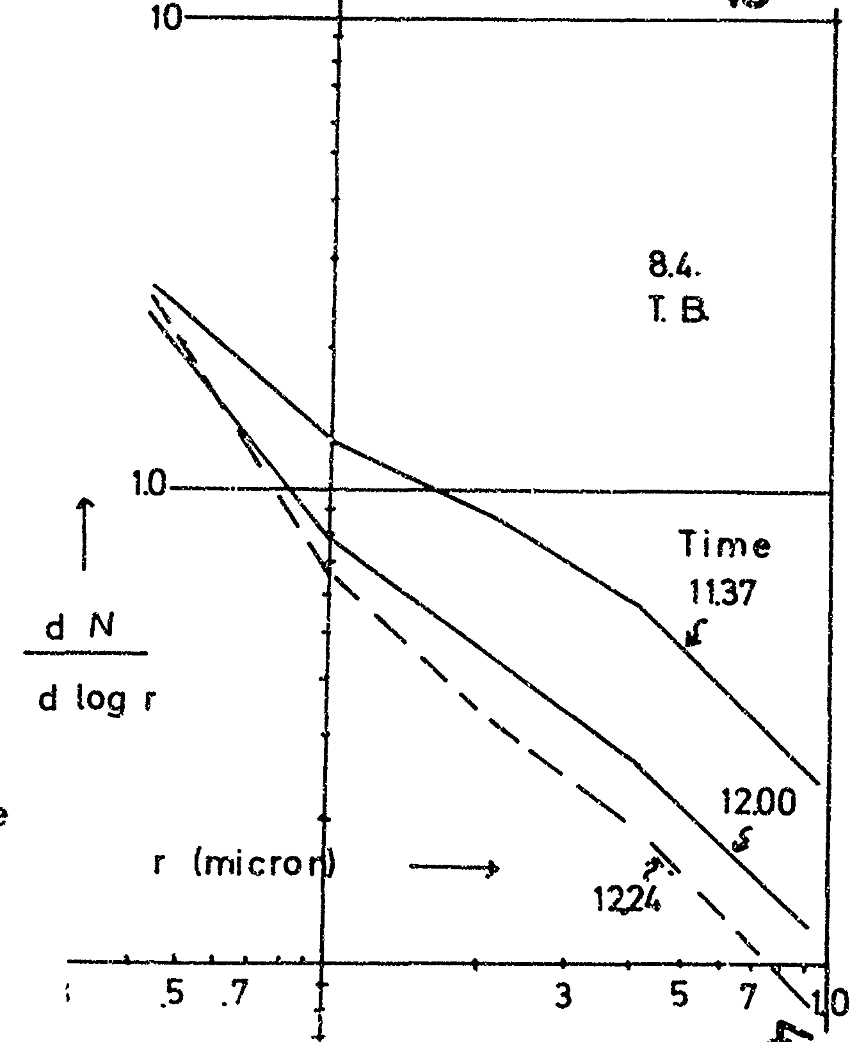

8.4.
T. B.
10
1.0
d N / d log r
Time
11.37
12.00
12.24
r (micron)
.5
.7
3
5
7
10

42-43

Aitken Nuclei Number

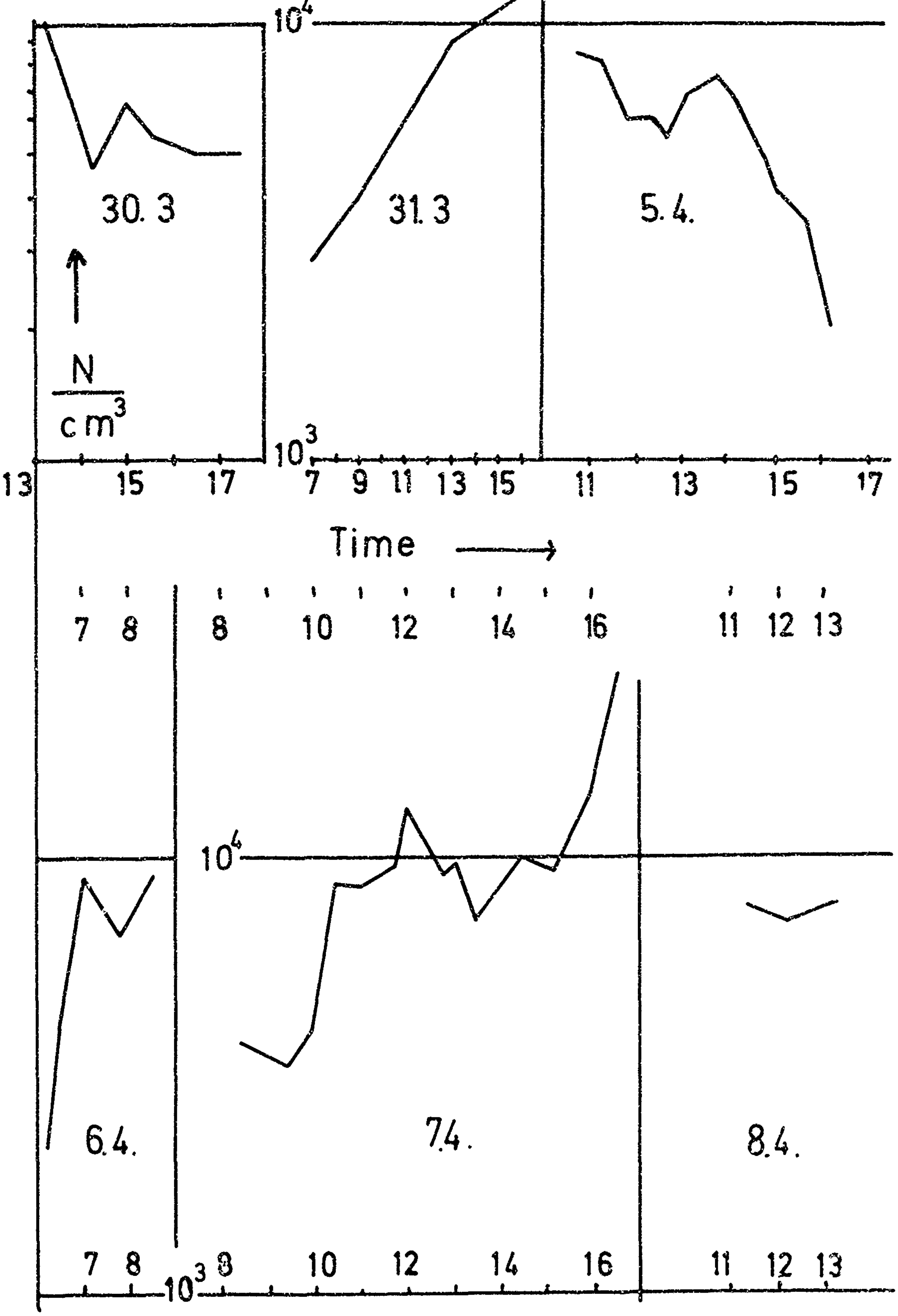

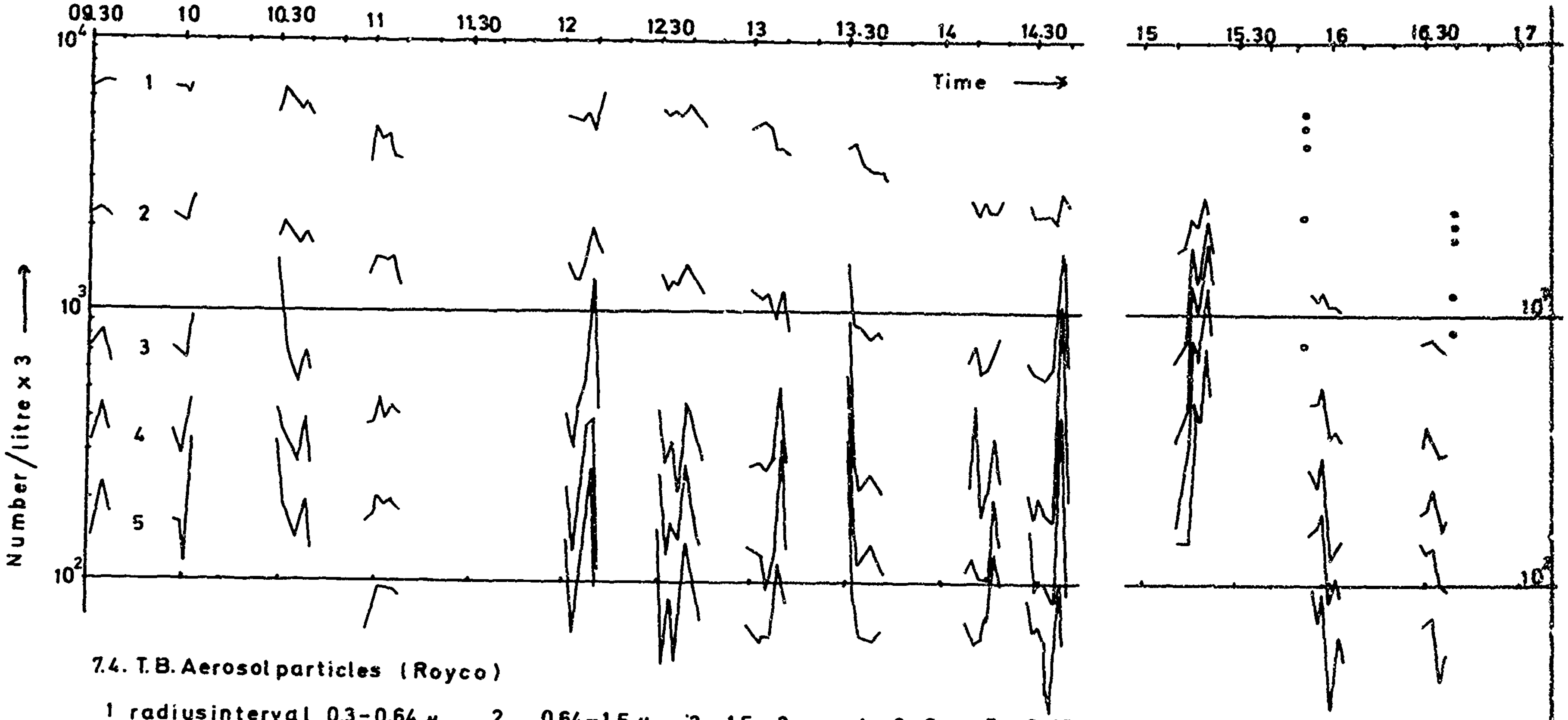

7.4. T.B. Aerosol particles (Royco)

1 radiusinterval 0,3–0,64 μ, 2 0,64–1,5 μ, 3 1,5–3 μ, 4 3–6 μ, 5 6–15 μ

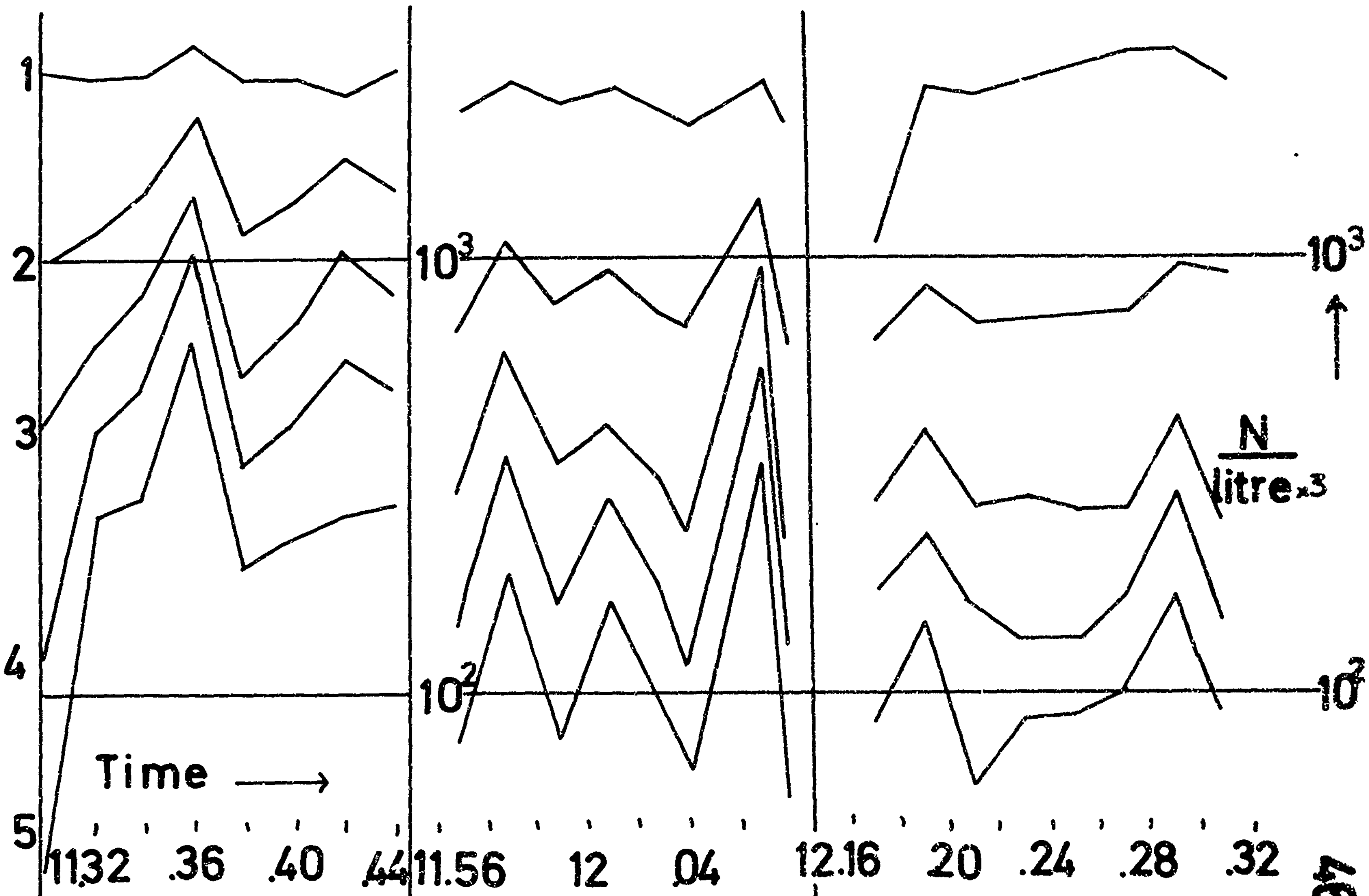

8.4. T.B. aerosolparticles

46

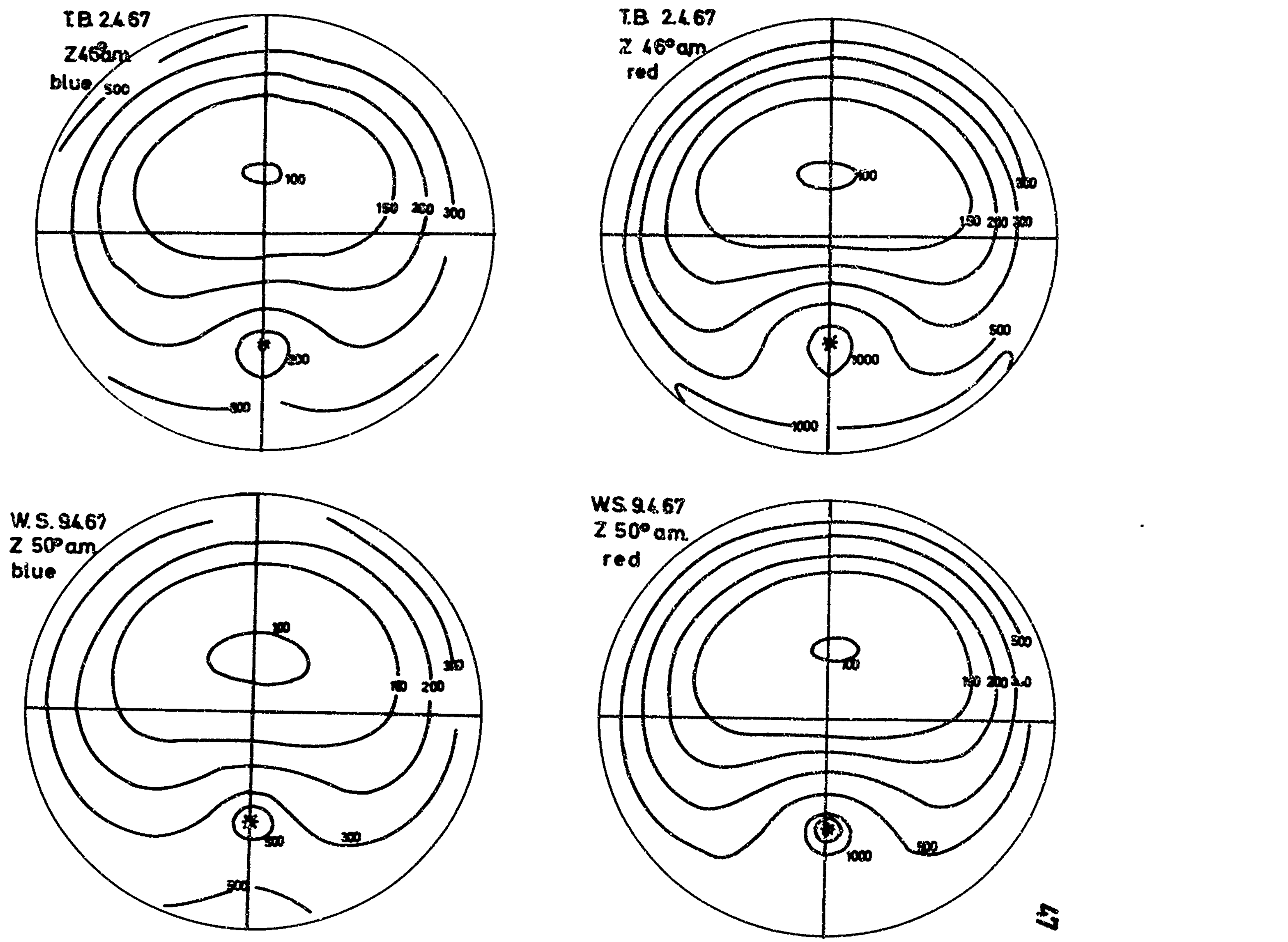
T.B 2.4.67
Z 46° am
blue
T.B 2.4.67
Z 46° am
red
W.S. 9.4.67
Z 50° am
blue
W.S. 9.4.67
Z 50° am.
red
100
150
200
300
500
1000

W.S. 8.4.67
Z 64° p.m.
red

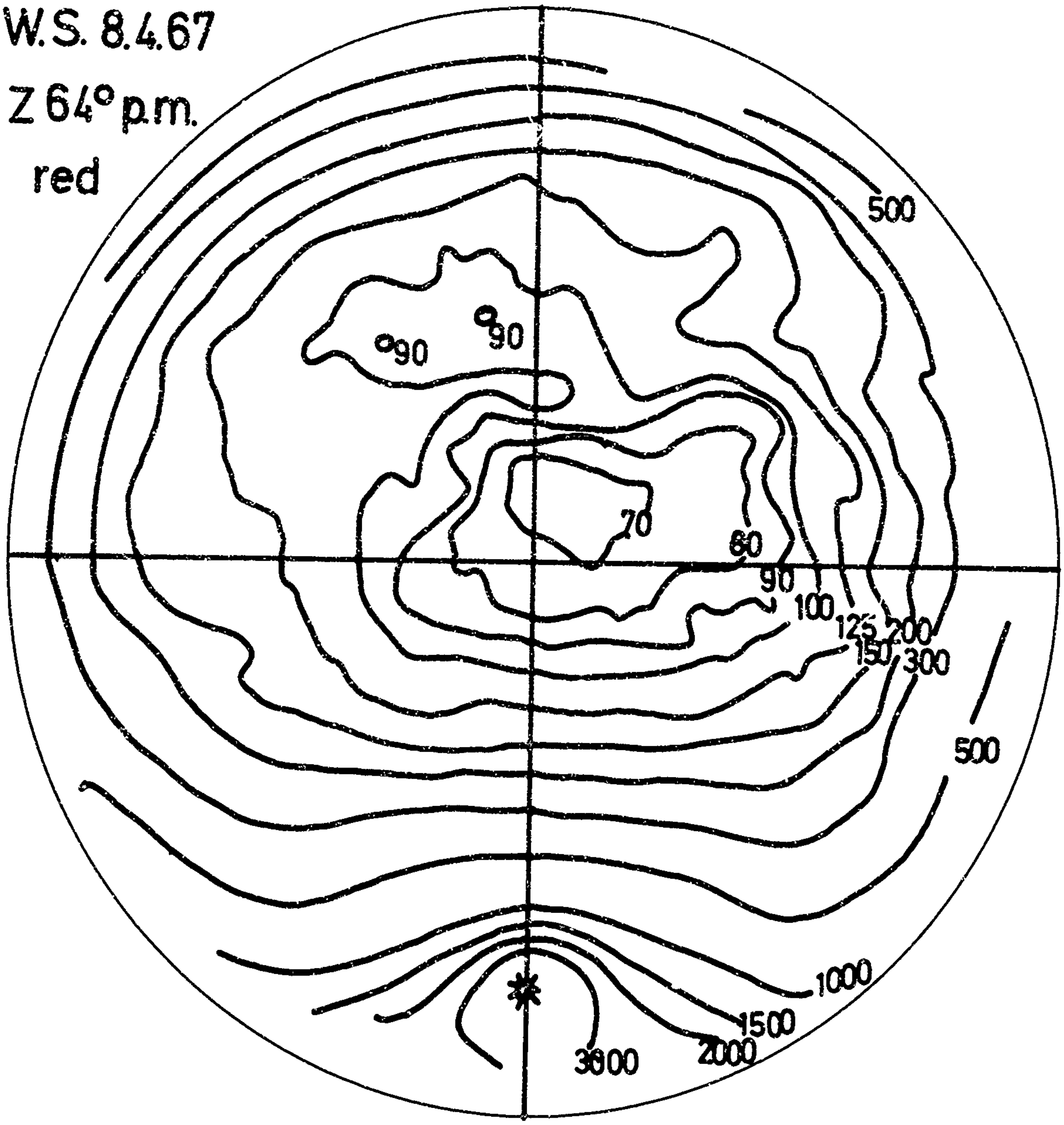

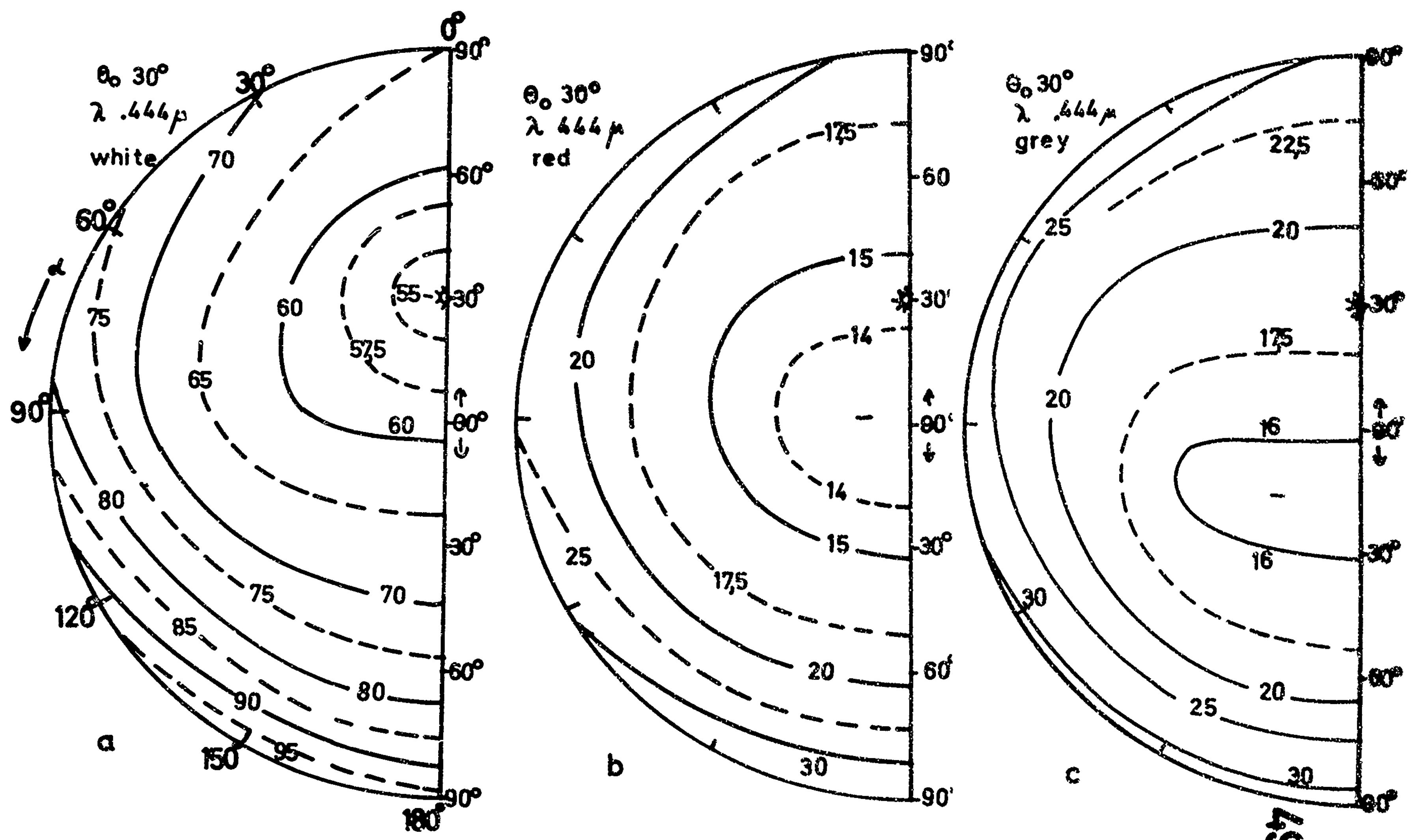

θo 30°
λ .444 μ
white
a
θo 30°
λ .444 μ
red
b
θo 30°
λ .444 μ
grey
c

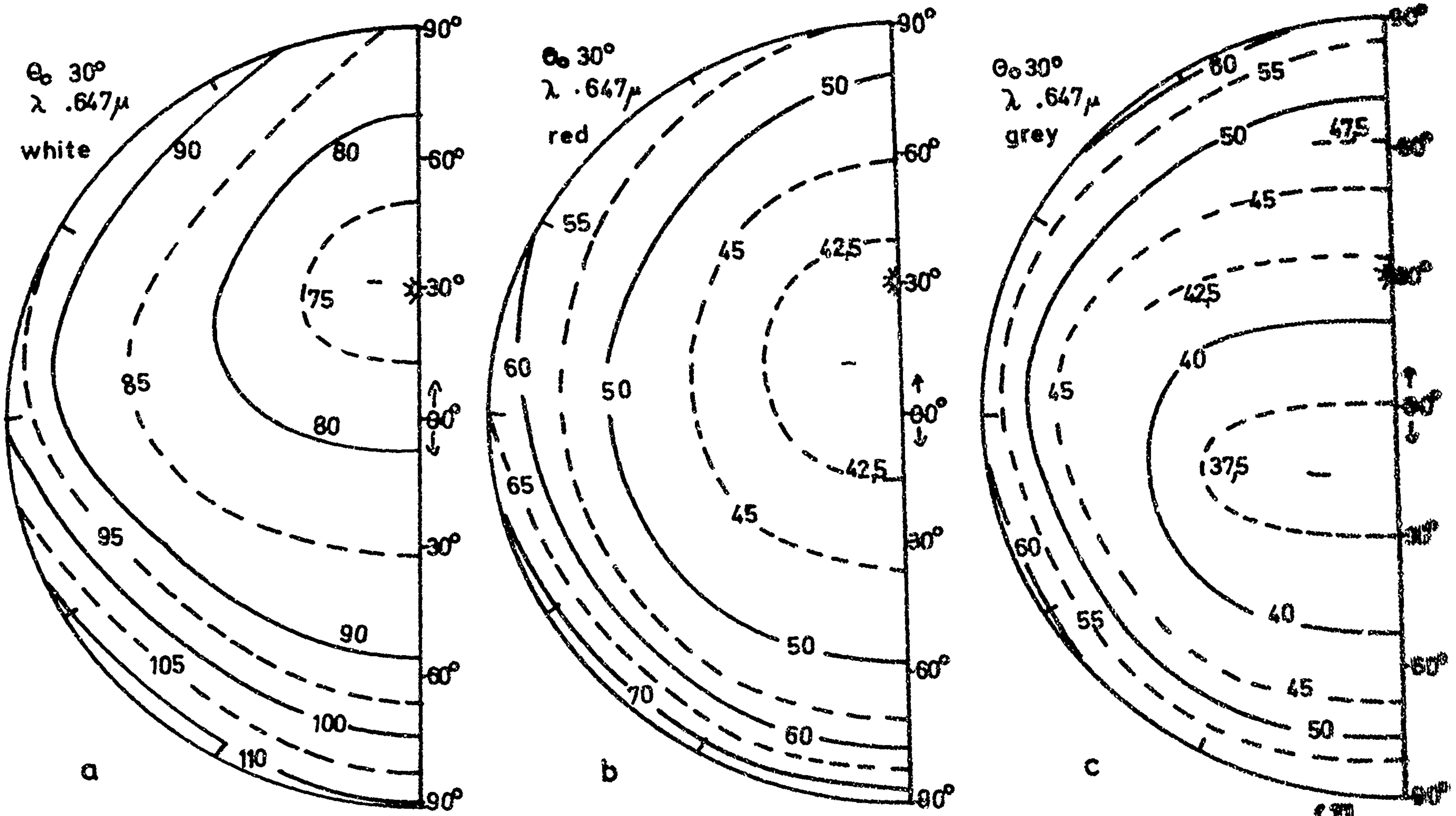
θ_0 30°
λ .647 μ
white
a
θ_0 30°
λ .647 μ
red
b
θ_0 30°
λ .647 μ
grey
c

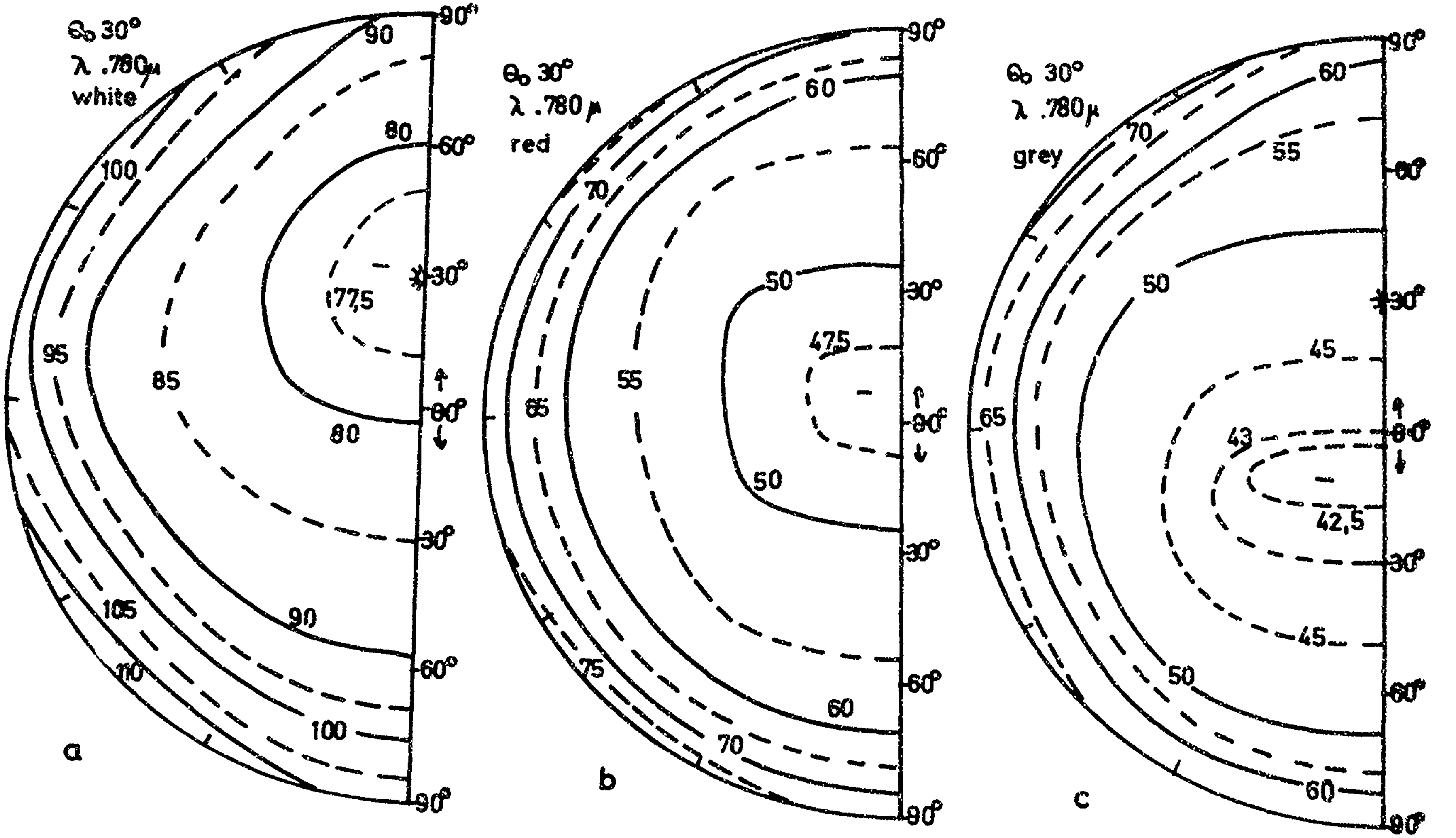

Θo 30°
λ .780μ
white
a
Θo 30°
λ .780μ
red
b
Θo 30°
λ .780μ
grey
c

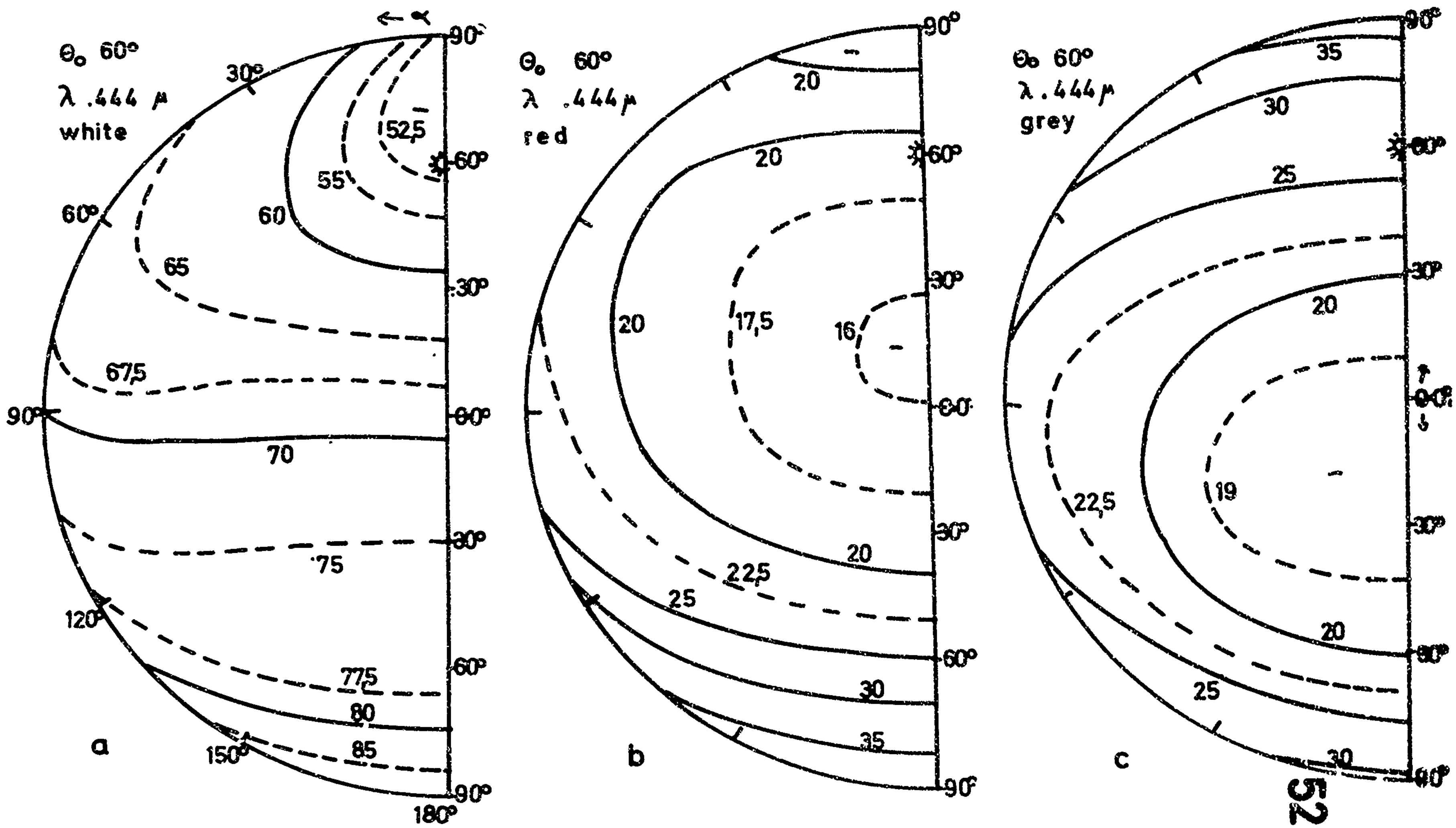

Θo 60°
λ .444 μ
white
Θo 60°
λ .444 μ
red
Θo 60°
λ .444 μ
grey
α
90°
60°
30°
0°
30°
60°
90°
180°
150°
120°
90°
60°
30°
52,5
55
60
65
67,5
70
75
77,5
80
85
20
17,5
16
22,5
25
30
35
19
a
b
c

52

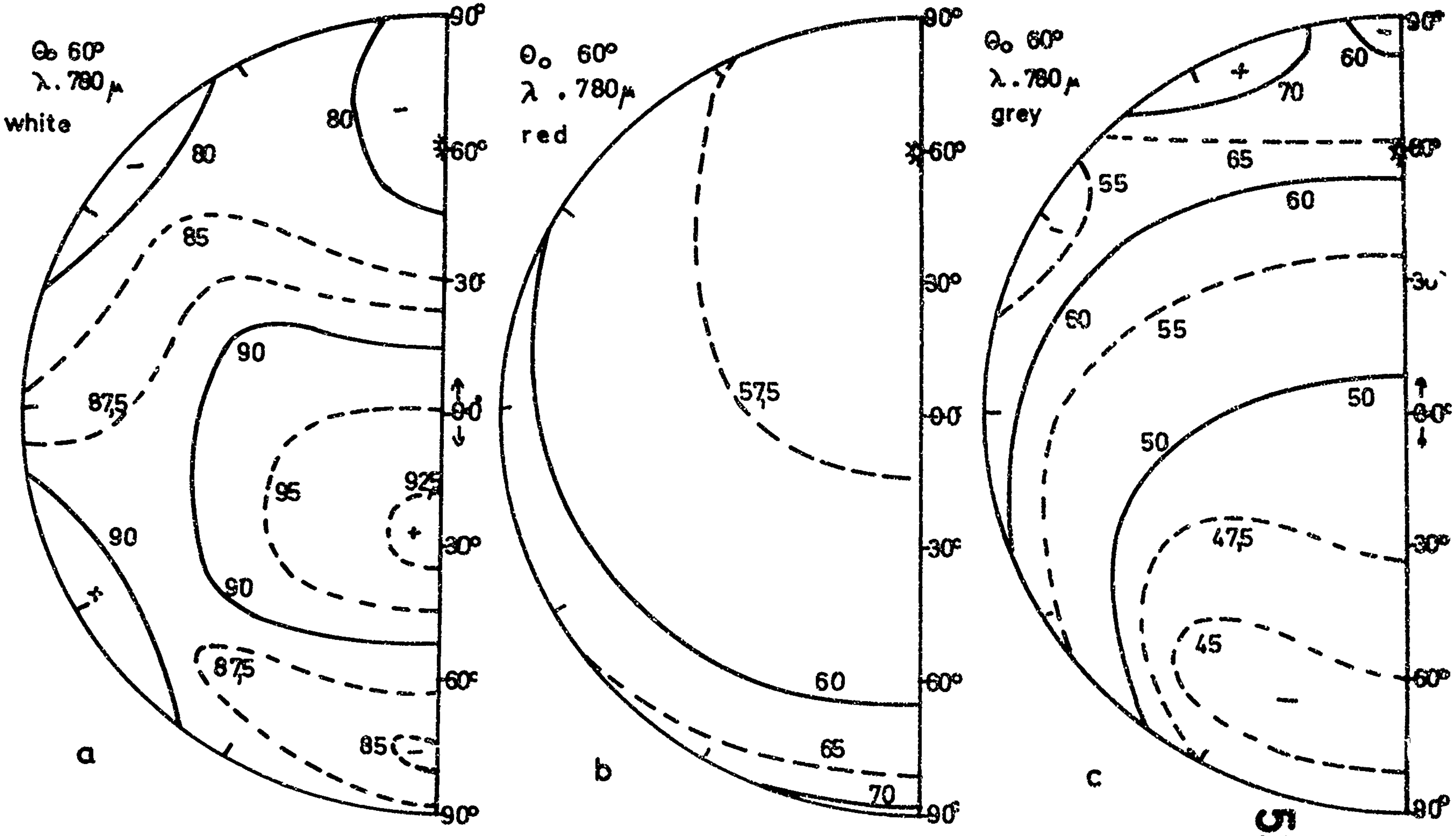
Θo 60°
λ . 780 μ
white
Θo 60°
λ . 780 μ
red
Θo 60°
λ . 780 μ
grey
a
b
c

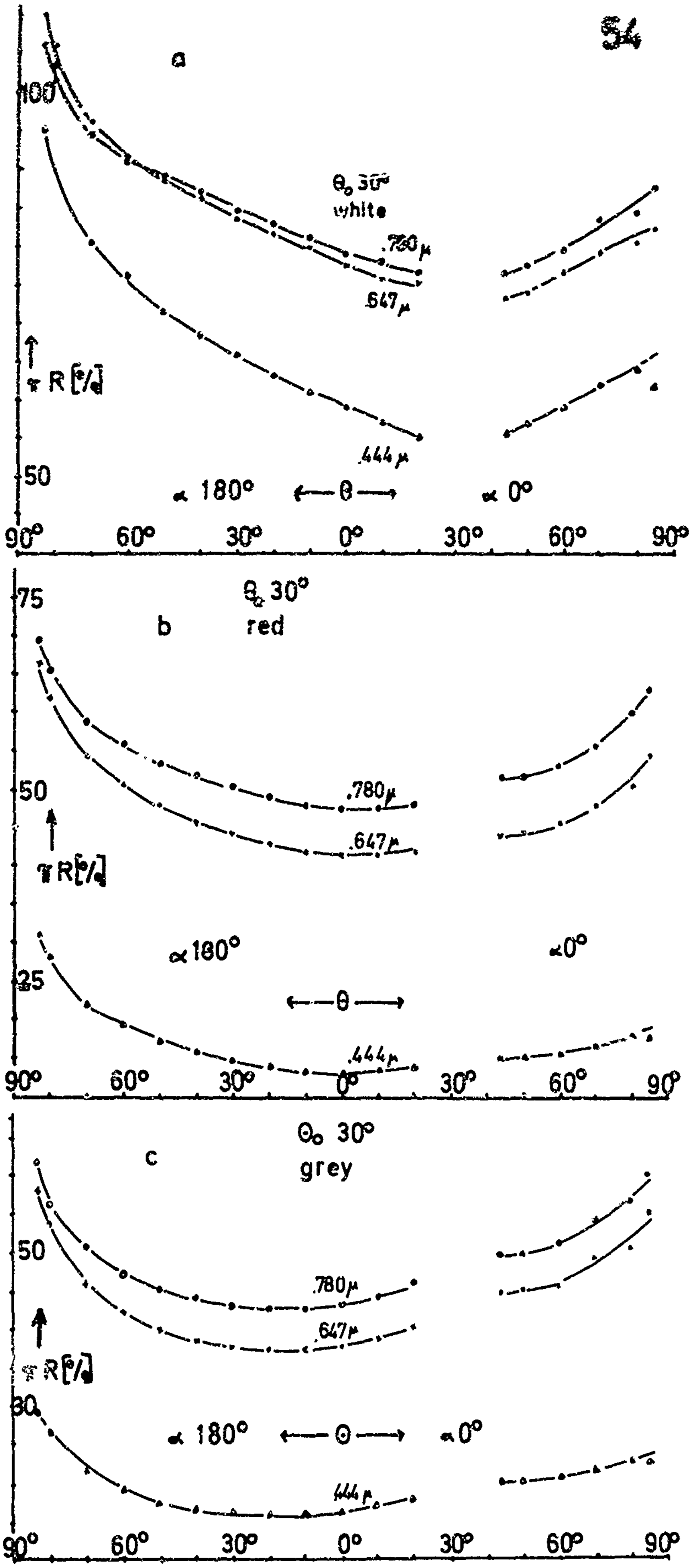
a
100
50
θo 30°
white
.780 μ
.647 μ
.444 μ
↑ π R [%]
α 180°
← θ →
α 0°
90° 60° 30° 0° 30° 60° 90°
b
θo 30°
red
75
50
25
.780 μ
.647 μ
.444 μ
↑ π R [%]
α 180°
← θ →
α 0°
90° 60° 30° 0° 30° 60° 90°
c
θo 30°
grey
50
30
.780 μ
.647 μ
.444 μ
↑ π R [%]
α 180°
← θ →
α 0°
90° 60° 30° 0° 30° 60° 90°

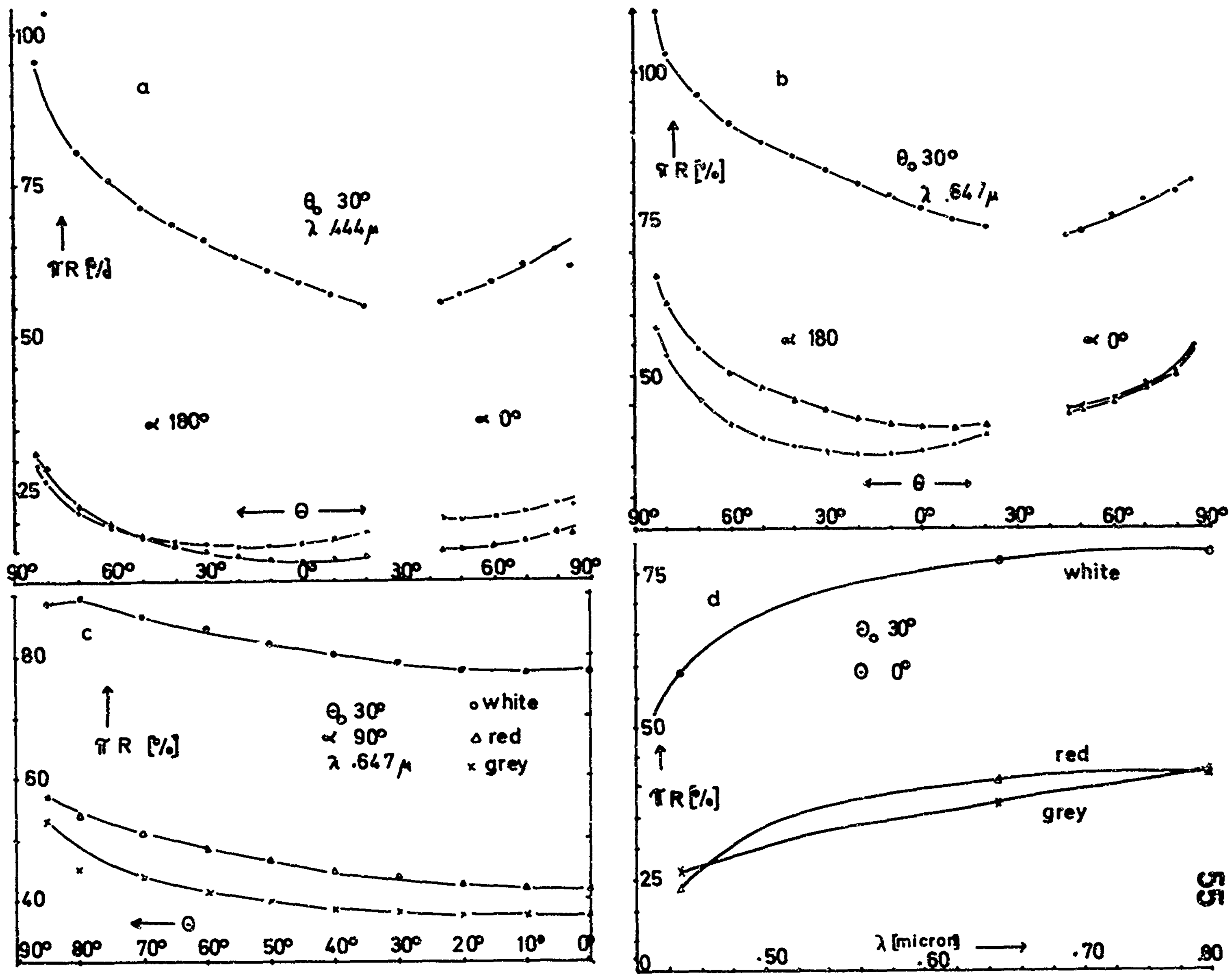
a
θ_o 30°
λ .444 μ
πR [%]
α 180°
α 0°
Θ
b
θ_o 30°
λ .647 μ
πR [%]
α 180
α 0°
θ
c
θ_o 30°
α 90°
λ .647 μ
o white
Δ red
x grey
πR [%]
Θ
d
Θ_o 30°
Θ 0°
white
red
grey
πR [%]
λ [micron]

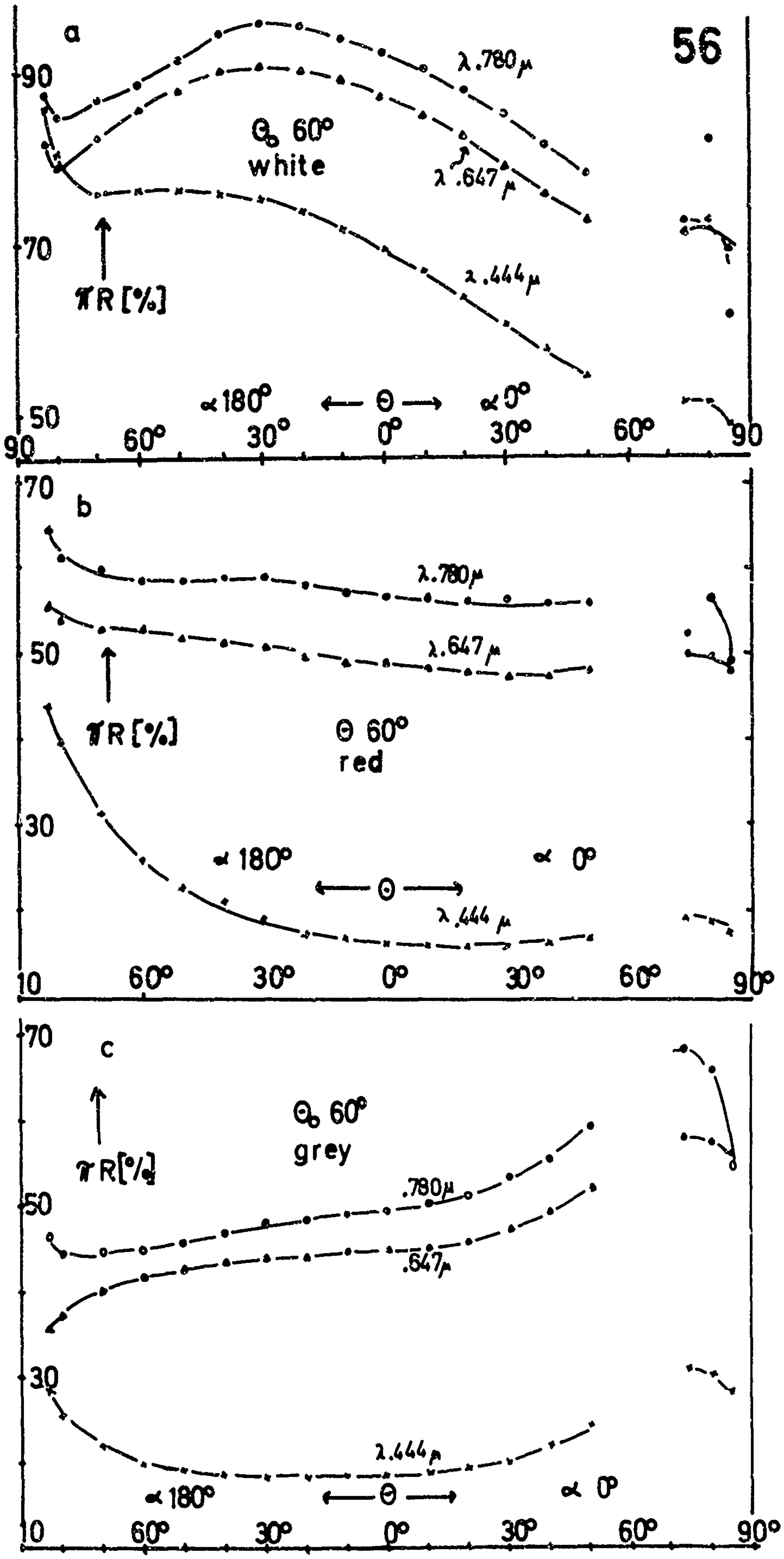
a
90
70
50
λ .780 μ
λ .647 μ
λ .444 μ
Θ₀ 60°
white
πR [%]
α 180°
← Θ →
α 0°
90
60°
30°
0°
30°
60°
90
b
70
50
30
10
λ .780 μ
λ .647 μ
λ .444 μ
πR [%]
Θ 60°
red
α 180°
← Θ →
α 0°
60°
30°
0°
30°
60°
90°
c
70
50
30
10
πR [%]
Θ₀ 60°
grey
.780 μ
.647 μ
λ .444 μ
α 180°
← Θ →
α 0°
60°
30°
0°
30°
60°
90°

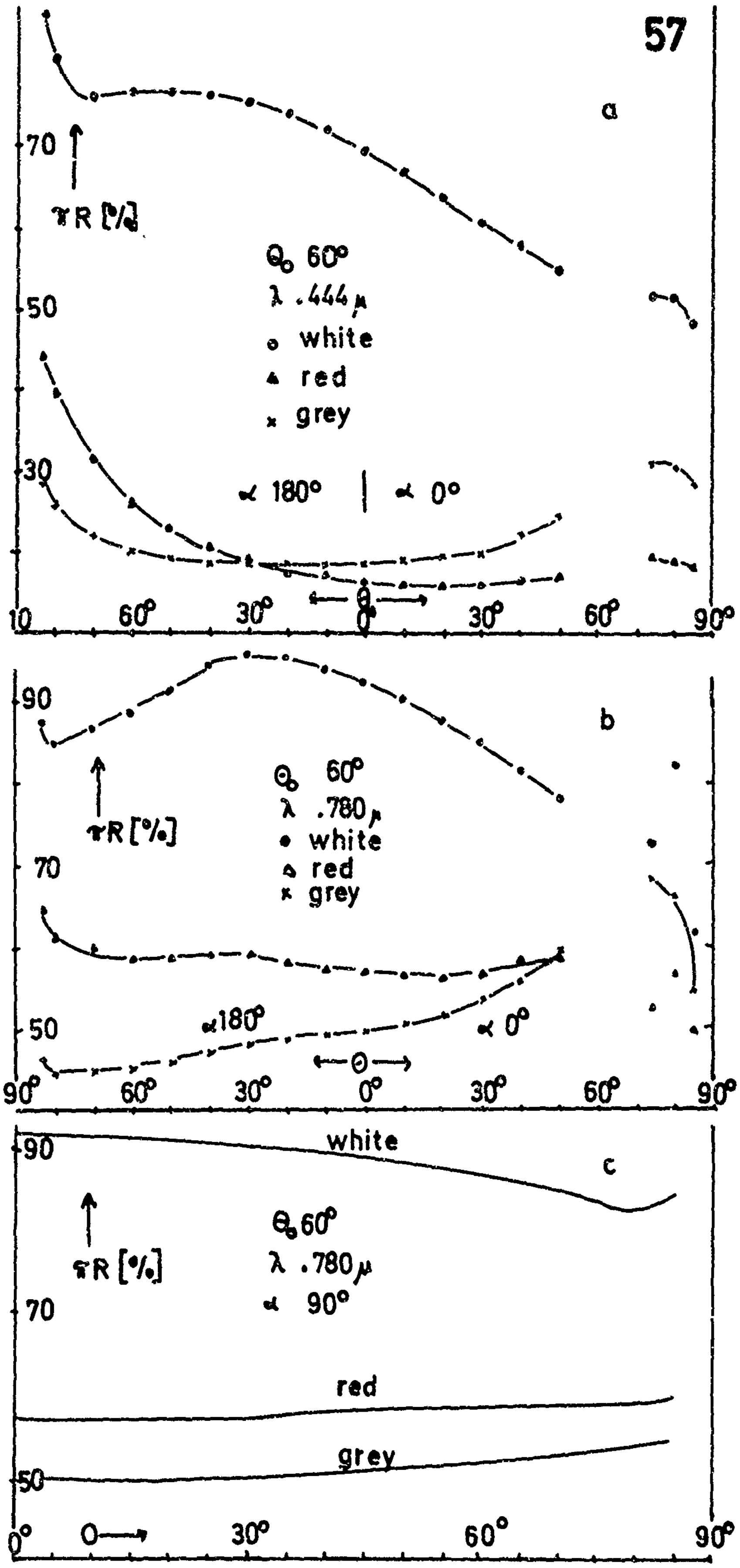
a
70
πR [%]
Θ_0 60°
λ .444 μ
white
red
grey
50
30
α 180°
α 0°
θ
10
60°
30°
0°
30°
60°
90°
b
90
Θ_0 60°
λ .780 μ
white
red
grey
πR [%]
70
α180°
α 0°
50
θ
90°
60°
30°
0°
30°
60°
90°
white
c
90
Θ_0 60°
λ .780 μ
α 90°
πR [%]
70
red
grey
50
0°
θ
30°
60°
90°

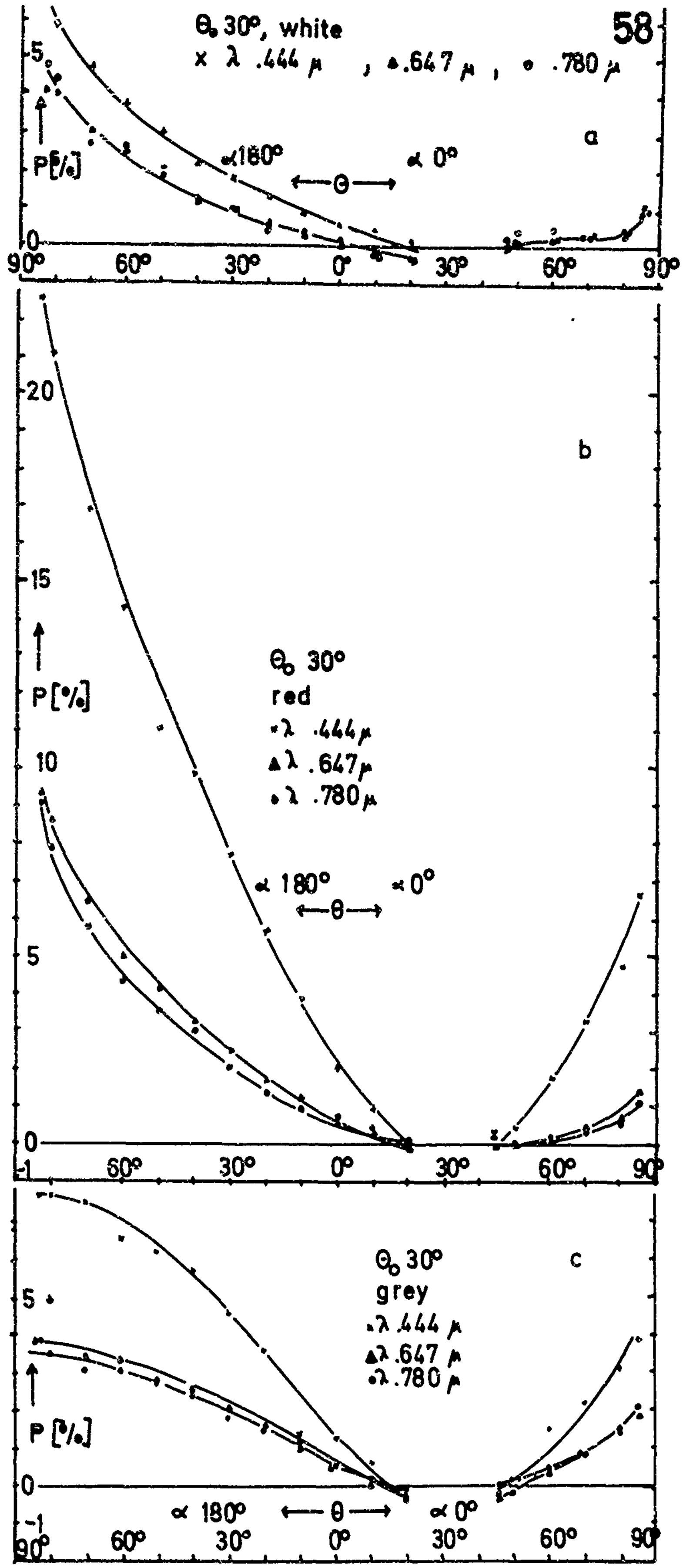

Θo 30°, white
× λ .444 μ , ▲.647 μ , • .780 μ
a
P[%]
α180° ←Θ→ α 0°
90° 60° 30° 0° 30° 60° 90°
b
Θo 30°
red
×λ .444μ
▲λ .647μ
•λ .780μ
α 180° ←θ→ α 0°
c
Θo 30°
grey
×λ .444 μ
▲λ .647 μ
•λ .780 μ

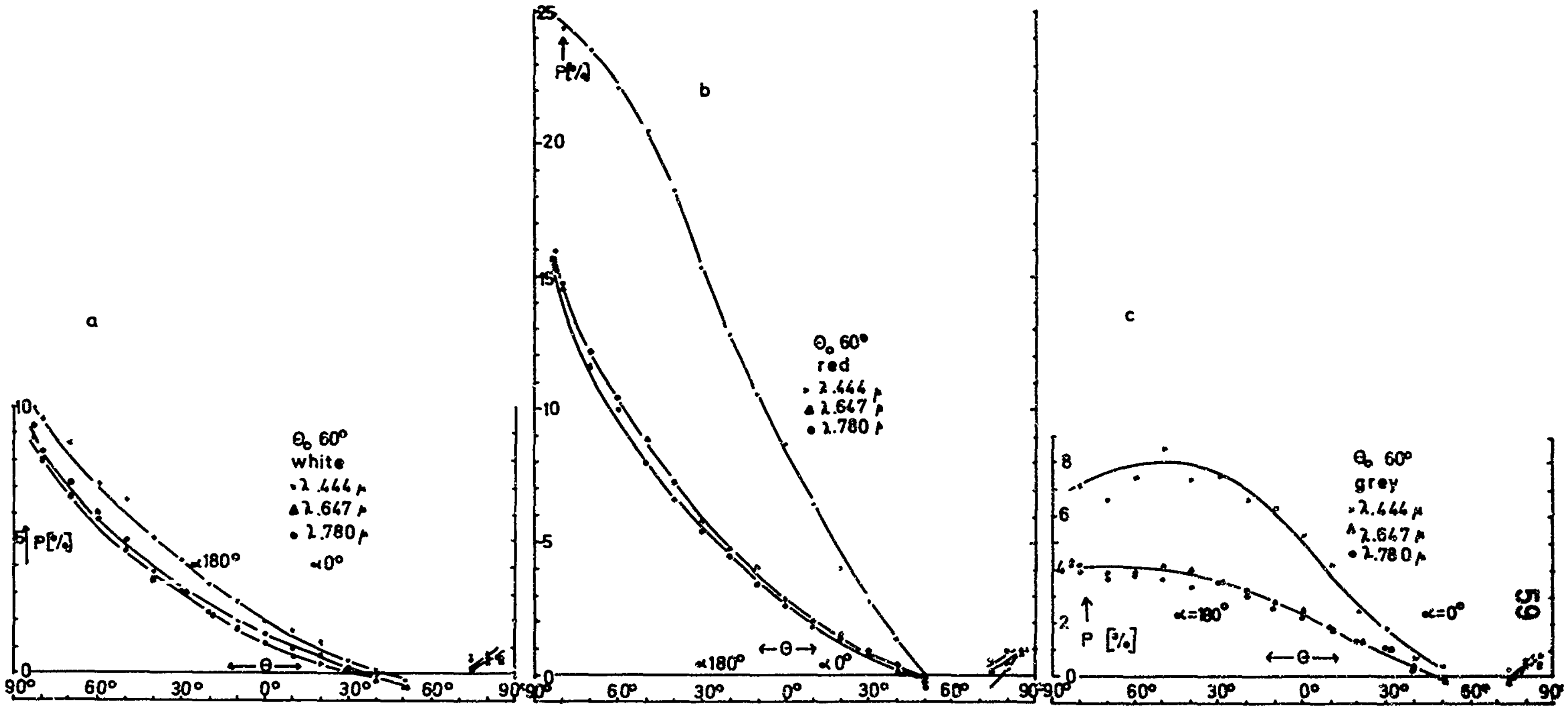
59
a
Θ_o 60°
white
λ .444 μ
λ .647 μ
λ .780 μ
α 180°
α 0°
P [%]
←Θ→
b
Θ_o 60°
red
λ .444 μ
λ .647 μ
λ .780 μ
α 180°
α 0°
P [%]
c
Θ_o 60°
grey
λ .444 μ
λ .647 μ
λ .780 μ
α = 180°
α = 0°
P [%]

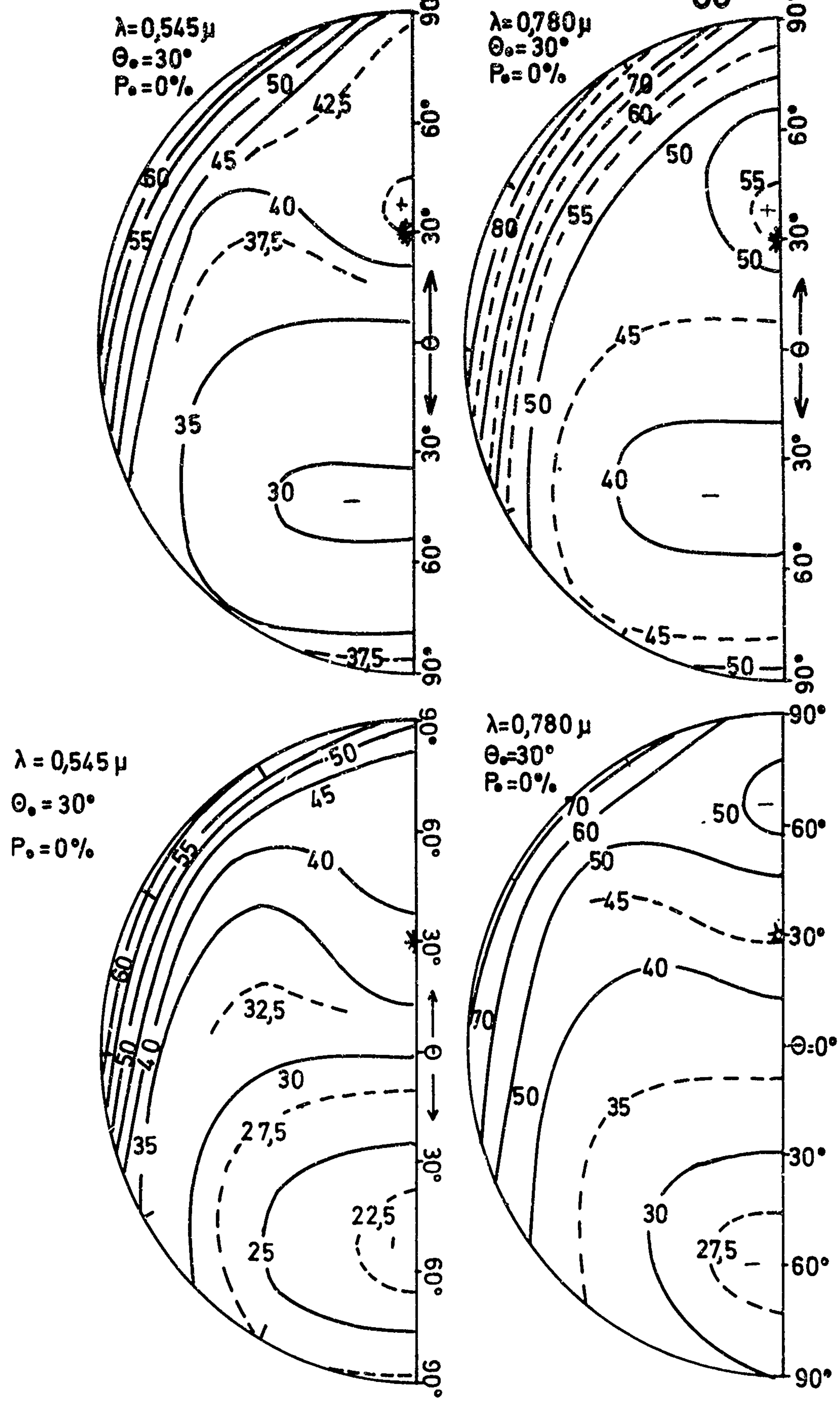
λ=0,545μ
Θ₀=30°
P₀=0%
λ=0,780μ
Θ₀=30°
P₀=0%
λ = 0,545 μ
Θ₀ = 30°
P₀ = 0%
λ=0,780μ
Θ₀=30°
P₀=0%
Θ=0°

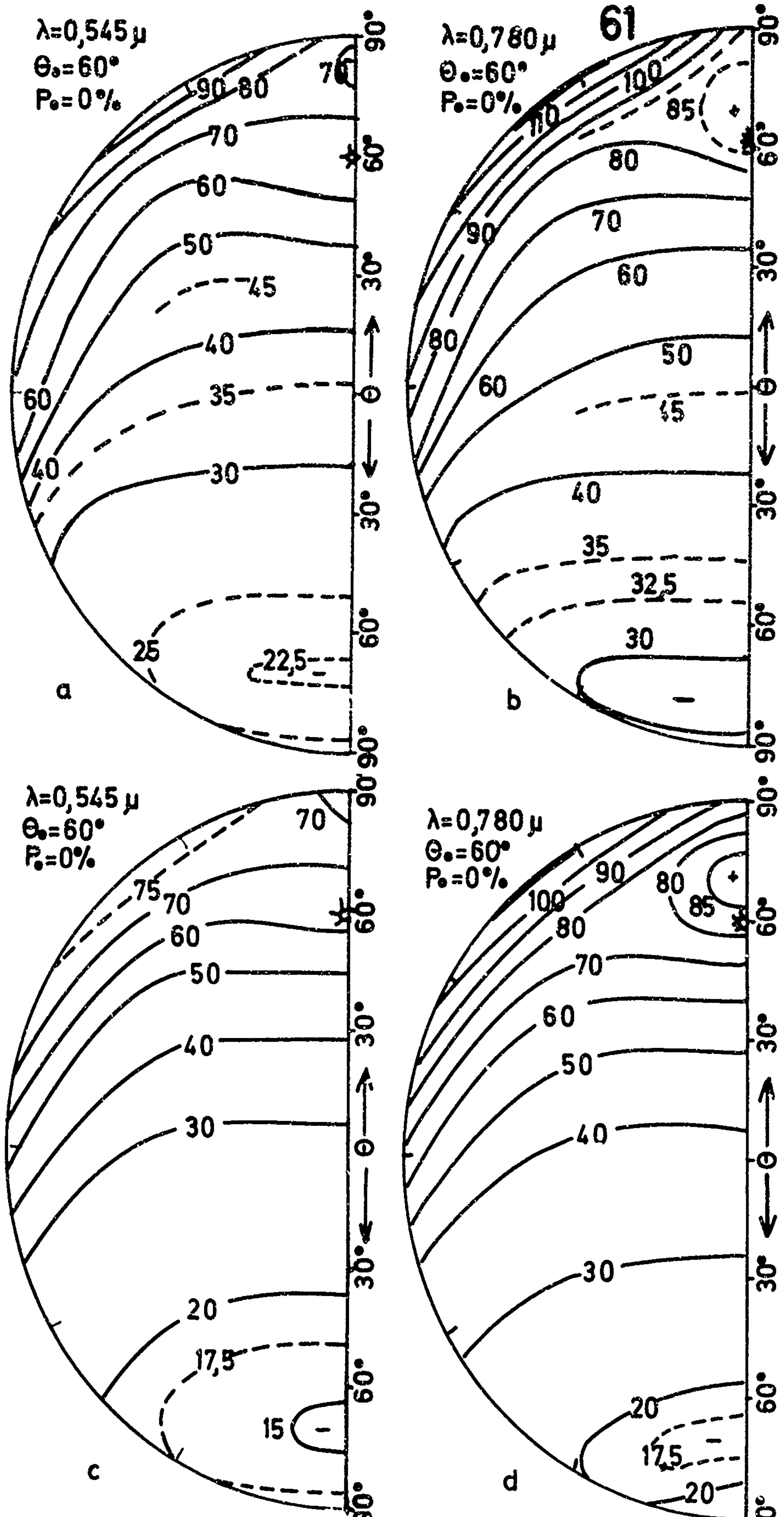
λ=0,545 μ
Θ₀=60°
P₀=0%
a
λ=0,780 μ
Θ₀=60°
P₀=0%
b
λ=0,545 μ
Θ₀=60°
P₀=0%
c
λ=0,780 μ
Θ₀=60°
P₀=0%
d

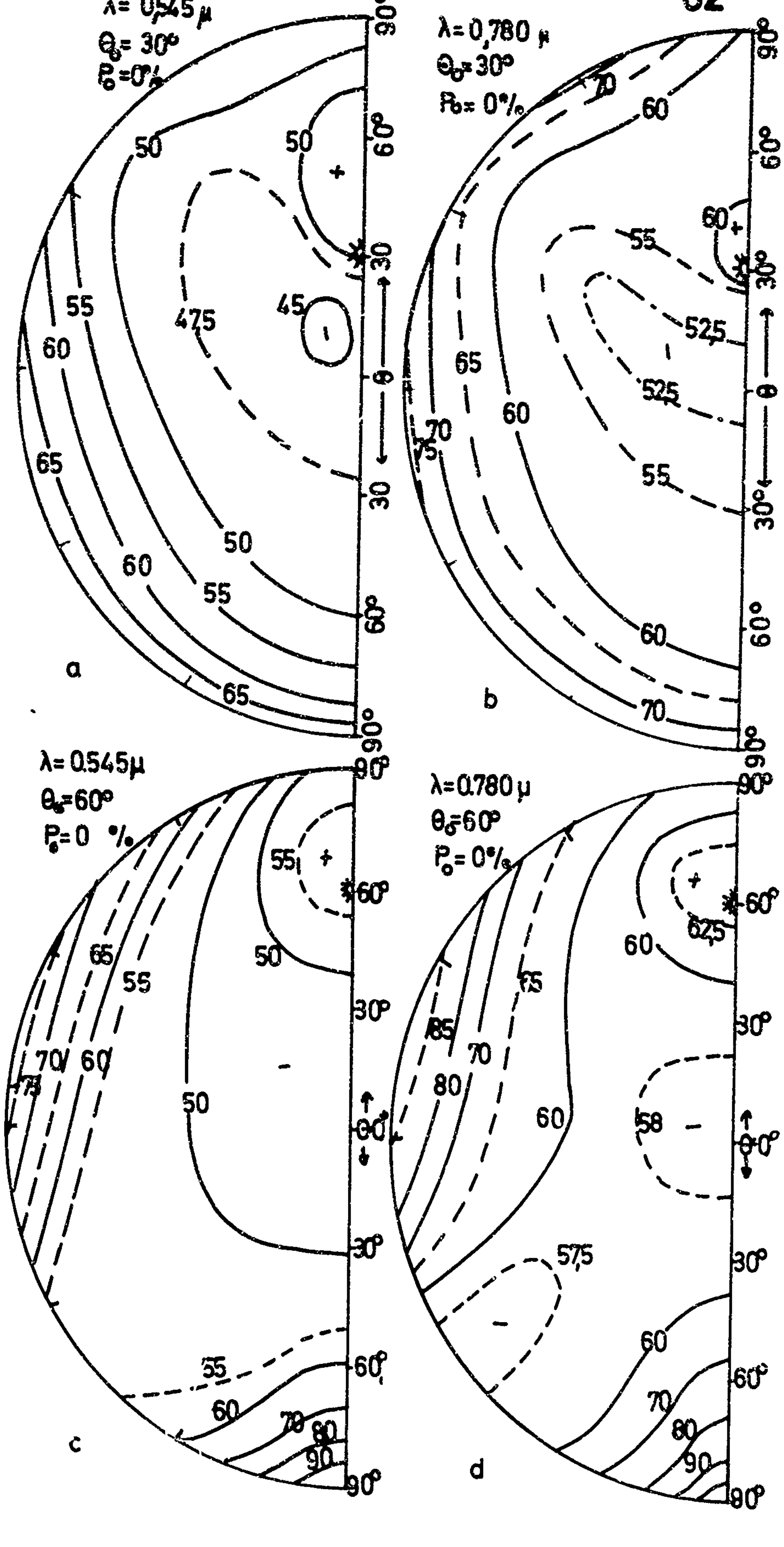
λ= 0,545 μ
Θo= 30°
Po=0%
λ= 0,780 μ
Θo=30°
Po= 0%
a
b
λ= 0.545μ
θo=60°
Po= 0 %
λ=0.780 μ
θo=60°
Po= 0%
c
d

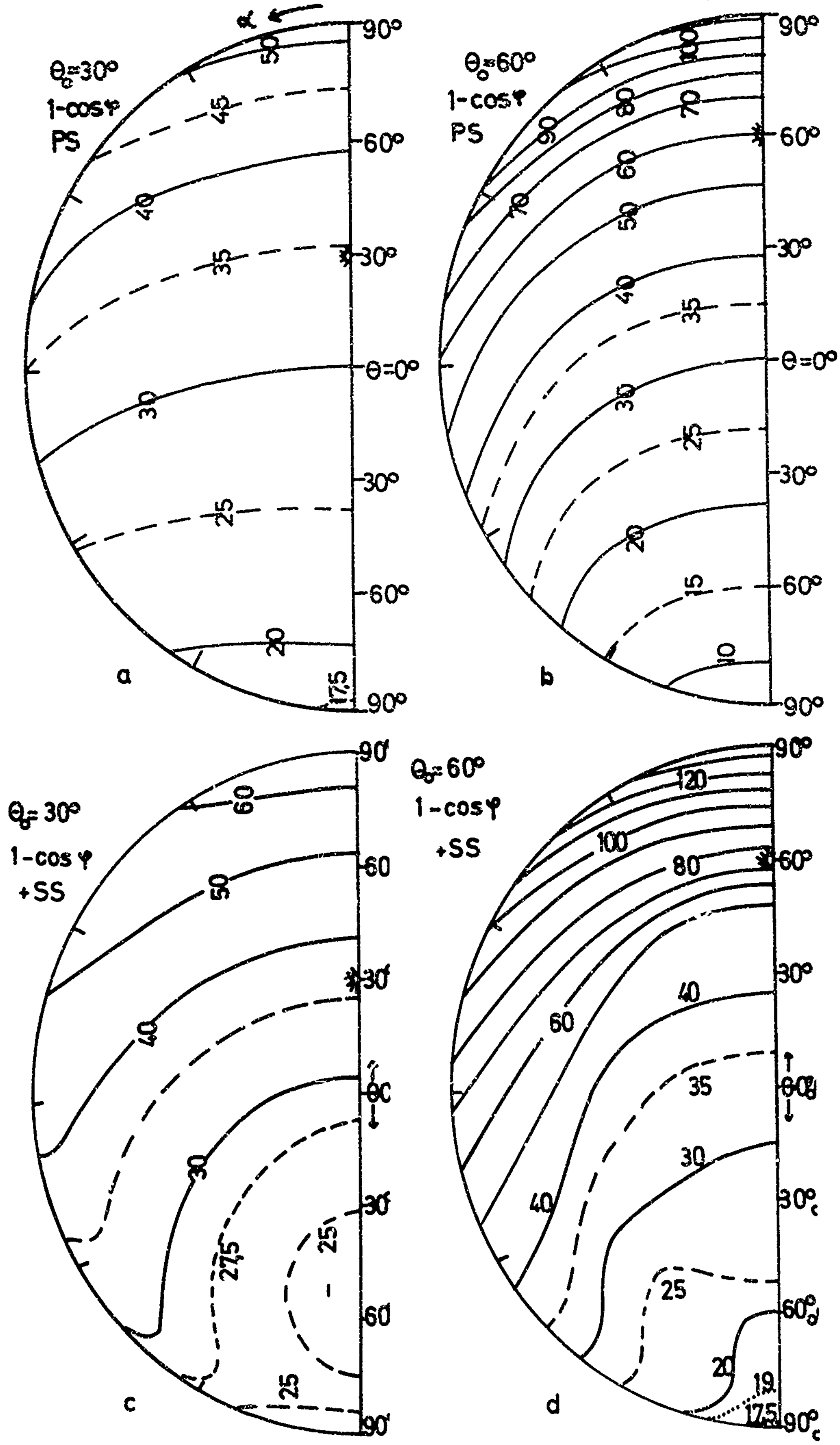

$\theta_0 = 30°$
1-cos φ
PS
$\theta_0 = 60°$
1-cos φ
PS
$\theta_0 = 30°$
1-cos φ
+SS
$\theta_0 = 60°$
1-cos φ
+SS
α
90°
60°
30°
θ=0°
a
b
c
d

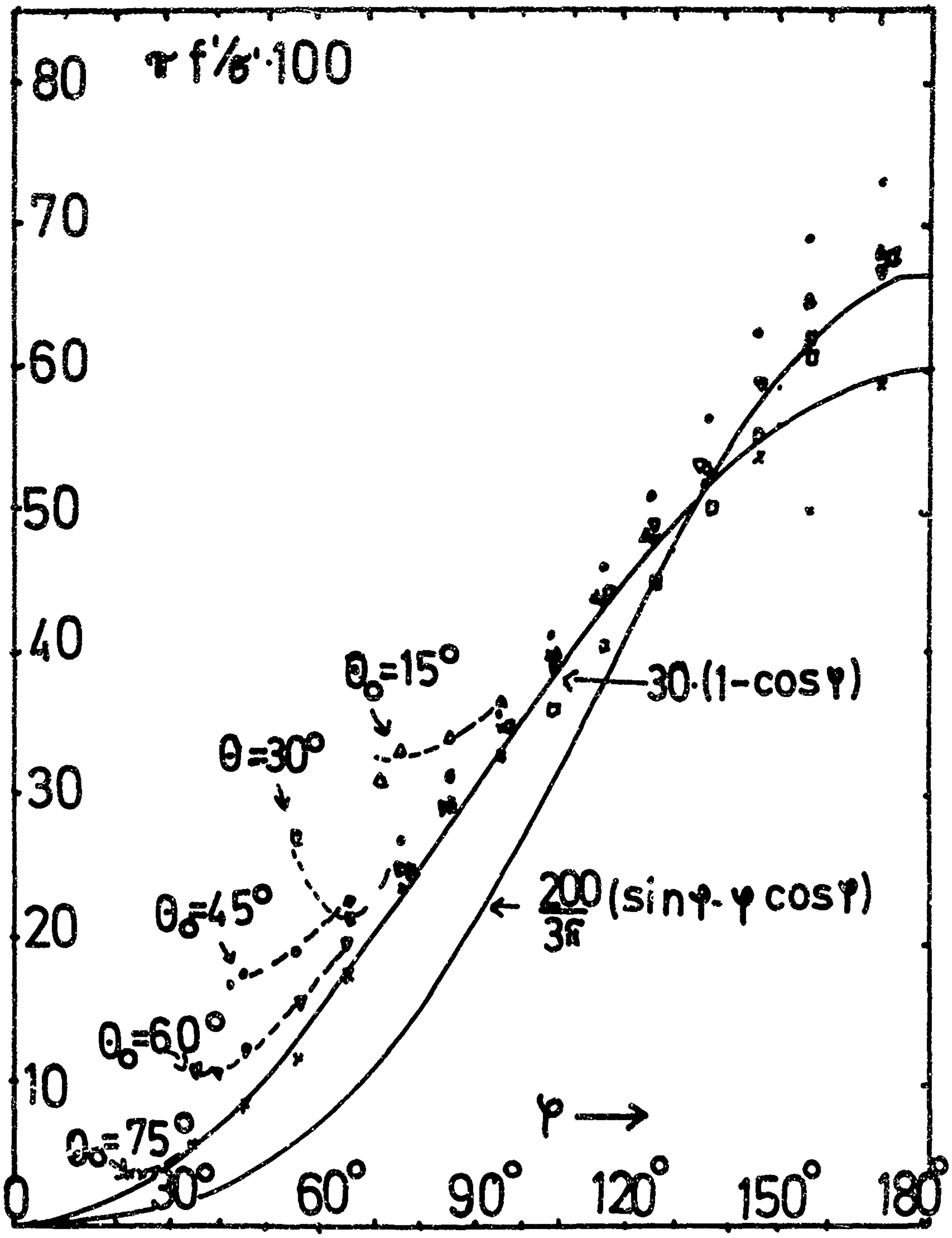

$\pi f'/\sigma' \cdot 100$
80
70
60
50
40
30
20
10
0
30°
60°
90°
120°
150°
180°
$\varphi \longrightarrow$
$\theta_0=15°$
$\theta=30°$
$\theta_0=45°$
$\theta_0=60°$
$\theta_0=75°$
$30 \cdot (1-\cos\varphi)$
$\frac{200}{3\pi}(\sin\varphi - \varphi\cos\varphi)$

65

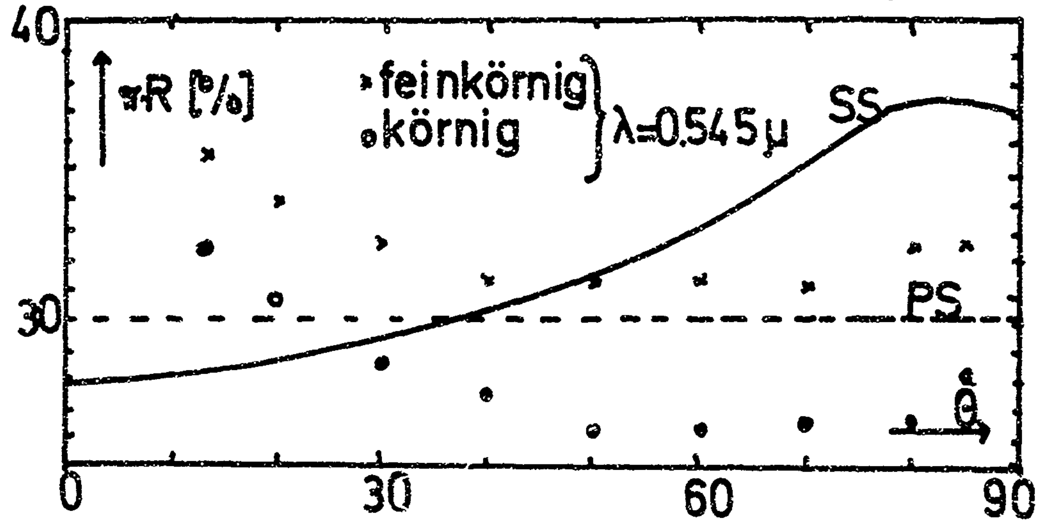
40
30
↑ π·R [%]
× feinkörnig
• körnig
λ=0.545 μ
SS
PS
θ
0
30
60
90

66

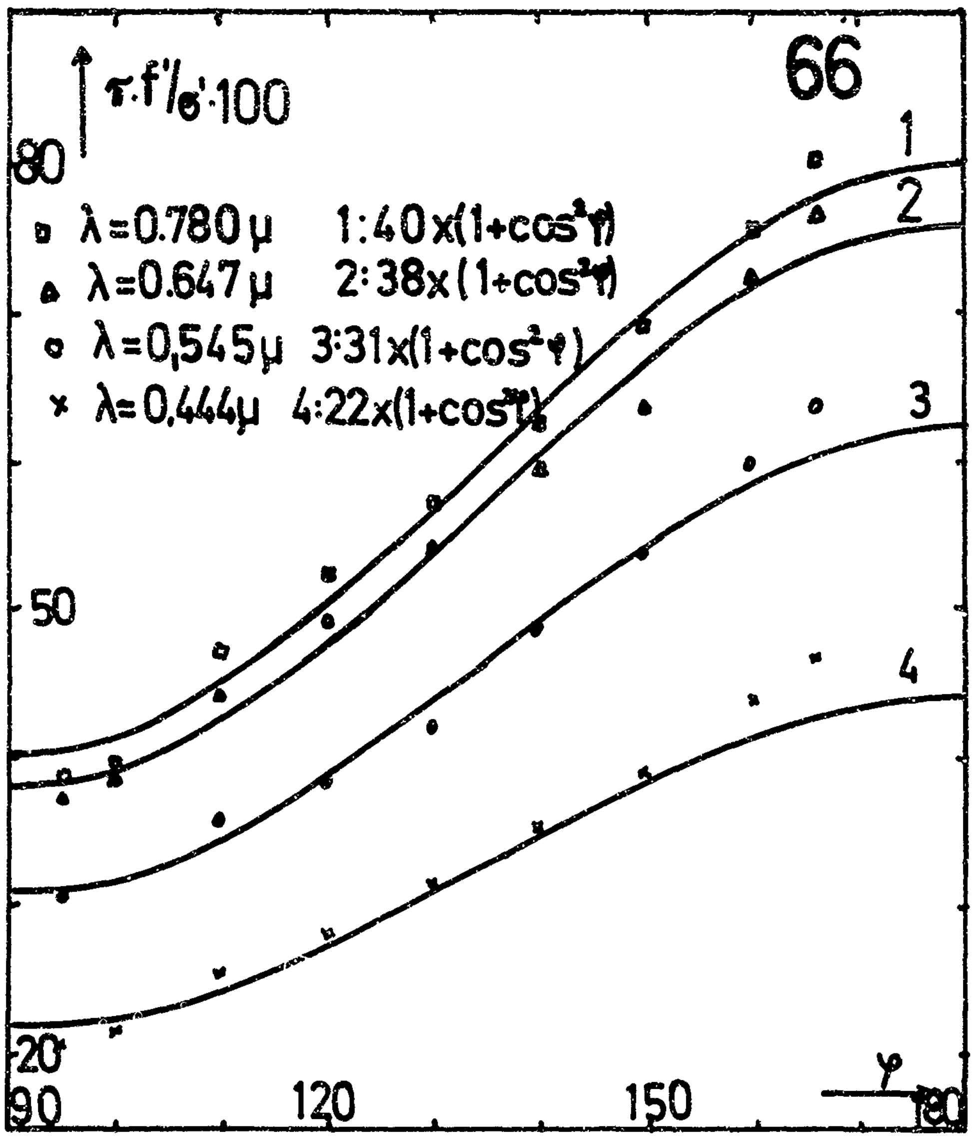
↑ π·f'/σ'·100
80
50
20
1
2
3
4
▫ λ=0.780 μ 1:40x(1+cos²φ)
▵ λ=0.647 μ 2:38x(1+cos²φ)
∘ λ=0,545μ 3:31x(1+cos²φ)
× λ=0,444μ 4:22x(1+cos²φ)
φ
90
120
150
180

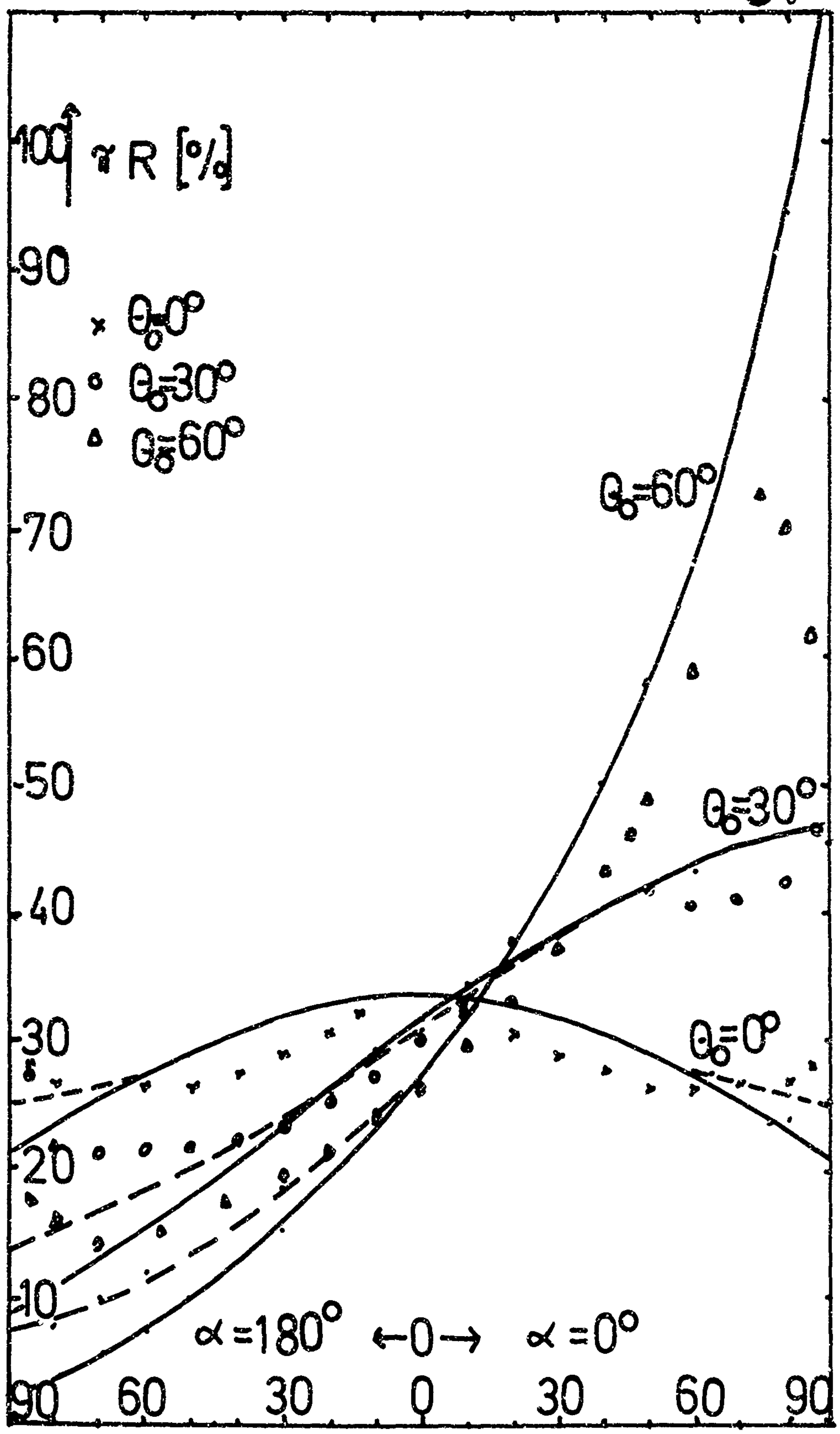
100 γR [%]
90
80
70
60
50
40
30
20
10
× Θ₀=0°
° Θ₀=30°
Δ Θ₀=60°
Θ₀=60°
Θ₀=30°
Θ₀=0°
α=180° ←0→ α=0°
90 60 30 0 30 60 90

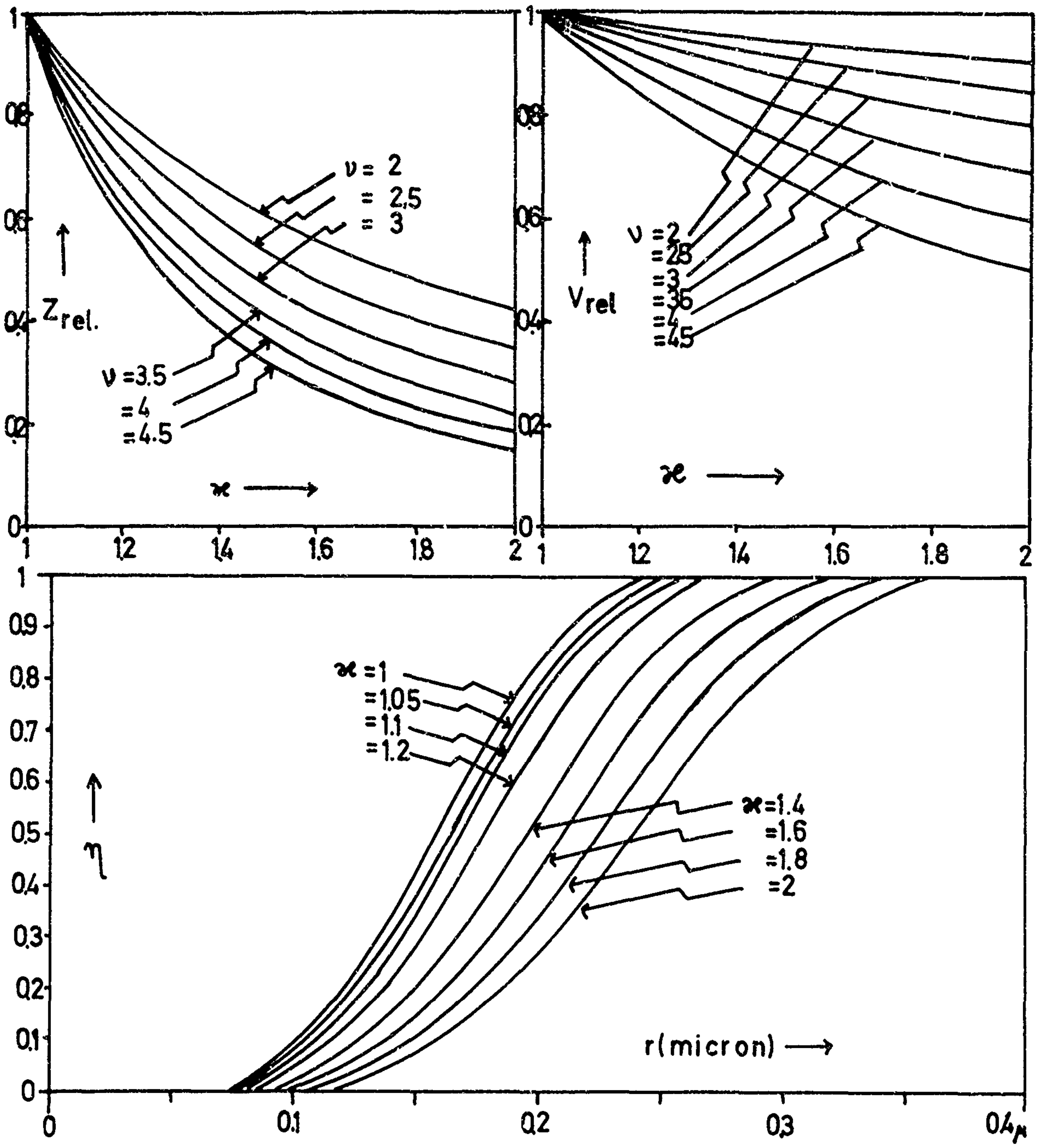

$Z_{rel.}$
$\nu = 2$
$= 2,5$
$= 3$
$\nu = 3.5$
$= 4$
$= 4.5$
$\varkappa$
V_{rel}
$\nu = 2$
$= 2,5$
$= 3$
$= 3,5$
$= 4$
$= 4,5$
$\varkappa$
η
$\varkappa = 1$
$= 1,05$
$= 1,1$
$= 1.2$
$\varkappa = 1.4$
$= 1.6$
$= 1.8$
$= 2$
r(micron)

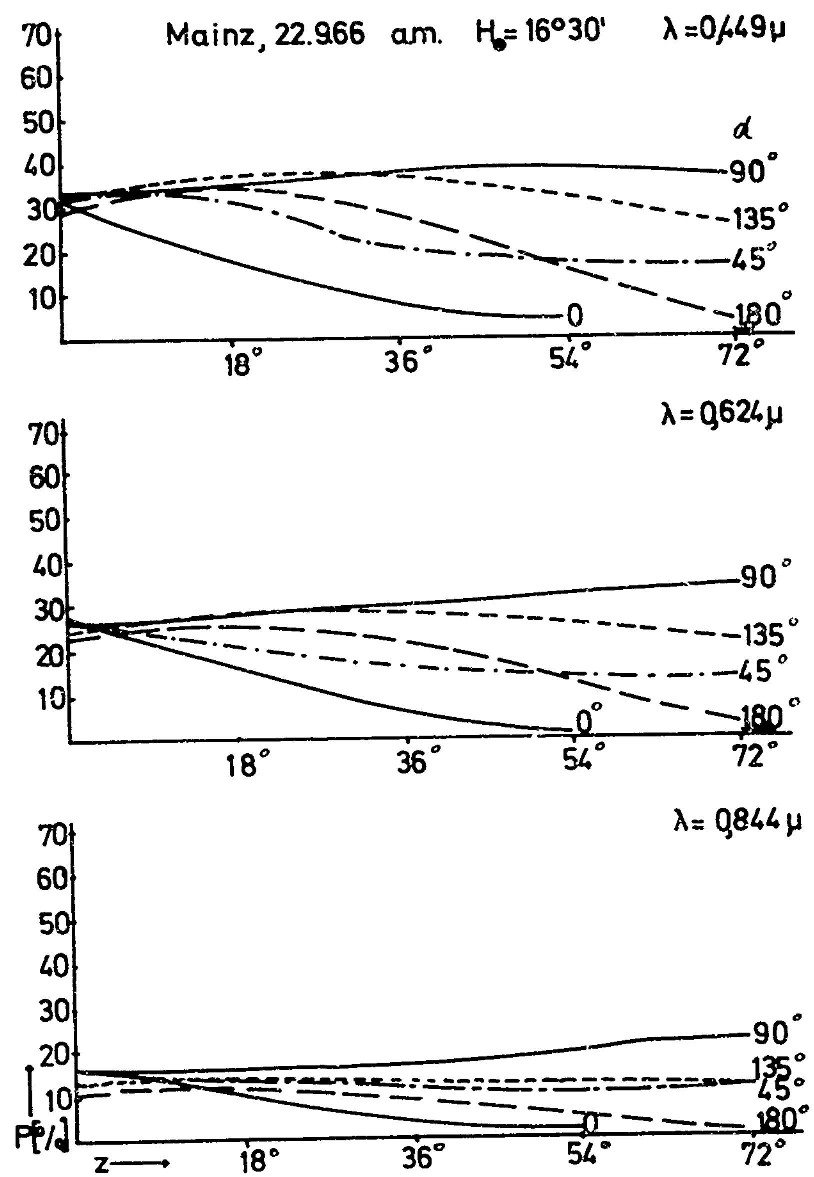
Mainz, 22.9.66 a.m. $H_\odot$ = 16°30' λ = 0,449 μ
λ = 0,624 μ
λ = 0,844 μ
α
90°
135°
45°
180°
0
18°
36°
54°
72°
10
20
30
40
50
60
70
P [%]
z

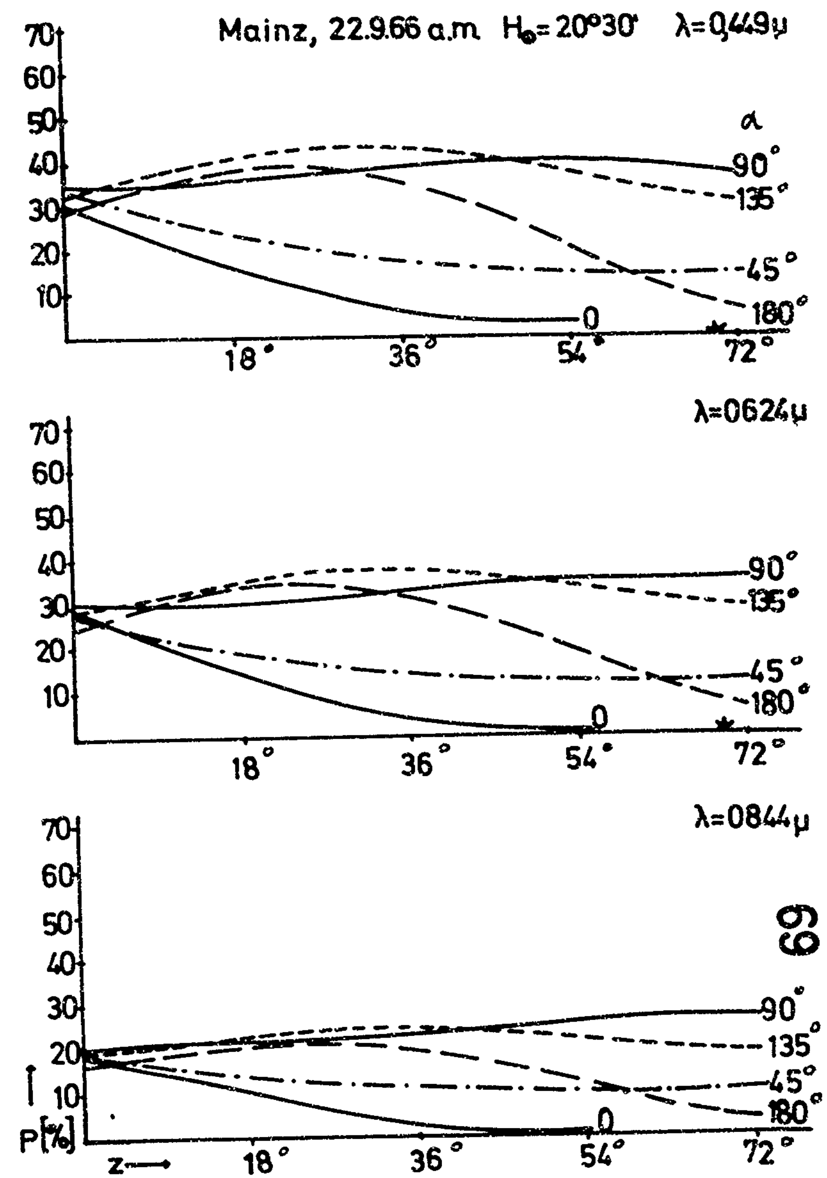
Mainz, 22.9.66 a.m. $H_\odot$ = 20°30' λ = 0,449 μ
λ = 0624 μ
λ = 0844 μ
α
90°
135°
45°
180°
0
18°
36°
54°
72°
10
20
30
40
50
60
70
P [%]
z

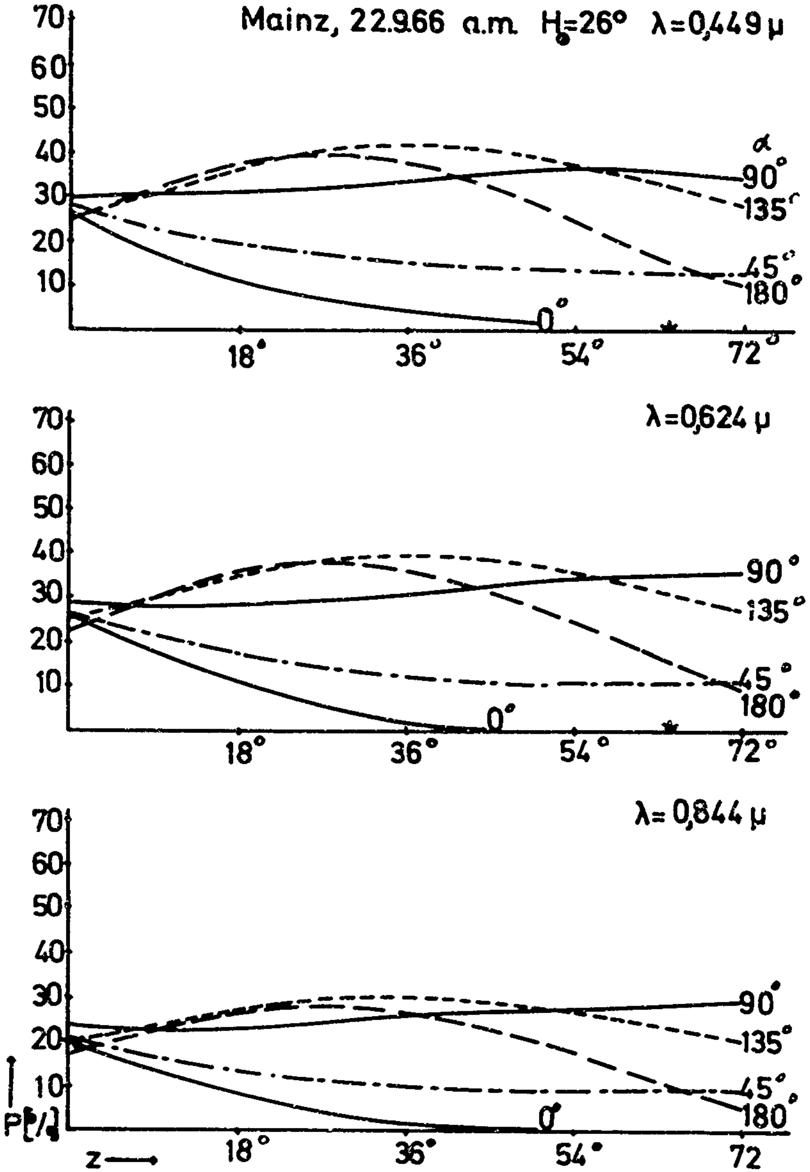
Mainz, 22.9.66 a.m. H=26° λ=0,449 μ
λ=0,624 μ
λ=0,844 μ
α
90°
135°
45°
180°
0°
18°
36°
54°
72°
P[%]
z

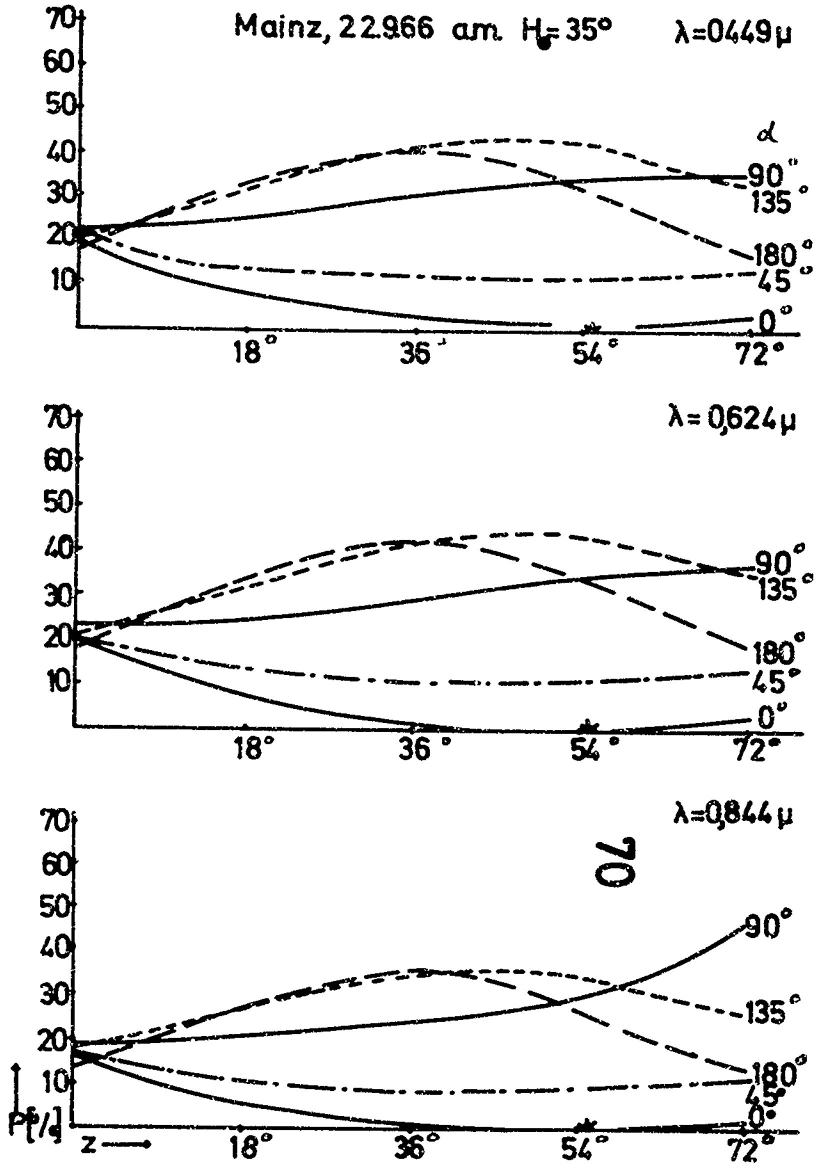
Mainz, 22.9.66 a.m. H=35° λ=0449 μ
λ=0,624 μ
λ=0,844 μ
α
90°
135°
180°
45°
0°
18°
36°
54°
72°
P[%]
z

70

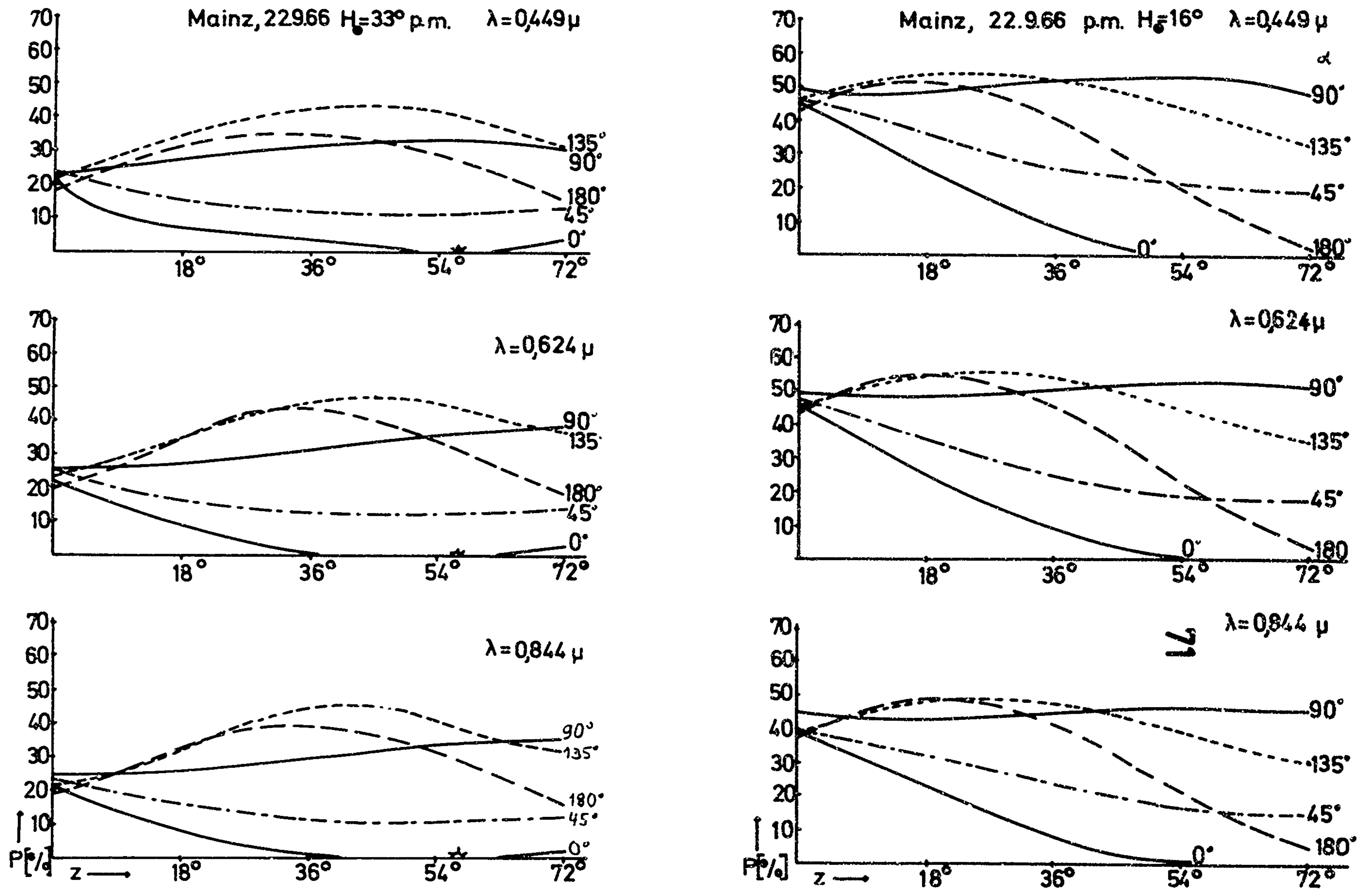
Mainz, 22.9.66 H=33° p.m. λ=0,449 μ
λ=0,624 μ
λ=0,844 μ
135°
90°
180°
45°
0°
70
60
50
40
30
20
10
18°
36°
54°
72°
P[%]
z
Mainz, 22.9.66 p.m. H=16° λ=0,449 μ
α
λ=0,624 μ
λ=0,844 μ
90°
135°
45°
180°
0°

71

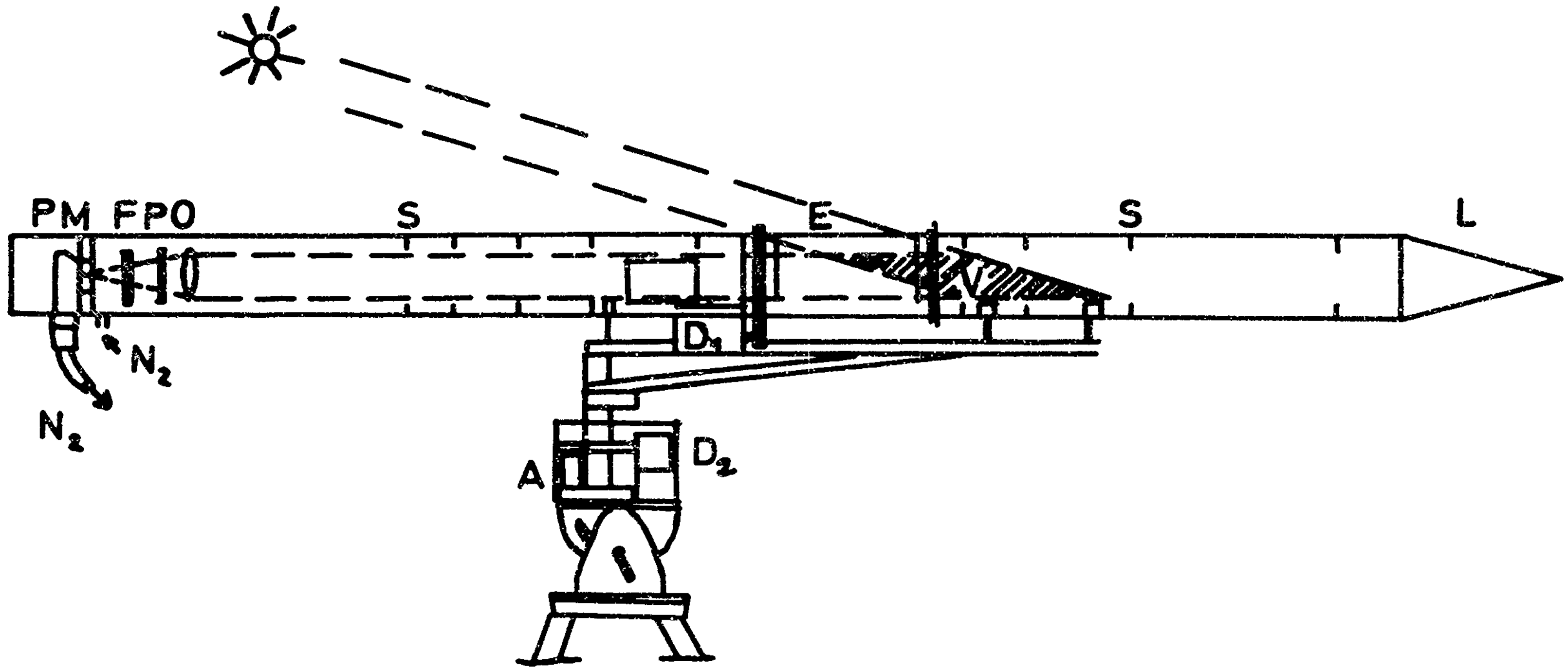

72

A = Angle Pickoff Potentiometer	D_2 = Scattering Angle Drive	N_2 = Nitrogen Input	PM = Photomultiplier
C = Chopper	F = Filter	O = Photometer Lens	S = Stop
D_1 = Chopper Drive	L = Light Trap	P = Polarizer Filter	V = Scattering Volume

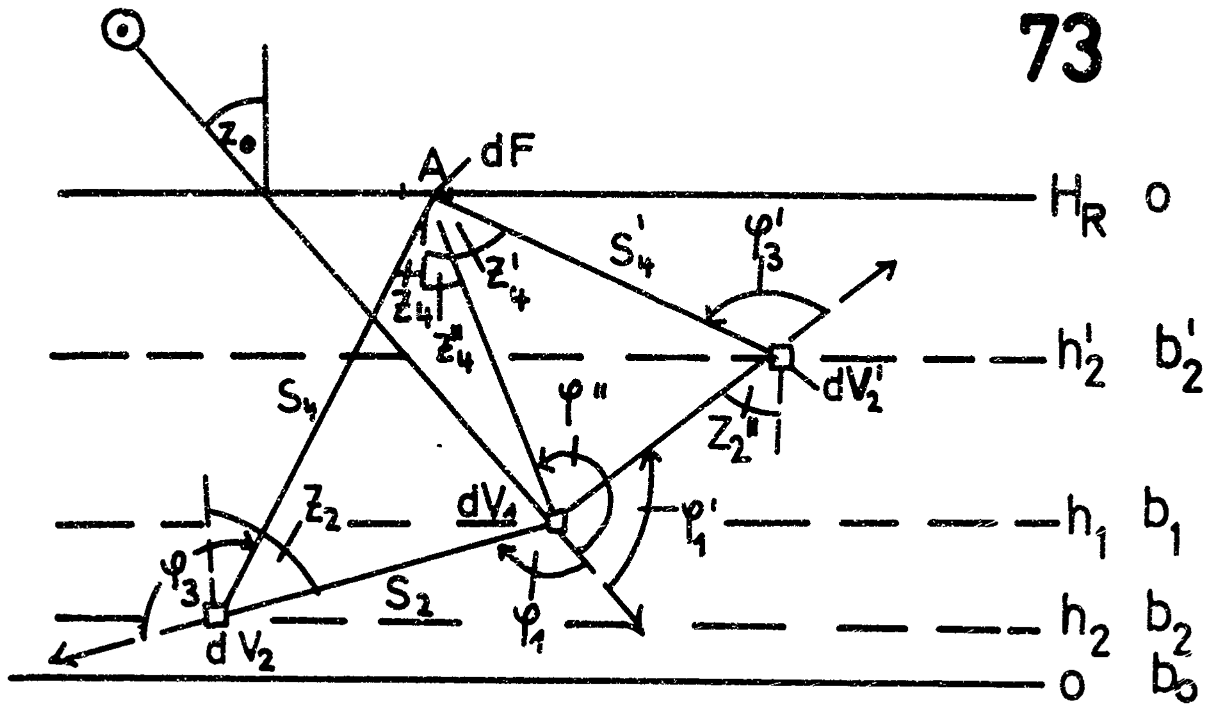
A
dF
$z_\odot$
H_R o
S_4'
φ_3'
z_4'
z_4
z_4''
h_2' b_2'
dV_2'
S_4
φ''
Z_2''
Z_2
dV_1
φ_1'
h_1 b_1
φ_3
S_2
φ_1
h_2 b_2
dV_2
o b_o

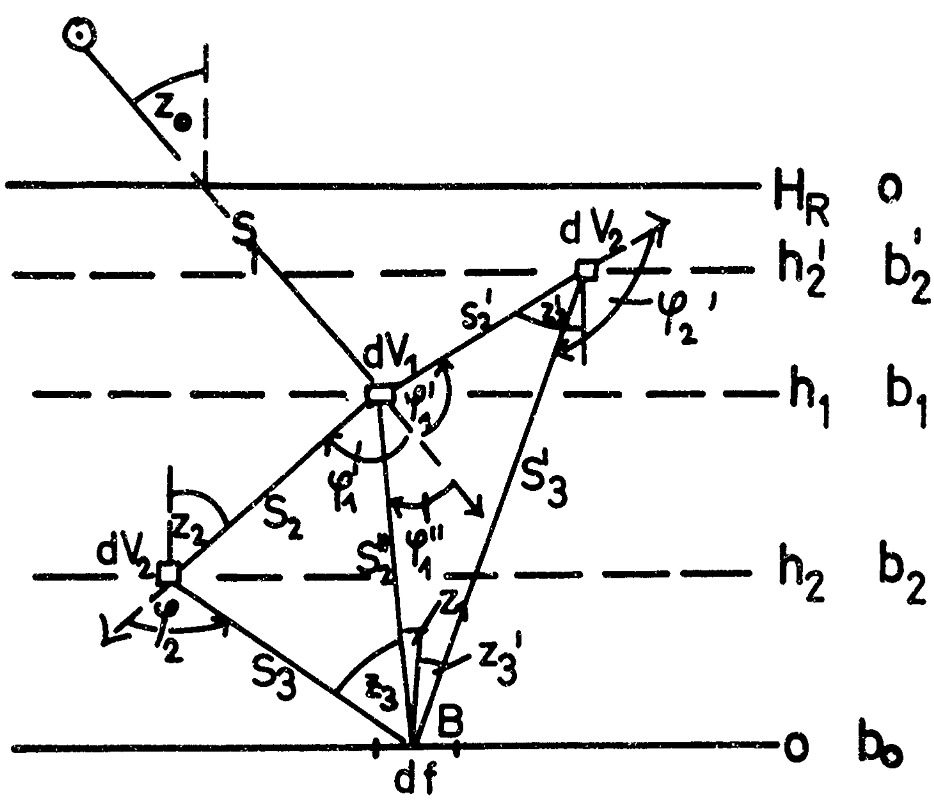
$z_\odot$
H_R o
S
dV_2
h_2' b_2'
S_2'
φ_2'
dV_1
φ_2'
h_1 b_1
φ_1'
S_3'
z_2
S_2
S_2''
φ_1''
dV_2
h_2 b_2
φ_2
z_3'
S_3
z_3
B
o b_o
df

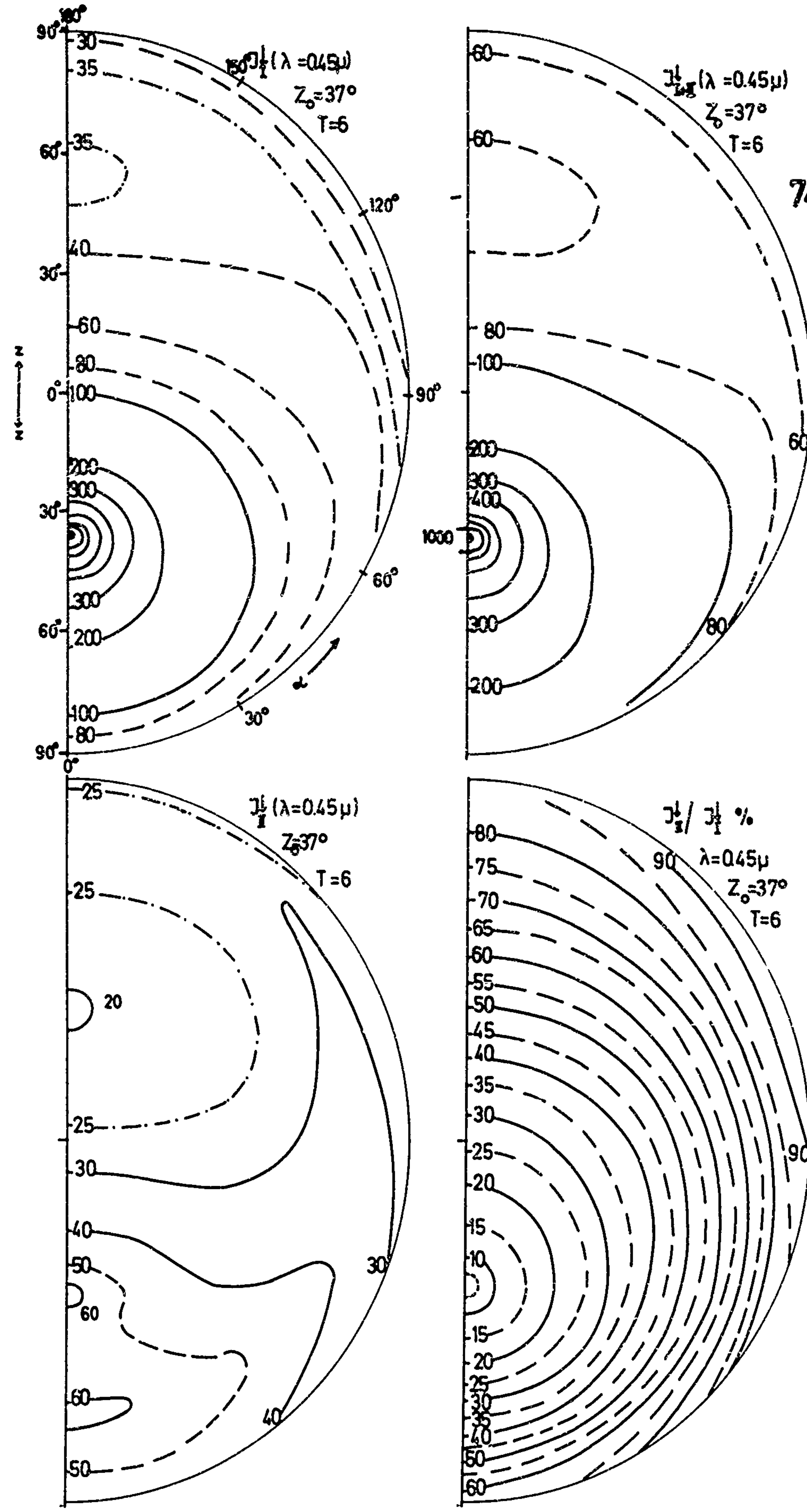
J↓I (λ=0.45μ)
Z0=37°
T=6
J↓I+II (λ=0.45μ)
Z0=37°
T=6
J↓II (λ=0.45μ)
Z0=37°
T=6
J↓II / J↓I %
λ=0.45μ
Z0=37°
T=6

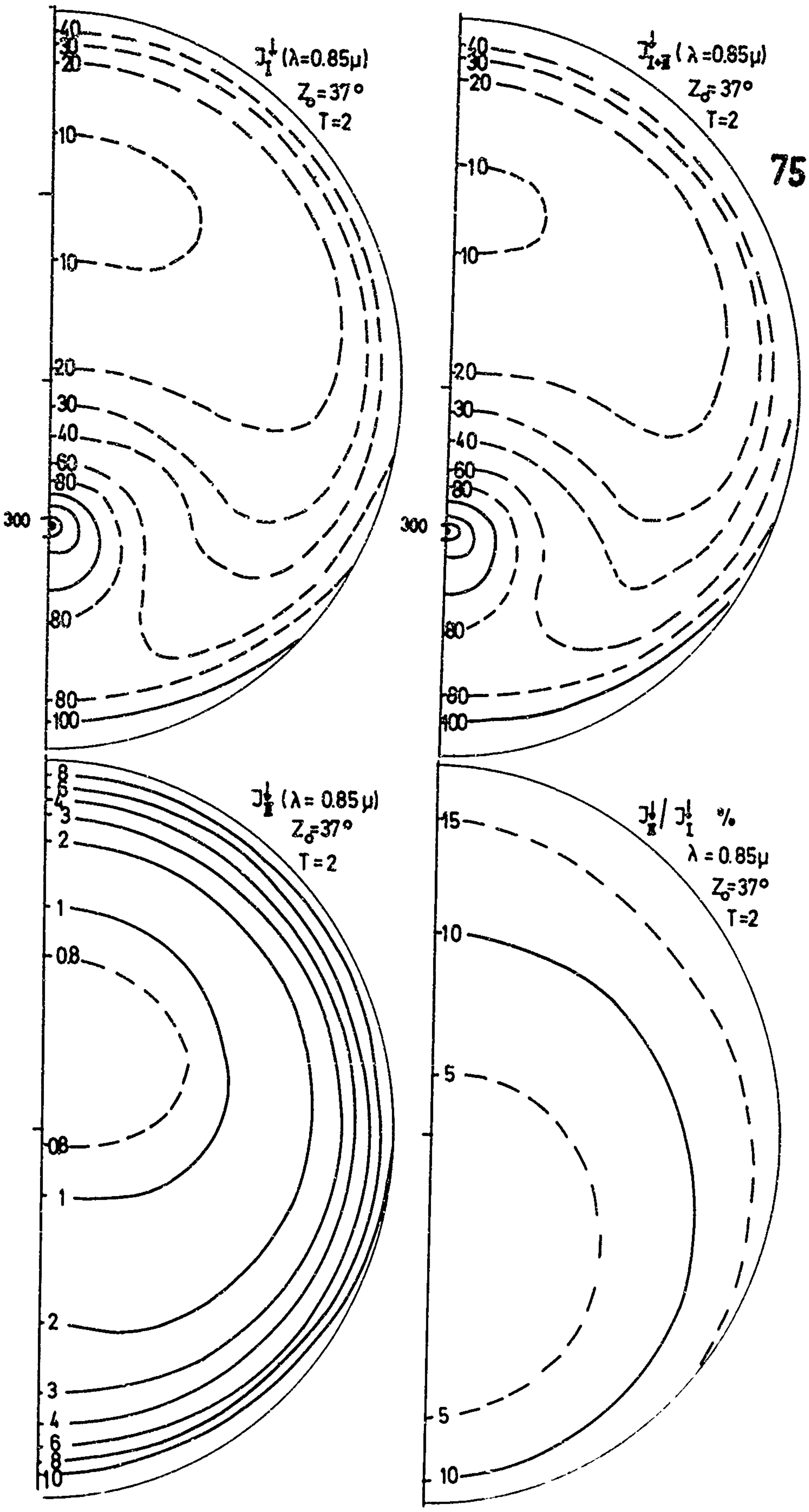

$J_I^{\downarrow}$ (λ=0.85μ)
Z_0=37°
T=2
40
30
20
10
10
20
30
40
60
80
300
80
80
100
$J_{I+II}^{\downarrow}$ (λ=0.85μ)
Z_0=37°
T=2
40
30
20
10
10
20
30
40
60
80
300
80
80
100
$J_{II}^{\downarrow}$ (λ=0.85μ)
Z_0=37°
T=2
8
6
4
3
2
1
0.8
0.8
1
2
3
4
6
8
10
$J_{II}^{\downarrow}/J_I^{\downarrow}$ %
λ=0.85μ
Z_0=37°
T=2
15
10
5
5
10

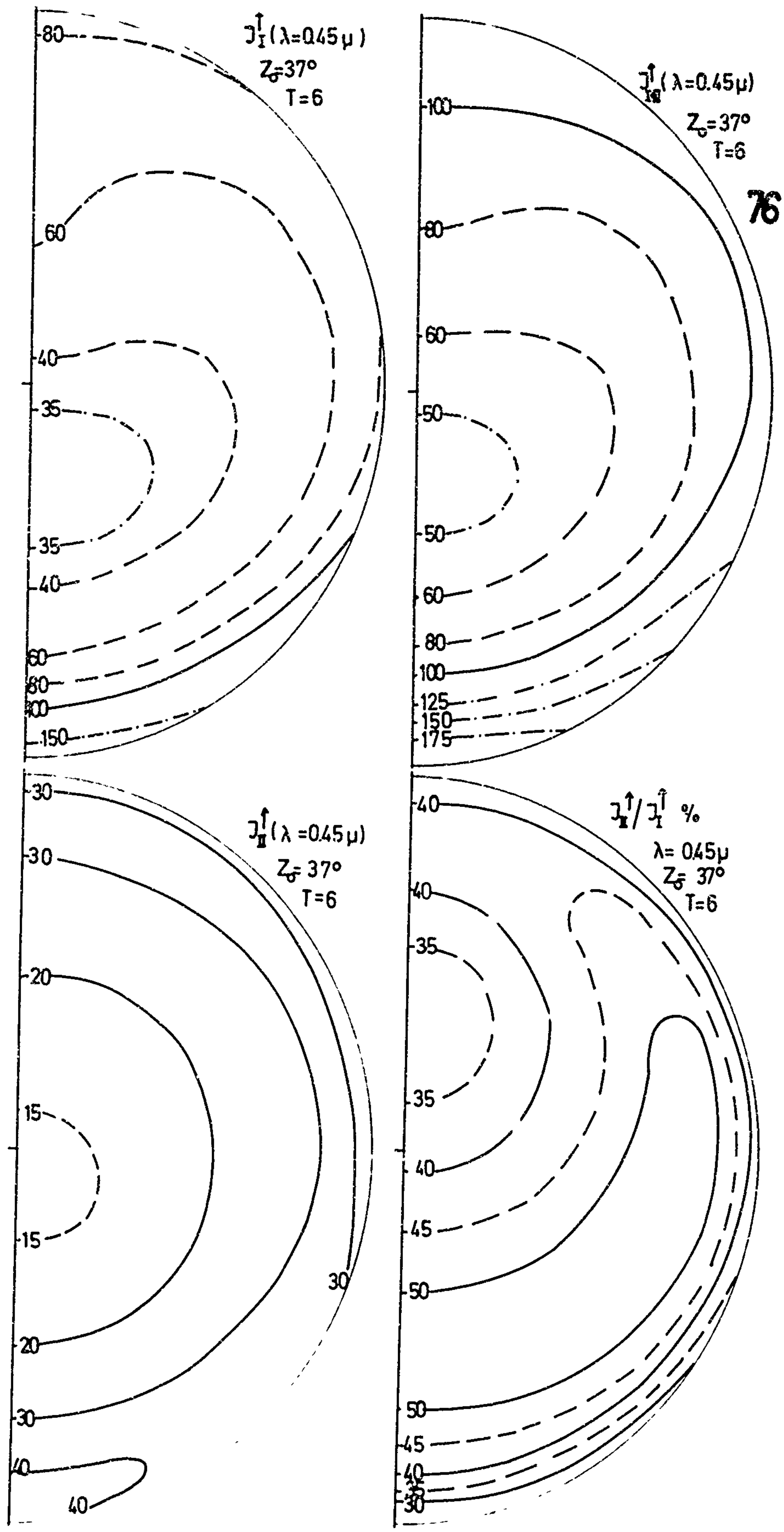

76

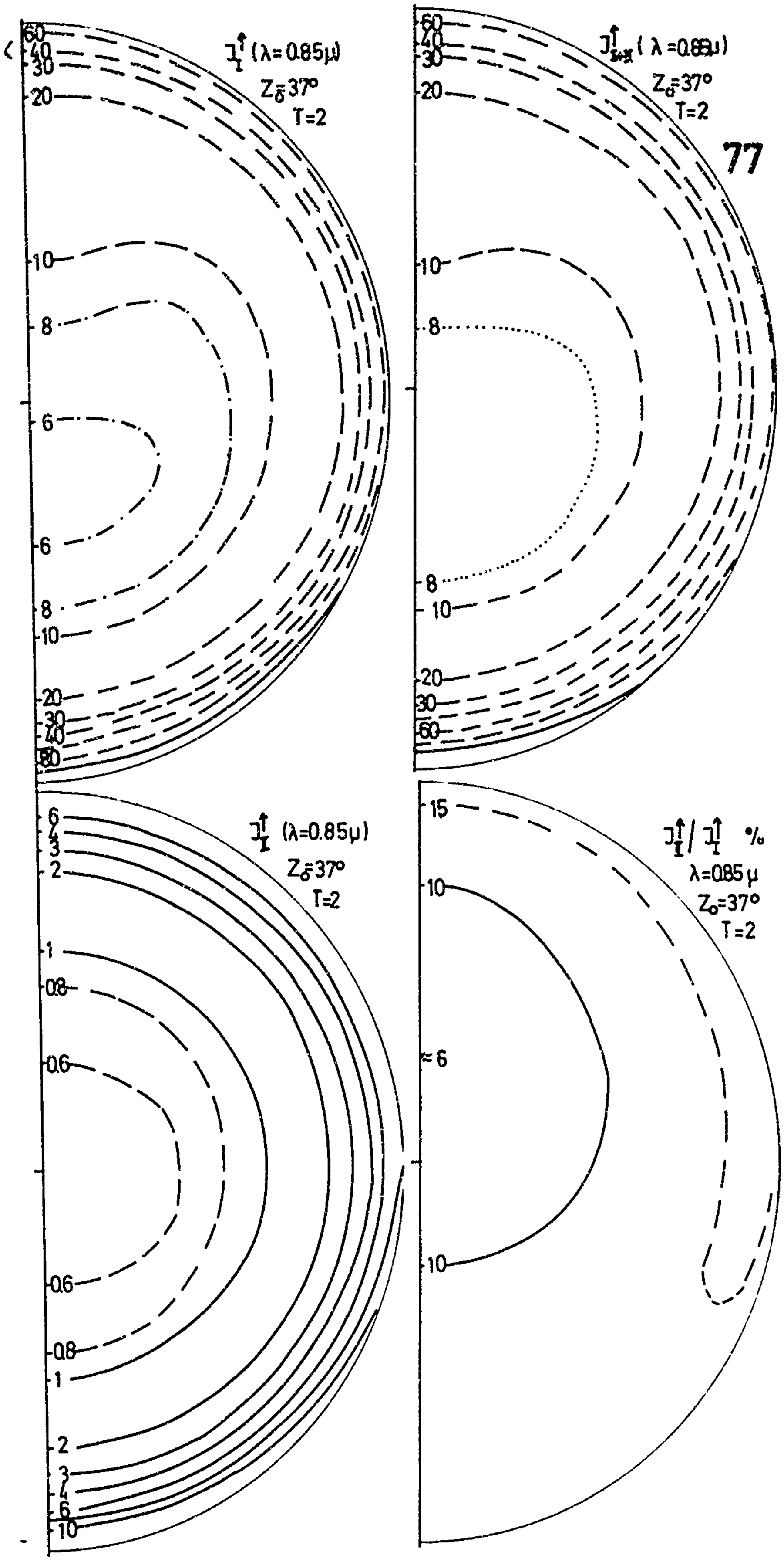
$J_I^{\uparrow}$ (λ=0.85μ)
Z_0=37°
T=2
$J_{I+II}^{\uparrow}$ (λ=0.85μ)
Z_0=37°
T=2
$J_{II}^{\uparrow}$ (λ=0.85μ)
Z_0=37°
T=2
$J_{II}^{\uparrow}$ / $J_I^{\uparrow}$ %
λ=0.85 μ
Z_0=37°
T=2
60
40
30
20
10
8
6
4
3
2
1
0.8
0.6
15

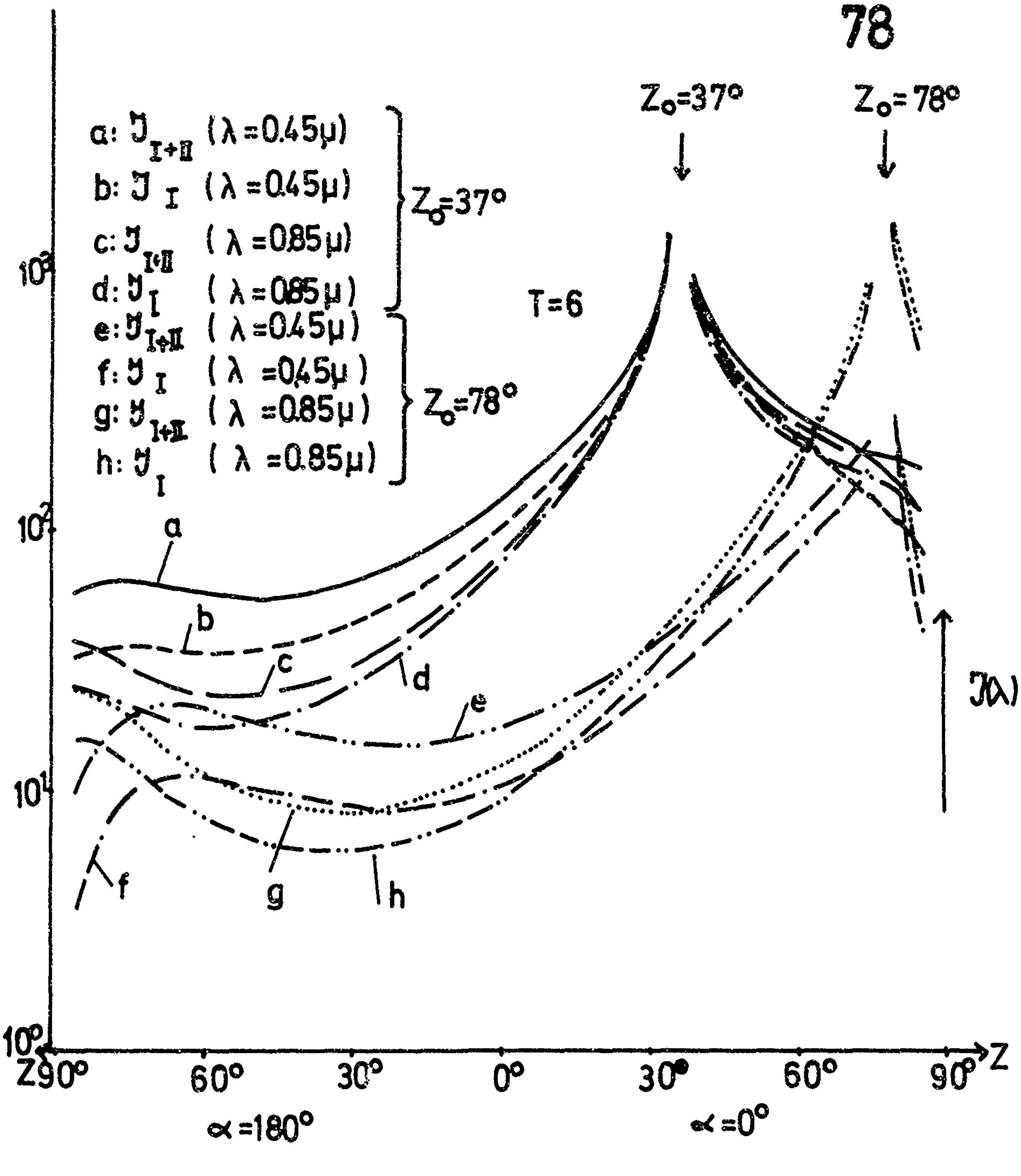

a: $\mathfrak{I}_{I+II}$ (λ = 0.45μ)
b: $\mathfrak{I}_{I}$ (λ = 0.45μ)
c: $\mathfrak{I}_{I+II}$ (λ = 0.85μ)
d: $\mathfrak{I}_{I}$ (λ = 0.85μ)
Z_o=37°
e: $\mathfrak{I}_{I+II}$ (λ = 0.45μ)
f: $\mathfrak{I}_{I}$ (λ = 0.45μ)
g: $\mathfrak{I}_{I+II}$ (λ = 0.85μ)
h: $\mathfrak{I}_{I}$ (λ = 0.85μ)
Z_o=78°
Z_o=37°
Z_o= 78°
T=6
10^3
10^2
10^1
10^0
a
b
c
d
e
f
g
h
$\mathfrak{I}(\lambda)$
Z 90°
60°
30°
0°
30°
60°
90°
Z
α =180°
α =0°

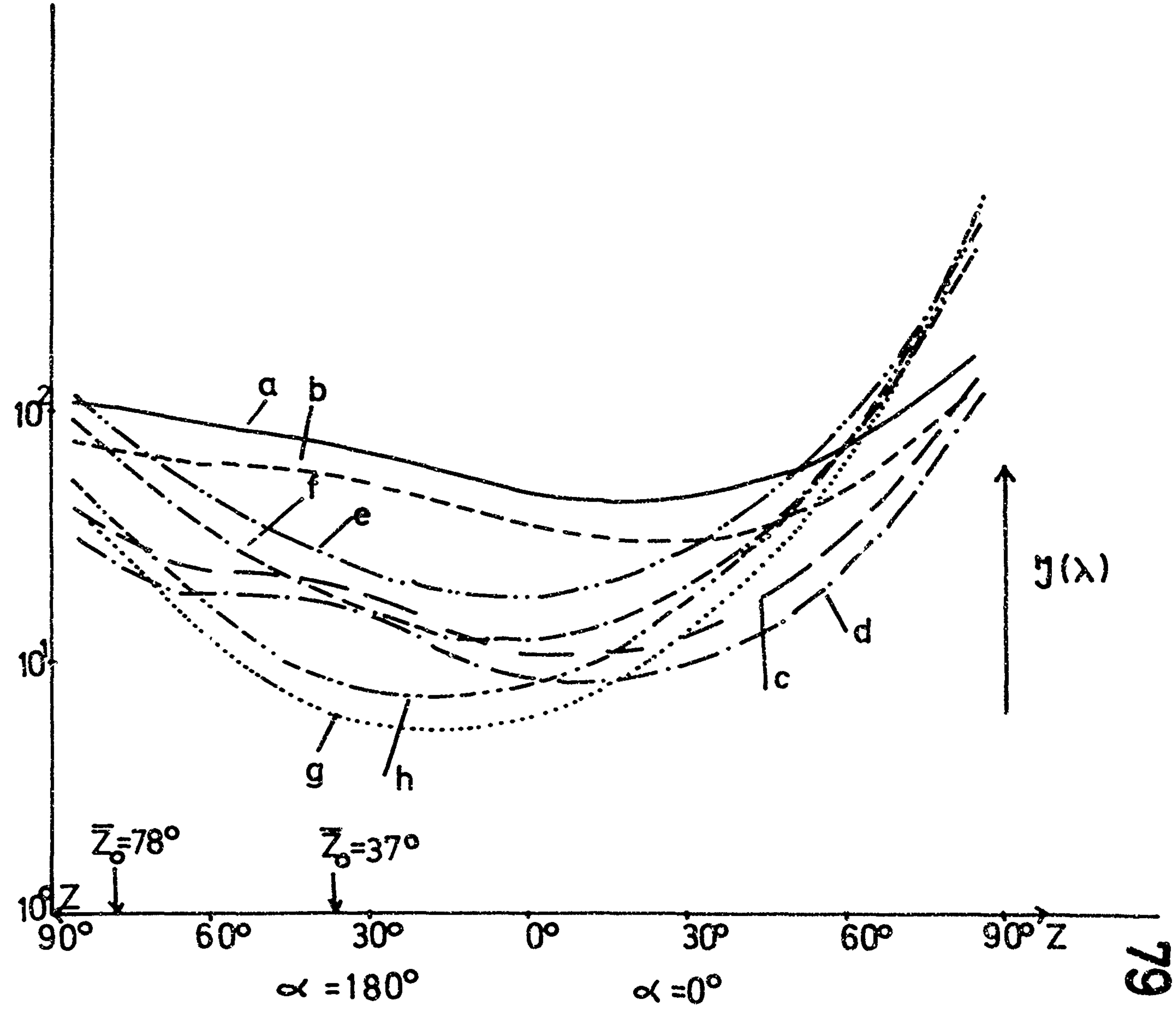

a
b
f
e
c
d
g
h
10^2
10^1
10^0
$\mathfrak{J}(\lambda)$
$\bar{Z}_o=78°$
$\bar{Z}_o=37°$
Z
90°
60°
30°
0°
30°
60°
90°
Z
α =180°
α =0°

79

UNCLASSIFIED
Security Classification

DOCUMENT CONTROL DATA - R & D

(Security classification of title, body of abstract and indexing annotation must be entered when the overall report is classified)

1. ORIGINATING ACTIVITY (Corporate author) Meteorologisch-Geophysikalisches Institut Johannes Gutenberg Universität Mainz, Germany	2a. REPORT SECURITY CLASSIFICATION Unclassified 2b. GROUP

3. REPORT TITLE
RESEARCH ON ATMOSPHERIC OPTICAL RADIATION TRANSMISSION

4. DESCRIPTIVE NOTES (Type of report and inclusive dates)
Scientific. Interim.

5. AUTHOR(S) (First name, middle initial, last name)
K.Bullrich, W.Blättner, T.Conley, R.Eiden, G.Hänel, K.Heger, W.Nowak

6. REPORT DATE	7a. TOTAL NO. OF PAGES	7b. NO. OF REFS
January 1968	97	28

8a. CONTRACT OR GRANT NO. F61052 67 C 0046 b. PROJECT NO. 7621-03 62405394 681000	9a. ORIGINATOR'S REPORT NUMBER(S) Scientific Report No 6 9b. OTHER REPORT NO(S) (Any other numbers that may be assigned this report)

10. DISTRIBUTION STATEMENT
This document has been approved for public release and sale; its distribution is unlimited.

11. SUPPLEMENTARY NOTES	12. SPONSORING MILITARY ACTIVITY Air Force Cambridge Research Laboratories(CROA L.G.Hanscom Field Bedford, Mass. 01730

13. ABSTRACT

A. Measurements of the spectral distribution of the sky radiation and of the radiation reflected by the ground as well as their degrees of polarization at Alamogordo, N.M., USA.
B. Experimental and theoretical investigations into the spectral and angular dependence of reflectivity and the degree of polarization of reflected radiation of various soil types.
C. The influence of the shape of the aerosol particles on their collection in a jet impactor.
D. Contribution to the polarization of the sky radiation.
E. A portable scattering function meter.
F. The influence of second order scattering on the sky radiation and on the radiation emerging from the earth's atmosphere under the assumption of a turbid atmosphere.

DD FORM 1473

UNCLASSIFIED
Security Classification

UNCLASSIFIED

Security Classification

14 KEY WORDS	LINK A		LINK B		LINK C	
	ROLE	WT	ROLE	WT	ROLE	WT
Albedo. Atmospheric aerosol particles. Atmospheric scattering function. Ground reflection. Impactor collection. Second order scattering on large particles. Sky light polarization. Sky radiation.						

UNCLASSIFIED

Security Classification